Titre: Title:	Study of uniplanar phase inverter, ring coupler and magic-t circuits
Auteur: Author:	Yanyan Zhang
Date:	2001
Type:	Mémoire ou thèse / Dissertation or Thesis
Référence: Citation:	Zhang, Y. (2001). Study of uniplanar phase inverter, ring coupler and magic-t circuits [Mémoire de maîtrise, École Polytechnique de Montréal]. PolyPublie. https://publications.polymtl.ca/8727/

URL de PolyPublie: PolyPublie URL:	https://publications.polymtl.ca/8727/
Directeurs de recherche: Advisors:	Ke Wu
Programme: Program:	Non spécifié

UNIVERSITÉ DE MONTRÉAL

STUDY OF UNIPLANAR PHASE INVERTER, RING COUPLER AND MAGIC-T CIRCUITS

YANYAN ZHANG
DÉPARTEMENT DE GÉNIE ÉLECTRIQUE
ET GÉNIE INFORMATIQUE
ÈCOLE POLYTECHNIQUE DE MONTRÉAL

THÈSE PRÉSENTÉE EN VUE DE L'OBTENTION DU DIPLÔME DE
MAITRISE
(GÉNIE ÉLECTRIQUE)
AVRIL 2001

UNIVERSITÉ DE MONTRÉAL

ÈCOLE POLYTECHNIQUE DE MONTRÉAL

Cette thèse intitulée:

STUDY OF UNIPLANAR PHASE INVERTER, RING COUPLER AND MAGIC-TEE CIRCUITS

présentée par: ZHANG Yanyan

en vue de l'obtention du diplôme de: MAITRISE

a été dûment acceptée par le jury d'examen constitué de:

M. BOSISIO Renato-G, président

M. WU Ke, Ph.D., membre et directeur de recherche

M. AKYEL Cevdet, Ph.D., membre

To my family.

Acknowledgments

I would like to gratefully express my sincere appreciation to my advisor Prof. Ke Wu for his constant encouragement, support and guidance throughout my graduate study at École polytechnique. I would also like to thank the members of my committee, Profs. Renato-G. Bosisio and Cevdet Akyel for their helpful suggestions and precious time spent in reviewing this thesis and participating in the oral defense.

Sincere thanks are due to Profs. Renato G. Bosisio, Jean-Jacques Laurin and Cevdet Akyel for their expertise added greatly in my graduate education. I would like to extend my gratitude to Jules Gauthier for the fabrication and packaging of circuits and Rene Archambault for the computer and measurement system management. I would also like to thank the research members in Poly-GRAMES Research Center, especially Jinbang Tang and Jerome Colinas, for their helps and friendship.

I wish to express my deep gratitude to my family for their love and support that they have never failed to provide. I am especially grateful to my father, Zhonggan Zhang, my husband, Tongqing Wang and my daughter, Jean Wang, for their encouragement and love during the journey of my graduate study.

Résumé

Ce mémoire présente l'étude de circuits inverseurs de phase uniplanaires: les coupleurs en anneau et les T magiques. Une étude complète des propriétés électriques des circuits uniplanaires a été effectuée. Plusieurs circuits uniplanaires innovateurs ont été développés. Un résumé des travaux effectués dans ce mémoire est donné ci-dessous.

Des lignes microrubans coplanaires et des circuits lignes microrubans microcoplanaires inverseurs de phase ont été développés. Les performances électriques de l'inverseur de phase sont obtenues à partir d'une analyse électromagnétique basée sur une méthode d'éléments finis. Les résultats simulés et expérimentaux montrent que les circuits inverseurs de phase conviennent aux applications large-bande. Les pertes d'insertion du circuit inverseur de phase coplanaire sont de -0.4 dB jusqu'à 10.0 GHz et la différence de phase est de $-182° \pm 3°$ jusqu'à 8.8 GHz.

Des coupleurs en anneau uniplanaires de type série et parallèle avec des inverseurs de phase ont été étudiés. Les caractéristiques principales et les considérations sur la conception du coupleur en anneau sont discutées. Une méthode générale de conception est donnée. Deux circuits en anneau ont été développés. Les mesures montrent que ces deux coupleurs offrent de bonnes performances électriques. L'isolation mutuelle est plus petite que -20.0 dB sur une largeur de bande plus grande qu'un octave. L'erreur de phase des coupleurs en anneau microrubans coplanaires est plus petite que $\pm 4°$ sur un intervalle de fréquences de 1.0 - 2.3 GHz.

Une étude complète des T magiques uniplanaires a été effectuée. Les performances électriques des circuits T magiques uniplanaires sont données en détail. Les conditions d'adaptation des circuits T magiques uniplanaires ont été obtenues à partir d'une analyse de circuit. Les équations de conception générales des circuits T magiques uniplanaires

sont données. Un circuit T magique uniplanaire compacte a été développé. Les caractéristiques électriques sont calculées en effectuant une analyse par éléments finis. Les mesures montrent que la différence d'amplitude du coefficient de transmission entre deux portes H du coupleur balancé est plus petite que 0.2 dB sur l'intervalle de fréquence 2 - 4.5 GHz . Sur cette même plage de fréquence, l'isolation entre les portes E et H est plus petite que -40 dB . Enfin, ce mémoire présente des suggestions pour les travaux futurs.

Abstract

This thesis presents a study of uniplanar phase inverters, ring couplers and magic-tee circuits. A comprehensive investigation of electrical performance of the uniplanar circuits has been made. Several novel uniplanar circuits have been proposed and developed. Following is a summary of the work presented in this thesis.

Coplanar stripline and micro-coplanar stripline phase inverter circuits have been studied and developed. Electrical performance of the phase inverters is obtained by using a full-wave analysis based on a finite element method. Simulated and measured results show that both phase inverter circuits are suitable for broadband applications. For the coplanar phase inverter, the insertion loss within -0.4 dB has been achieved up to 10.0 GHz while the phase shift within $-182° \pm 3°$ has been obtained up to 8.8 GHz.

Series- and parallel-type uniplanar ring couplers with phase inverter have been studied in detail. Principal features and design considerations for the ring couplers are discussed. A generalized design formulation is derived. Two ring coupler circuits have been developed. Electrical characteristics are obtained by using a finite element analysis. The measurements show that both ring couplers have a fairly good performance. Their mutual isolation is better than -20.0 dB over a bandwidth of more than one octave. For the coplanar stripline ring coupler, the phase error of less than $\pm 4°$ has been demonstrated in the frequency range of 1.0 - 2.3 GHz.

A comprehensive study of uniplanar magic-tee (or magic-T) has been developed. Electrical performance of uniplanar magic-T circuits is discussed in detail. The matching condition of uniplanar magic-T circuits has been obtained from a simple circuit analysis. Generalized design equations for the uniplanar magic-T are also derived. A compact uniplanar magic-T circuit has been developed. Its electrical characteristics are calculated

by using a finite element analysis. Measured results show that the maximum amplitude imbalance for the port H is less than 0.2 dB in the frequency rang of 2 - 4.5 GHz . Over the same frequency range, the isolation between ports E and H is better than -40 dB . The thesis is the concluded together with suggestions for the future work.

Étude de circuits inverseurs de phase uniplanaires, coupleurs en anneau, et T magiques

Ce mémoire présente l'étude de circuits inverseurs de phase uniplanaires, de coupleurs en anneau, et de circuits T magiques.

0.1 Introduction

L'avancement des applications commerciales en micro-ondes et ondes millimétriques a permis d'accroître la demande pour des circuits intégrés micro-ondes MIC (*Microwave Integrated Circuits*). La recherche dans le domaine des MIC est très active, elle vise à développer des composantes et sous-systèmes compactes et peu coûteux qui répondent aux besoins du marché. Dans les dernières décennies, beaucoup d'efforts ont été faits pour développer des circuits uniplanaires MIC. Dans les circuits uniplanaires MIC, tous les conducteurs sont placés sur le côté du substrat. Cela permet une niveau d'intégration élevé. De plus ce type de circuit est très bien adapté la conception en haute-fréquence puisque on élimine la connexion au plan de masse avec des vias. Pour étendre l'emploi des circuits uniplanaires aux applications commerciales, des composantes uniplanaires de coûts variables et de hautes performances sont nécessaires. C'est pourquoi, la recherche et le développement de nouveaux dispositifs uniplanaires est pleinement justifiée.

Les circuits hybrides sont des composantes indispensables pour de nombreuses applications MIC comme les amplificateurs balancés, les melangeur balancés, les circuits déphaseurs, et les circuits d'alimentation de réseau d'antennes. Un circuit hybride couramment utilisé est le circuit hybride en anneau (*rat-race hybrid ring*). Le coupleur en anneau offre l'avantage d'isoler les deux portes d'entrées indépendamment de l'impédance de terminaison. Le coupleur en anneau est composé d'un anneau et de quatre lignes d'alimentation. Selon le type de connexion entre la ligne d'alimentation et l'anneau, on distingue 3 catégories : le type série, le type parallèle, et le T magique. À

notre connaissance, la littérature scientifique concernant la conception de ces trois types de circuits hybrides uniplanaires en anneau n'est pas complète.

À partir de ce qui a été discuté plus haut, le travail de ce mémoire est centré sur l'étude des circuits inverseurs de phase, des coupleurs en anneau et circuits des T magiques. Ce mémoire contient six chapitres. Le chapitre II présente les performances électriques des lignes d'alimentations coplanaires et des circuits inverseurs de phase microrubans micro-coplanaires. Le chapitre III traite la conception de coupleurs en anneau uniplanaires de type série avec inverseur de phase. Une discussion sur la conception du coupleur en anneau de type parallèle est donnée dans le chapitre IV. Le chapitre V présente une analyse et une conception innovatrice des circuits uniplanaires en T magique. Les conclusions et recommandations pour les travaux futurs sont présentées dans le dernier chapitre.

0.2 Circuits uniplanaires inverseurs de phase

Dans les circuits intégrés micro-ondes et ondes millimétriques, un élément circuit déphaseur de 180° est utilisé pour obtenir l'annulation de deux signaux d'amplitudes égales. Le circuit déphaseur de 180° est couramment employé pour la conception de coupleurs uniplanaires en anneau pour réduire la taille du circuit et augmenter la largeur de bande. Le chapitre II présente deux circuits inverseurs de phase : alimenté par ligne coplanaire et alimenté par ligne micro-coplanaire.

Les performances électriques des circuits inverseurs de phase sont calculés à l'aide du logiciel commercial HFSS. Les résultats simulés montrent que les pertes de retour $|S_{11}|$ et $|S_{22}|$ pour les circuits inverseurs de phase avec alimentation microruban coplanaire sont plus petites que -17 dB jusqu'à 9.0 GHz. Sur la même plage de fréquences les pertes d'insertions sont de -0.3 dB. La phase d'insertion du circuit inverseur de phase microruban coplanaire est de $-180° \pm 1.5°$ jusqu'à 10.0 GHz. Pour les inverseurs de

phase microruban micro-coplanaire, les pertes de retour $|S_{11}|$ et $|S_{22}|$ sont de plus petites que -15 dB dans l'intervalle de fréquence $2.7-4.9$ GHz. Dans le même intervalle de fréquence les pertes d'insertion sont de l'ordre de -0.3 dB. La largeur de bande pour une erreur de phase de $\pm 10°$ est de 2.1 GHz , dans l'intervalle 2.2 - 4.3 GHz.

Pour valider les résultats simulés, des circuits inverseur de phase ont été fabriqués et testés. Les mesures montrent que les pertes de retour sont plus petites que -13.5 dB jusqu'à la fréquence de 9.6 GHz. Les pertes d'insertion sont de l'ordre -0.4 dB jusqu'à 10.0 GHz et la phase d'insertion est de l'ordre $-182° \pm 3°$ jusqu'à 8.8 GHz. Les circuits inverseurs de phase microruban micro-coplanaire offrent une perte d'insertion petite que -10 dB dans l'intervalle de fréquence de 2.3 - 5.2 GHz. Les pertes d'insertion sont de l'ordre de -1.0 dB dans l'intervalle de fréquence de 1.9 - 4.7 GHz. La phase d'insertion est de l'ordre de $-180° \pm 10°$ dans l'intervalle de fréquence de 2.2 - 4.3 GHz. Clairement, les résultats mesurés sont en accord avec les résultats simulés. Les deux circuits inverseurs de phase offrent de bonnes performances électriques et conviennent à des applications large bande.

0.3 Analyse et conception d'un coupleur en anneau de type série avec inverseur de phase

Le chapitre III présente l'analyse et la conception de coupleurs en anneau uniplanaires de type série avec inverseur de phase. Un schéma d'un coupleur en anneau de type série avec un inverseur de phase idéal est montré à la figure 3.1. Les paramètres S sont obtenus en utilisant une analyse *full-wave* des modes pairs et impairs. Les principales caractéristiques du coupleur en anneau sont :

(a) L'isolation entre deux portes de sortie est parfaite et est indépendante de la fréquence.

(b) La différence de phase entre deux portes de sortie est de 0°/180° et est aussi indépendante de la fréquence.

(c) Le rapport de puissance entre les deux sorties est proportionnel au carré du terme $\left|\frac{Z_1 \cdot \sin\theta_2}{Z_2 \cdot \sin\theta_1}\right|$.

La conception d'une coupleur en anneau 3-dB a été effectuée. Les coupleurs en anneau se distinguent en deux catégories : Les larges bandes, les bandes étroites. Les équations pour les larges bandes et bandes étroites sont données par les équations (3.14) et (3.16), respectivement. Pour valider la conception technique, un coupleur en anneau microruban coplanaire 3-dB avec inverseur de phase a été simulée. Les performances électriques sont calculées avec le logiciel commercial HFSS. Les résultats calculés montrent que les pertes de retour $|S_{11}|$ et $|S_{44}|$ sont plus petites que -20 dB de 1.9 GHz à 3.3 GHz. Pour les mêmes spécifications, la largeur de bande effective de $|S_{22}|$ et $|S_{33}|$ est 0.9 GHz dans l'intervalle 2.1 - 3.0 GHz. Le couplage pour toutes les portes est de -3.7 ± 0.5 dB dans l'intervalle 1.6 - 3.0 GHz. L'isolation mutuelle entre les portes 1(2) et 3(4) est meilleure que -20 dB dans l'intervalle 1.0 - 3.4 GHz. L'erreur de phase entre les portes en phase et les portes déphasées de 180° est plus petite que $\pm 5°$ dans l'intervalle de fréquence 1.3 - 3.3 GHz.

Les résultats expérimentaux sont obtenus à partir d'une calibration TRL. Les mesures montrent que les pertes de retour du coupleur sont meilleures que -15 dB dans l'intervalle de fréquence 1.4 - 2.4 GHz. Le couplage entre les portes est de -3.6 ± 0.8 dB dans l'intervalle 1.0 - 2.3 GHz. L'isolation entres les portes 1(2) et 3(4) est meilleure que -20 dB dans l'intervalle de fréquence 1.0 - 2.2 GHz. L'erreur de phase entre les sorties est plus petite que $\pm 4°$ dans l'intervalle de fréquence 1.0 - 2.3 GHz.

En conclusion, les résultats simulés sont cohérents avec les résultats mesurés et montrent que le coupleur en anneau offre de bonnes performances. Dans une certaine mesure, ceci valide la théorie développée sur la conception.

0.4 Analyse et conception d'un coupleur en anneau de type parallèle avec inverseur de phase

L'analyse et la conception d'un coupleur en anneau de type parallèle avec inverseur de phase est présentée au chapitre IV. Un schéma du coupleur en anneau avec un inverseur de phase idéal est montrée à la figure 4.1. De manière similaire, Les paramètres S du coupleur sont obtenus à partir d'une analyse des modes pairs et impairs. Les équations de conception du coupleur en anneau de type parallèle pour les applications larges bandes et bandes étroites sont données par (4.16) et (4.18), respectivement. Pour valider la conception, un coupleur en anneau 3-dB microruban micro-planaire a été développé. Les performances électriques ont été calculées avec HFSS. Les résultats simulés montrent que les pertes de retour $|S_{11}|$ et $|S_{44}|$ du coupleur sont meilleures que -15 dB de 1.3 GHz à 2.5 GHz. Pour des spécifications identiques, le largeur de bande effective pour $|S_{22}|$ et $|S_{33}|$ est de 1.6 GHz à 1.0 - 2.6 GHz. Le couplage $|S_{12}|$, $|S_{23}|$ et $|S_{43}|$ est de l'ordre de -3.5 ± 0.5 dB dans l'intervalle 0.9 - 2.5 GHz. Pour des spécifications de couplage identiques, la largeur de bande $|S_{14}|$ est 0.8 GHz dans l'intervalle 1.5 - 2.3 GHz. L'isolation mutuelle entre les portes 1(2) et 3(4) est meilleure que -20 dB dans l'intervalle 1.2 - 3.0 GHz. L'erreur de phase entre les deux portes de sorties sont plus petites que $\pm 5°$ dans l'intervalle de fréquence 1.5 - 2.4 GHz.

Les résultats expérimentaux ont été obtenus à partir d'une calibration TRL. Les mesures montrent que les pertes de retour du coupleur sont meilleures que -18 dB dans l'intervalle de fréquence de 1.6 - 2.6 GHz. Le couplage pour toutes les portes de sorties est de l'ordre de -3.5 ± 0.6 dB dans l'intervalle 1.6 - 3.0 GHz. L'isolation mutuelle entre les portes 1(2) et 3(4) est meilleure que -20 dB dans l'intervalle de fréquence 1.0 - 3.5 GHz. L'erreur de phase entre les portes de sorties est plus petite que $\pm 5°$ dans l'intervalle de fréquence 1.6 - 2.5 GHz. Il est clair que le coupleur en anneau offre de bonnes performances électriques. Les résultats expérimentaux montrent que les résultats sont en accord avec les résultats simulés.

0.5 Analyse et conception d'un circuit uniplanaire en T magique

Le chapitre V présente une analyse et conception de circuits uniplanaire en T magique. Selon le type de connexion, ce type de circuit se divise en deux catégories: Le type série et le type parallèle. Il est communément admis qu'il n'existe pas de couplage entre les portes H et E à cause des distributions de champs pairs et impairs à la jonction. Dans le chapitre V, il est montré avec la loi de la conservation de puissance d'un réseau sans perte, que la conception d'un circuit uniplanaire T magique peut être simplifiée à la conception de l'adaptation de l'impédance d'entrée des portes E et H. En utilisant une analyse de circuit, on découle les équations de conception pour le type série et le type parallèle. Les équations de conception pour un circuit de type série sont données par (5.15) et (5.17). Les équations de conception pour un circuit de type parallèle sont données par (5.27) et (5.29).

Pour valider la théorie de conception, un circuit T magique compacte a été développé. La configuration physique du circuit T magique est montrée à la figure 5.8. Les performances électriques ont été calculées avec le logiciel commercial HFSS. Les résultats simulés montrent que les pertes de retour du circuit T magique sont meilleures que -17 dB à la fréquence centrale $f = 3.5$ GHz. La division de puissance pour les portes E et H est de -3.8 dB et -3.1 dB à la fréquence $f = 3.5$ GHz, respectivement. L'isolation mutuelle entre les portes E et H est meilleure que 40 dB. L'erreur de phase entre les deux portes de sortie est plus petite que 1° dans l'intervalle de fréquence $2 - 4.5$ GHz.

Les résultats expérimentaux ont été obtenus à partir d'une calibration TRL. Les mesures montrent que les pertes de retour du circuit T magique sont meilleures que -18 dB dans l'intervalle de fréquence de $3 - 3.5$ GHz. L'amplitude maximum non-balancée pour la porte H est plus petite que 0.2 dB dans l'intervalle de fréquence $2 - 4.5$ GHz. L'isolation mutuelle à la fréquence centrale $f = 3.5$ GHz est meilleure que -20 dB. L'isolation

entre les portes E et H est meilleure que -40 dB dans l'intervalle de fréquence $2-4.5$ GHz.

En conclusion, les résultats simulés sont en accord avec les résultats mesurés et montrent que le circuit T magique proposé offre de bonnes performances. Dans une certaine mesure, ceci valide le développement théorique de la conception.

0.6 Conclusion et recommandations pour les travaux futurs

En conclusion, ce mémoire présente l'étude de circuit inverseur de phase uniplanaire, coupleur en anneau et T magique. Une théorie de conception générale a été développée pour les trois type coupleurs en anneau. Quelques circuits uniplanaire innovateurs ont été développés. Leur performances électriques ont été simulés en utilisant une analyse *full-wave* basée sur une méthode par éléments finis. Les résultats simulés et mesurés montrent que les circuits uniplanaire offrent de bonnes performances électriques. Il peuvent être utilisés comme composantes fondamentales dans plusieurs applications de circuits micro-ondes et onde millimétriques.

Les travaux futurs associés avec ce mémoire devrait inclure (a) le développement d'un inverseur de phase large bande utilisant des structures guides d'onde uniplanaires, (b) l'extension de la conception d'un coupleur en anneau à un diviseur de puissance de rapport arbitraire, et (c) développement de circuits plus complexes comme les amplificateurs balancés, les mélangeurs balancés, les *transceivers* uniplanaires micro-ondes et ondes millimétriques pour les radars et les systèmes de communication. Les travaux futurs devraient aussi inclure l'étude de mise en production de circuits uniplanaires pour des applications commerciales.

Table of Contents

List of Figures

Chapter I

Introduction

1.1 Background and motivation

In recent years, an increasing demand can be seen for microwave and millimeter-wave systems for commercial applications, such as wireless communication systems, global positioning systems and automotive collision-avoidance radar systems. In these applications, microwave integrated circuits (MICs) play an important role in determining performance of these systems. MICs have advantages of small size, light weight, high reliability, low-cost and they are well suited for high volume production, which is an important factor for consumer applications. The MIC is currently subject to intense research aimed at developing cost-effective compact components and subsystems suitable for such applications.

In MICs, planar transmission lines are one of the most essential elements. Earlier work on MICs was mostly carried out based on microstrip line. In microstrip line, the strip and ground plane are located on the opposite sides of substrate. It is known that this configuration suffers from some potential physical defects such as the dependency of electrical property on substrate thickness and difficult integration of three-terminal active devices and shunt elements. A drilled hole is usually needed for DC-grounding. To overcome the shortcomings of microstrip line, considerable efforts have been made to develop uniplanar MICs in the past decades [1-4]. The uniplanar MIC only uses one side of the substrate. Its key elements are uniplanar guided-wave structures, which usually consist of coplanar waveguide, coplanar stripline, slotline, and micro-coplanar stripline as shown in Figure 1.1. Generally speaking, these transmission lines have advantages of

easy realization of short-circuited ends, and simple integration of series and shunt passive and active chip elements. As all conductors are located on the same side of substrate, it permits a high-level integration and well-suited to high-frequency design since the grounding connection through via-holes is eliminated and potential parasitic effects related to active device implementation may be minimized. In addition, potentially easy inter-transition among different structures provides a great flexibility for circuit design. Considering those advantages of uniplanar MICs, research on the development of novel uniplanar circuits is fully justified.

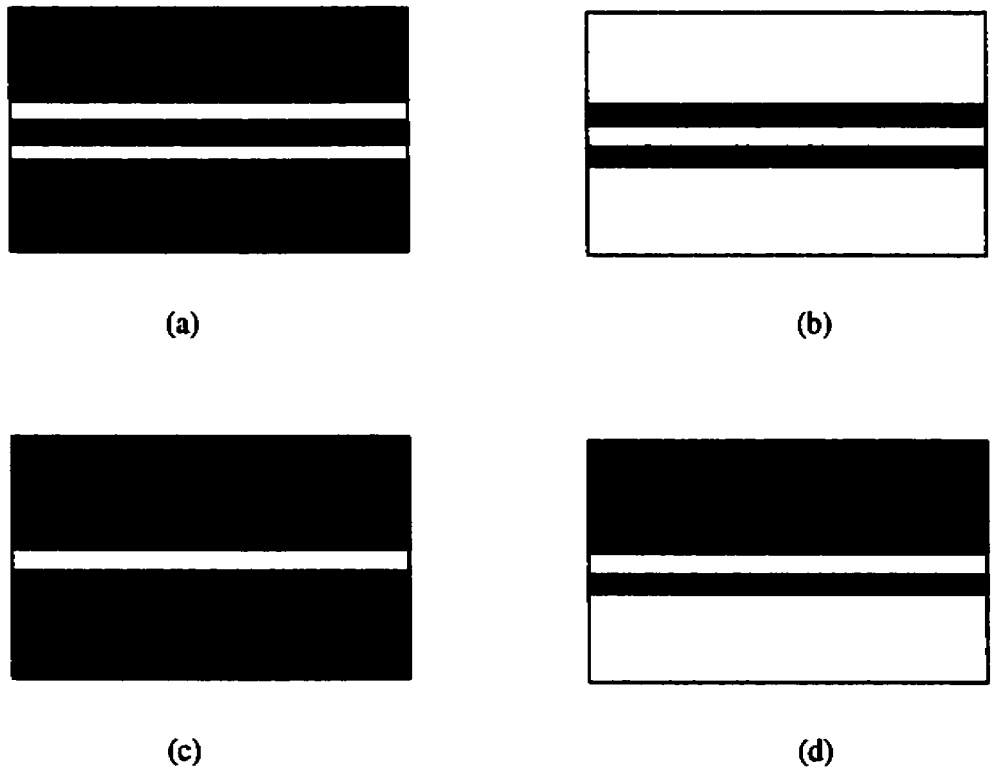

Figure 1.1 Uniplanar guided-wave structures (a) coplanar waveguide, (b) coplanar stripline, (c) slotline, and (d) micro-coplanar stripline.

In microwave systems, coupler is a widely used component. In particular, 3 dB hybrid coupler is an indispensable building block for various microwave and millimeter-wave circuits such as balanced amplifier, balanced mixer, frequency discriminator, phase shifter, (de)modulator and feeding network in antenna array. To a large extent, hybrid coupler in view of phase difference between its two output ports can be classified into two categories: 90° and 0°/180°. Parallel coupled-line and branch-line couplers are well-known examples of 90°-hybrid coupler and their electrical performance has been well documented in [5-7]. For certain applications, namely, mixer, modulator and isolating power splitter, 0°/180° hybrid coupler is more preferred than its 90° counterpart since its isolation between the two input ports may be independent of the value of two balanced-impedance loads. And also, a typical 0°/180° hybrid ring coupler has a wider bandwidth than the branch-line coupler [8].

One well-known example of 0°/180° hybrid couplers is rate-race ring which consists of three one-quarter-wavelength sections and one three-quarter-wavelength sections. It has been used as 3-dB directional coupler. Its main drawbacks are large size and limited usable bandwidth due to the three-quarter-wavelength section. Over the last decades, a large amount of research efforts have been made to improve performance of this type of coupler. Several design techniques have been proposed to enhance the effective bandwidth and also reduce the circuit size [9-11]. Among the techniques, using one-quarter wavelength section with phase inverter to replace its conventional three-quarter wavelength line has found a wide acceptance in uniplanar MICs. Several broadband uniplanar hybrid ring couplers with phase inverter have been presented in [12]. A miniaturized uniplanar 0°/180° hybrid ring coupler having $0.67\lambda_g$ circumference was reported in [13] and the circuit is composed of a coplanar strip ring and CPW feed lines. A crossover of two strips on the ring achieved a 180° phase shift. Recently, a systematic design procedure for the hybrid ring coupler using phase inverter has been developed in [14]. It should be noted that the development was carried out only for ring couplers with the feed lines connecting to ring in parallel.

Generally speaking, a ring coupler is composed of ring and four feed lines. In light of connection between feed lines and ring, the couplers can be divided into three categories: series-type, parallel-type and magic-T. In the series-type ring couplers, four feed lines are connected to ring in series while in the parallel-type ring couplers four feed lines are connected to ring in parallel. Magic-T contains both series and parallel connections. To our knowledge, there is the lack of a complete description for the design of all the three types of uniplanar hybrid ring couplers.

1.2 Overview of thesis

Based on the above discussion, this work is centered on a comprehensive study of uniplanar phase inverter, ring coupler and magic-T. The thesis consists of six chapters. Chapter II will present coplanar stripline and micro-coplanar stripline phase inverter circuits. Electrical performance for the phase inverters is studied using a full-wave analysis based on a finite element method. Numerical and experimental results show that both the phase inverter circuits are suited for broadband application. For the coplanar stripline phase inverter, the insertion loss within -0.4 dB has been achieved up to 10.0 GHz while the phase shift within $-182° \pm 3°$ has been obtained up to 8.8 GHz.

Chapter III addresses the design of the uniplanar series-type ring coupler with phase inverter. A generalized design formulation is derived. Principal features and design criteria for the ring coupler are summarized. To verify the proposed design theory, a coplanar stripline ring coupler with phase inverter is developed and tested. Experimental results show that the mutual isolation is better than -20.0 dB over a bandwidth of more than one octave. The phase error of less than $\pm 4°$ has been demonstrated in the frequency range of 1.0 - 2.3 GHz.

Chapter IV provides a summary of design for the uniplanar parallel-type ring coupler with phase inverter. A micro-coplanar stripline ring coupler is developed. Field analysis for the coupler is completed by using a finite element technique. Measurements show that

the ring coupler has a fairly good electrical performance. Its mutual isolation is better than -20.0 dB in frequency range of 1.0 - 3.5 GHz. The coupling for all the port is within -3.5 ± 0.6 dB from 1.6 - 3.0 GHz.

Chapter V presents analysis and design of novel uniplanar magic-T circuits. Two basic configurations of the uniplanar magic-T circuits are described. The discussion includes electrical performance and matching condition of the uniplanar magic-T circuits. Generalized design equations are derived. A compact uniplanar magic-T circuit is developed. Measured results show that the maximum amplitude imbalance for the port H is less than 0.2 dB in the frequency rang of 2 - 4.5 GHz. Over the same frequency range, the isolation between ports E and H is better than -40 dB.

The conclusions of this thesis and recommendation for future work are presented in the final chapter.

Chapter II

Uniplanar Phase inverter Circuits

2.1 Introduction

In microwave and millimeter-wave integrated circuits, a circuit element with a 180° phase shift is usually required in order to achieve the cancellation of two-path signals with equal amplitude. As mentioned before, the phase inverter that has 180° phase shift has been widely used in the design of broadband and size-reduced ring couplers. In general, a phase inverter may be obtained by reversing signal and ground paths or field orientations with reference to a particular path. It is obvious that this mechanism can be easily realized with uniplanar techniques in which all conductors are located on the same side of substrate. Some broadband uniplanar phase inverters have been reported in [3,15]. In this chapter, we present two circuits of phase inverter, which are realized with coplanar stripline and micro-coplanar stripline, respectively. Numerical and experimental results are given below in detail. Both phase inverters will be used in the design of ring couplers to be discussed in the following chapters.

2.2 Coplanar stripline phase inverter

Figure 2.1(a) illustrates the physical configuration of a coplanar stripline phase inverter. The circuit consists of two coplanar stripline sections. The 180° phase shift is obtained by a two-strip crossover in the middle of transmission line sections. From Figure 2.1(a), it is seen that the E-field orientations are reversed at input and output ports 1 and 2. The phase inverter test circuit was built on a RT/Duriod 6010 ($\varepsilon_r = 10.2$) substrate with thickness $h = 1.27$ mm. Characteristic impedance for the coplanar stripline was chosen

to be 100 Ω with the following dimensions: the strip width $W = 0.30$ mm and the gap size between the two strips $S = 0.28$ mm. The circuit size is 15×15 mm^2. The gap dimension for the two-strip crossover is $G = 0.30$ mm.

Electrical performance of the coplanar stripline phase inverter was calculated using a commercial software HFSS developed by Ansoft. Figure 2.1(b) shows the geometrical model for the performance assessment. A virtual box was introduced to define the field solution area. Radiation boundaries were assigned to four side-surfaces of the virtual box in analysis in order to consider unbounded effects of the circuit. The virtual box was chosen to have dimensions of $15 \times 15 \times 15$ mm^3. The two end-surfaces of the virtual box were assigned to excitation ports 1 and 2 with dimensions of 15×15 mm^2. The crossover for 180° phase shift was modeled by an airbridge with a square cross-section (0.2×0.2 mm^2). Calculated frequency responses for return loss, insertion loss, and phase difference are shown in Figure 2.2. In Figure 2.2(a), it is seen that the return loss for $|S_{11}|$ and $|S_{22}|$ is better than -17 dB up to 9.0 GHz. Figure 2.2(b) shows that over the same frequency rang the insertion loss is better than -0.3 dB. The insertion phase is within $-180° \pm 1.5°$ up to 10.0 GHz. The calculated results suggest that the phase inverter be suitable for the broadband applications.

Measured performance of the phase inverter is shown in Figure 2.3. The measurement was made using GGB probes (40A-GS-750) and a vector network analyzer (HP 8720ES). A TRL calibration was used to remove the system errors of the test station. Figure 2.3(a) shows measured frequency response of return loss for the input and output ports. It is seen that the return loss is better than -13.5dB up to 9.6 GHz. Measured frequency responses of insertion loss and phase are shown in Figure 2.3(b). The insertion loss is within -0.4 dB up to 10.0 GHz, which agrees well with the calculated ones as shown in Figure 2.2(b). The insertion phase is within $-182° \pm 3°$ up to 8.8 GHz. The phase error is due to two-strip crossover discontinuities and probe misalignments.

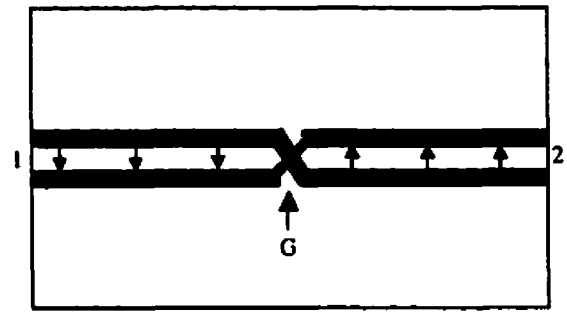

(a)

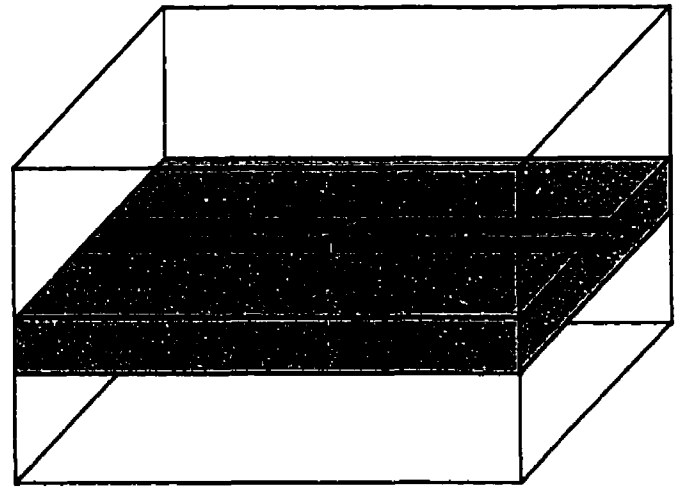

(b)

Figure 2.1 Coplanar stripline phase inverter (a) circuit layout and (b) geometrical model for the finite element analysis.

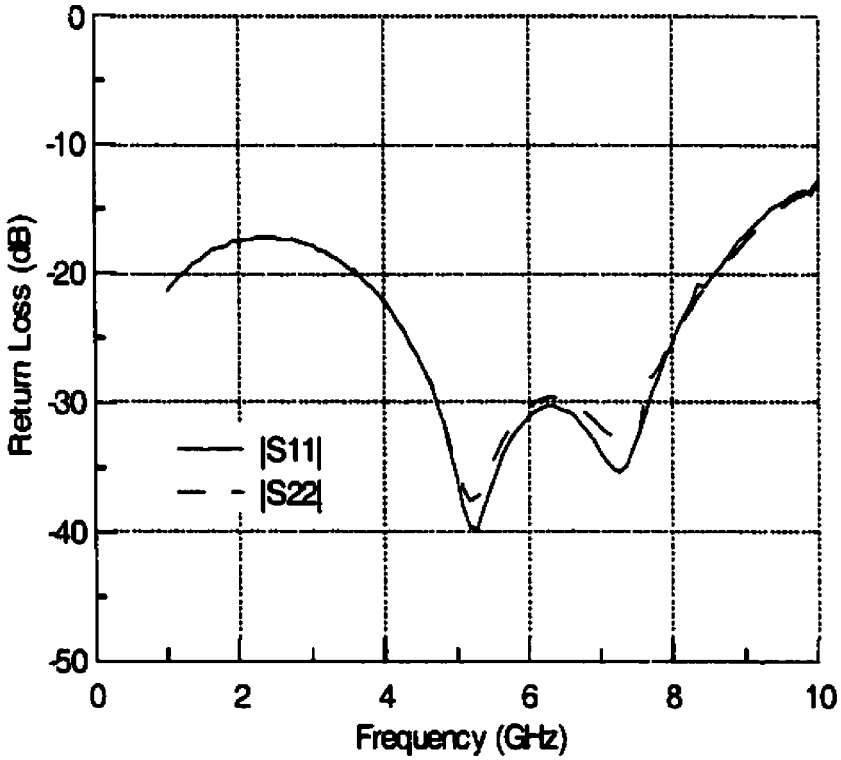

Figure 2.2(a) Calculated frequency responses of return loss for the phase inverter shown in Figure 2.1(b)

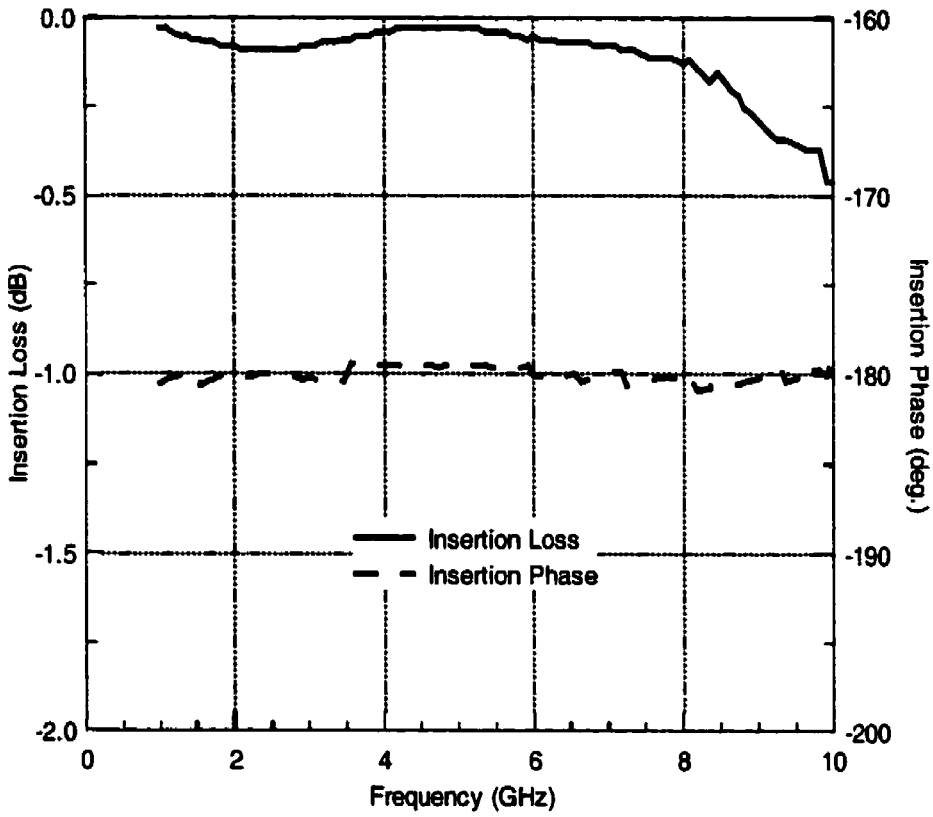

Figure 2.2(b) Calculated frequency responses of insertion loss and phase for the phase inverter shown in Figure 2.1(b)

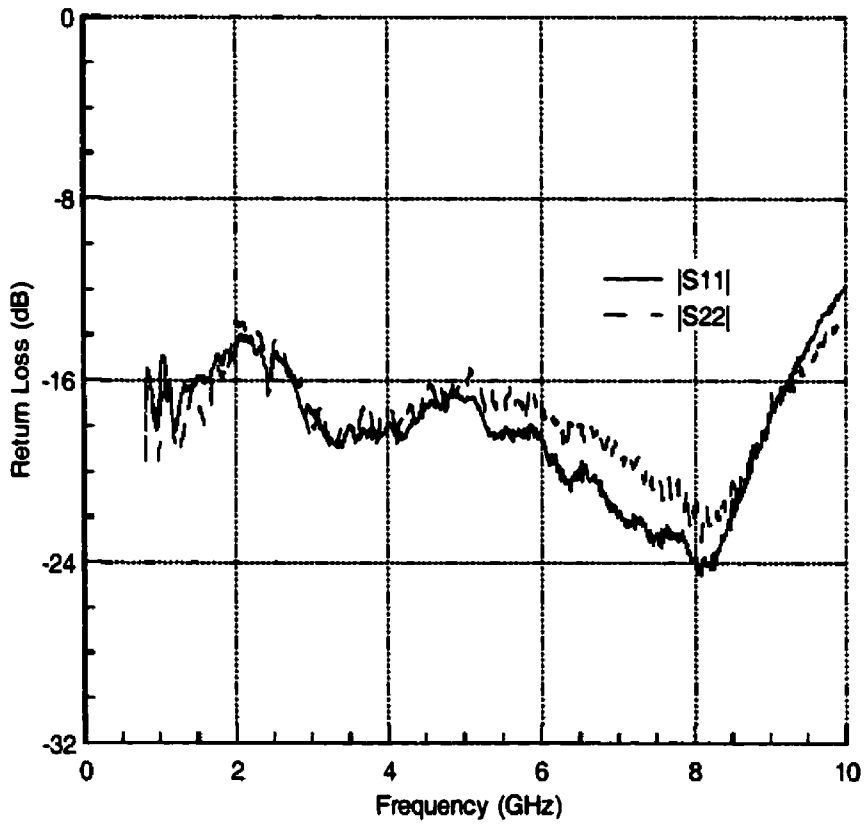

Figure 2.3(a) Measured frequency responses of return loss for the phase inverter shown in Figure 2.1(a)

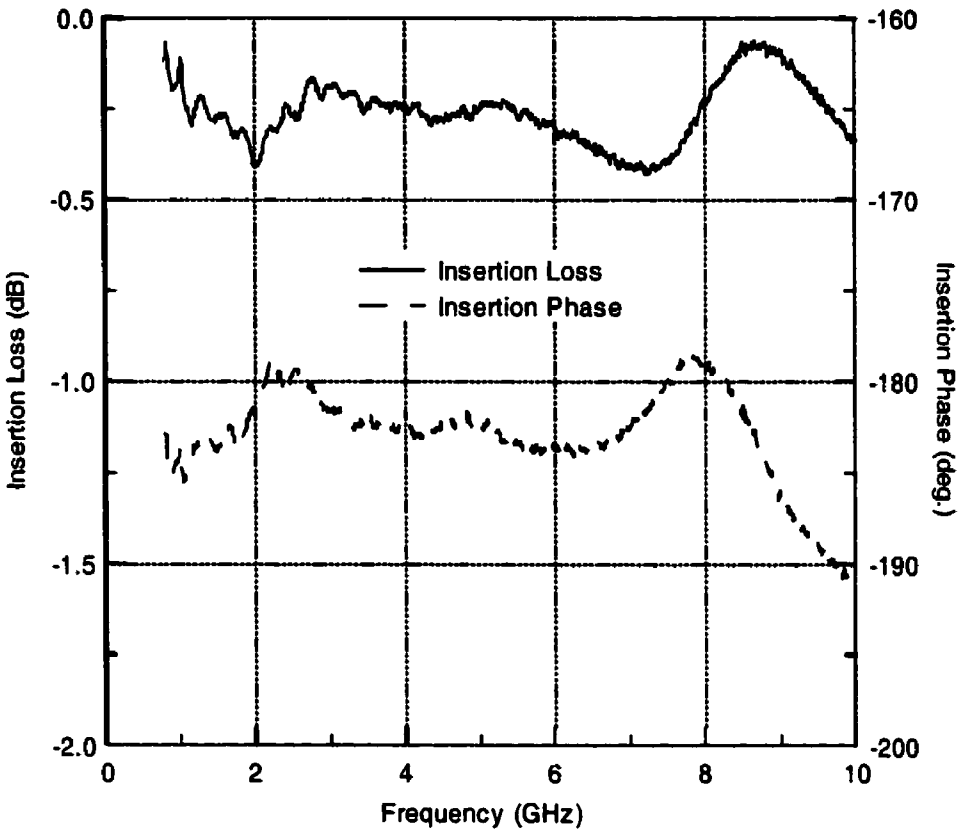

Figure 2.3(b) Measured frequency responses of insertion loss and phase for the phase inverter shown in Figure 2.1(a)

2.3 Micro-coplanar stripline phase inverter

Figure 2.4(a) shows the circuit layout of a micro-coplanar stripline phase inverter. The circuit consists of two micro-coplanar stripline sections and a slotline radial stub. The 180° phase shift is achieved by the combination of the two-strip crossover and the slotline radial stub. The slotline radial stub is designed to produce an open-circuit at the center frequency. Therefore, the two-strip crossover as discussed above provides 180° phase shift. The E-field orientations are reversed at input and output ports 1 and 2 as shown in Figure 2.4(a). The phase inverter test circuit was built on a RT/Duriod 6010 ($\varepsilon_r = 10.2$) substrate with thickness $h = 1.27$ mm. The micro-coplanar stripline dimensions include the strip width $W = 0.76$ mm and the gap size between the strip and ground $S = 0.2$ mm. The circuit size is 15×15 mm^2. Dimensions for the slotline radial stub are the radius $r = 5.5$ mm and angle $\alpha = 60°$. The gap dimension for the two-strip crossover is $G = 0.30$ mm.

Electrical performance of the coplanar stripline phase inverter was calculated by using HFSS. Figure 2.4(b) shows the geometrical model for the calculations of performance. Similarly, a virtual box was introduced to define the field solution area. Radiation boundaries were assigned to four side-surfaces of the virtual box to consider the unbounded effect of the circuit. The virtual box was chosen to have the dimensions of $15 \times 15 \times 15$ mm^3. The two end-surfaces of virtual box were used as excitation ports 1 and 2 with the dimensions of 15×15 mm^2. The crossover for 180° phase shift was modeled by an airbridge with a square cross-section (0.2×0.2 mm^2). Calculated frequency responses for return loss, insertion loss, and phase difference are shown in Figure 2.5. In Figure 2.5(a), it is seen that the return loss for $|S_{11}|$ and $|S_{22}|$ is better than -15 dB in the frequency range of $2.7 - 4.9$ GHz. It is obvious that the effective bandwidth is limited by the slotline radial stub. Figure 2.5(b) shows that over the same frequency rang the insertion loss is within -0.3 dB. The bandwidth for $\pm 10°$ phase error is 2.1 GHz from 2.2-4.3 GHz. From the above results, it is seen that the

bandwidth of micro-coplanar stripline phase inverter is smaller than the counterpart of coplanar stripline due to the slotline radial stub. It is noted that the bandwidth for micro-coplanar stripline phase inverter can be extended with increasing the angle of slotline radial stub.

Measured performance of the phase inverter is shown in Figure 2.6. The measurement was made using GGB probes (40A-GS-750) and a vector network analyzer (HP 8720ES). A TRL calibration was used to remove the system errors of the test station. Figure 2.6(a) shows measured frequency response of return loss for input and output ports. It is seen that the return loss is better than $-10\,\mathrm{dB}$ in the frequency range of 2.3-5.2 GHz. The measured frequency responses of insertion loss and phase shift are shown in Figure 2.6(b). It is seen that the insertion loss is within $-1.0\,\mathrm{dB}$ from 1.9-4.7 GHz. The insertion phase is within $-180° \pm 10°$ in the frequency range of 2.2-4.3 GHz, which agrees well with the calculated results shown in Figure 2.5(b).

2.4 Conclusion

In this chapter, two circuits of phase inverter have been presented. Calculated and measured results show that the coplanar stripline phase inverter has a good performance, which is suited for broadband application. In general, the experimental results agree well with the modeling ones. Both phase inverters will be used in the ring coupler design that will be presented in the subsequent chapters.

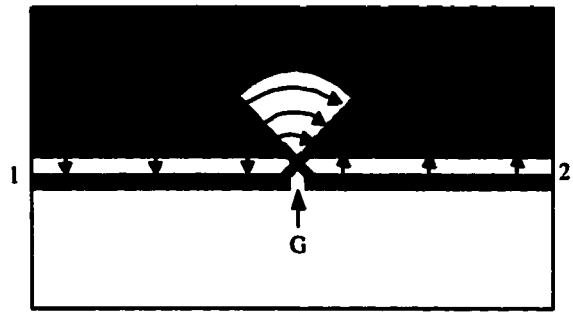

(a)

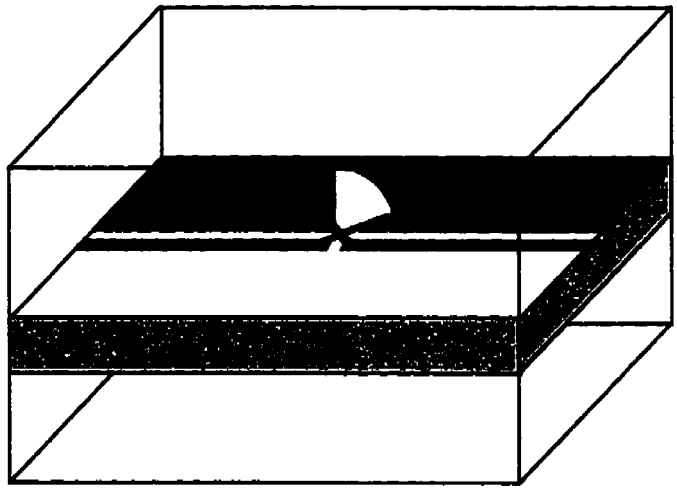

(b)

Figure 2.4 Coplanar stripline phase inverter (a) circuit layout and (b) geometrical model for finite element analysis.

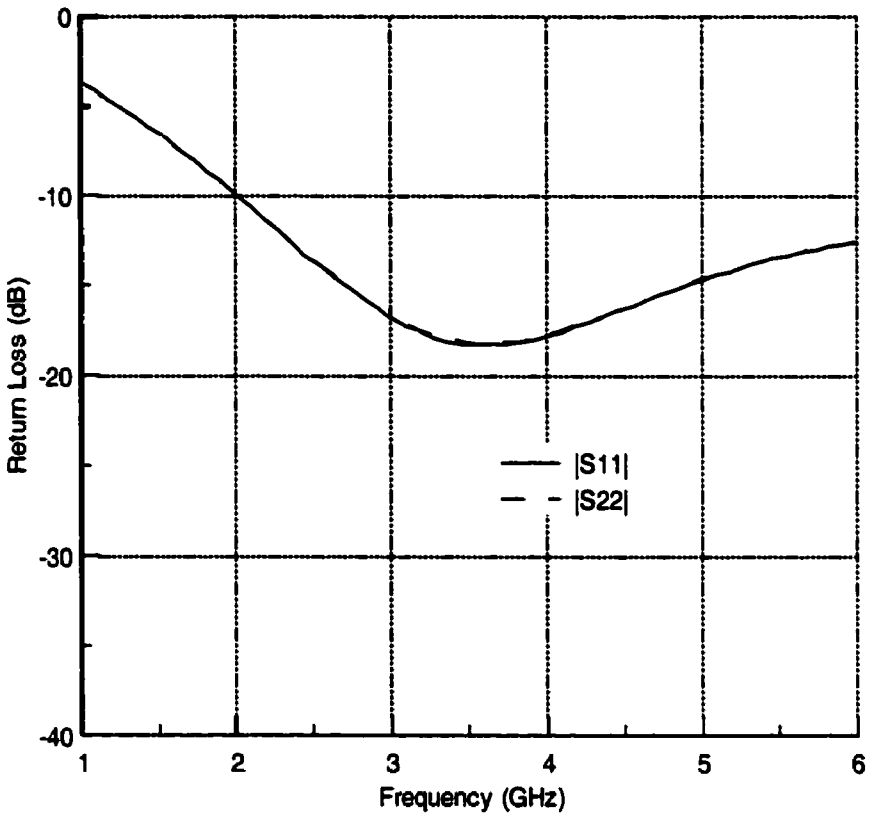

Figure 2.5(a) Calculated frequency responses of return loss for the phase inverter shown in Figure 2.4(b)

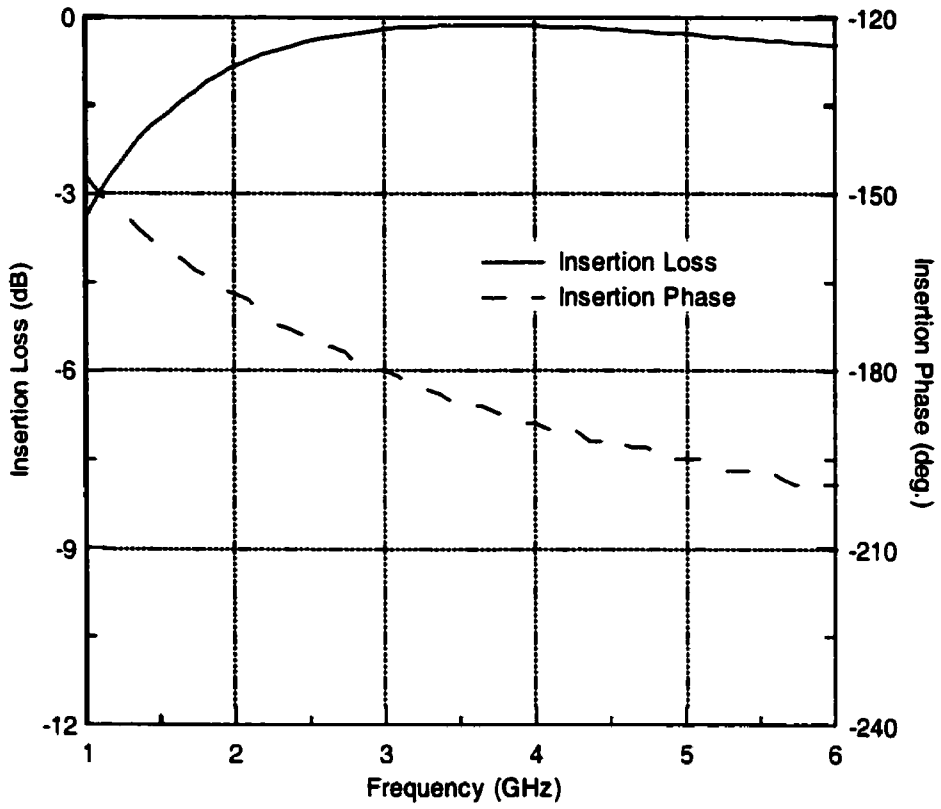

Figure 2.5(b) Calculated frequency responses of insertion loss and phase for the phase inverter shown in Figure 2.4(b)

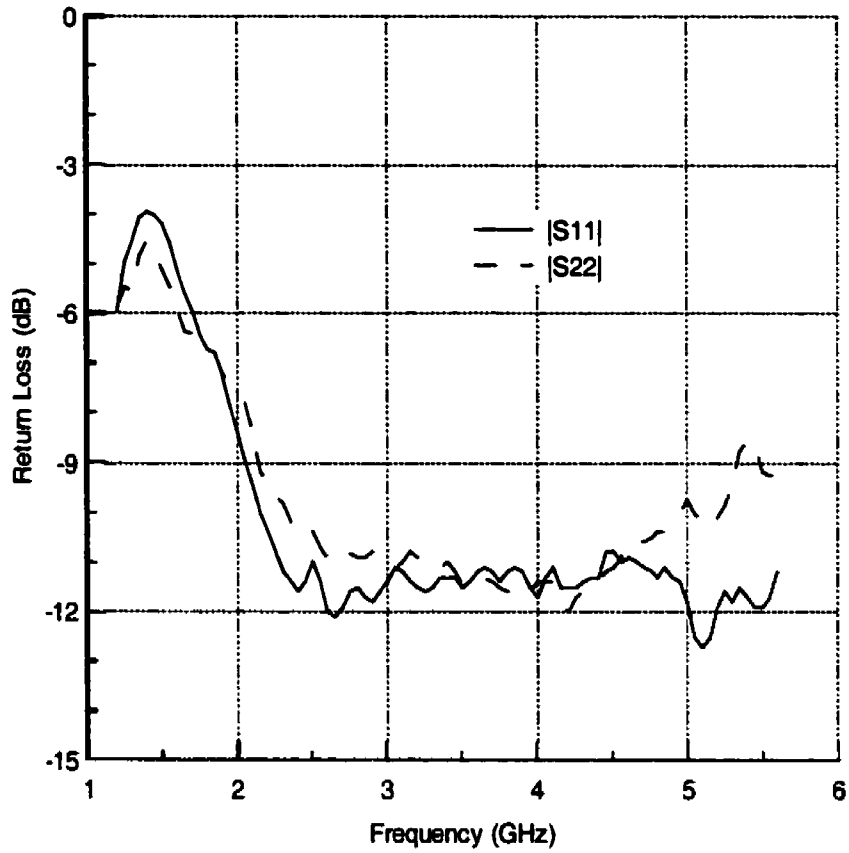

Figure 2.6(a) Measured frequency responses of return loss for the phase inverter shown in Figure 2.4(a)

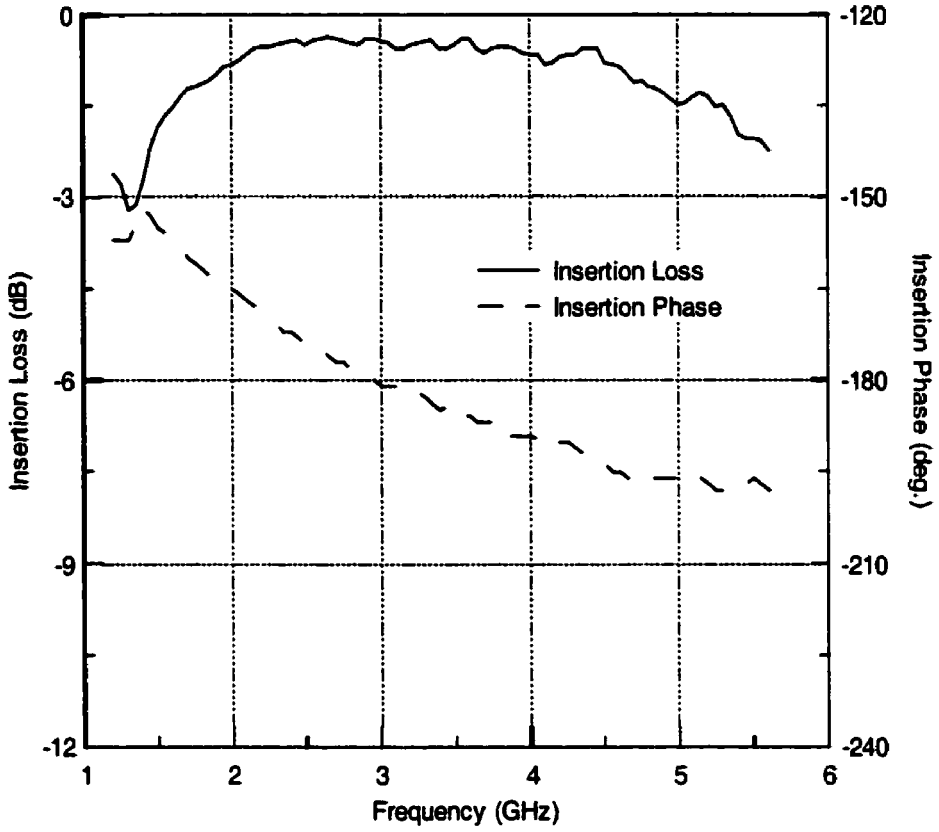

Figure 2.6(b) Measured frequency responses of insertion loss and phase for the phase inverter shown in Figure 2.4(a)

Chapter III

Analysis and Design of Series-Type Ring Coupler with Phase Inverter

3.1 Introduction

Hybrid couplers are indispensable components used in various microwave and millimeter-wave integrated circuit applications such as balanced amplifiers, balanced mixers, phase shifters, and feeding networks in antenna arrays. One of the most commonly used hybrid coupler is a rat-race hybrid ring. The main advantage of the ring coupler is that its isolation between two input ports may be independent of the value of two balanced terminating impedances. The conventional rat-race ring consists of three one-quarter-wavelength sections and one three-quarter-wavelength section. The circumference of the entire ring is equal to one and half wavelength. The drawback of the conventional ring hybrid is large size and limited usable bandwidth due to the three-quarter-wavelength section. Over the last decades, several design techniques have been developed to extend the operating bandwidth and reduce the size. One technique is to use one-quarter wavelength section with phase inverter to replace the conventional three-quarter wavelength section. As discussed in the previous chapter, the phase inverter circuits can easily be realized in uniplanar structure. It is known that the ring couplers can be divided into three categories: series-type, parallel-type, and magic-T. In this chapter, we will present analysis and design of the series-type uniplanar ring couplers with phase inverter. Design of the parallel-type ring coupler with phase inverter and magic-T will be discussed in Chapters IV and V, respectively.

In the following, we will present analysis of the series-type uniplanar ring coupler with phase inverter. Principal features and design considerations of the ring coupler are summarized. A general design equation is also given in the second section. The third section describes 3-dB ring coupler design. The design criteria for broadband and narrow-band applications are discussed in detail. To verify the design theory, a coplanar stripline ring coupler with phase inverter was developed and tested. Calculated and measured circuit performances are presented and discussed in the fourth section.

3.2 Analysis of the series-type ring coupler with phase inverter

In the following, we will present the analysis of a series-type ring coupler with phase inverter. A schematic diagram of series-type ring coupler with an ideal phase inverter is sketched in Figure 3.1. The coupler consists of four transmission line sections on the ring. Electrical length and characteristic impedance of each section are described as follows. Symbol Z_0 in Figure 3.1 stands for the characteristic impedance of attached feed lines (or input/output lines). The voltage reference for each port is denoted by lines with an arrow. Without loss of generality, a sub-network having a 180° phase shift represents the ideal phase inverter. Electrical characteristics of the sub-network can be described by such a two-port S-parameter matrix as

$$S = \begin{bmatrix} 0 & -1 \\ -1 & 0 \end{bmatrix} \tag{3.1}$$

It is easily shown that electrical behaviour of a line section including the phase inverter remains the same regardless of the location of phase inverter. To simplify the following analysis, we place the phase inverter at the middle of the line section. It is obvious that the coupler has a symmetric axis, which is denoted by a cross-line A-A.

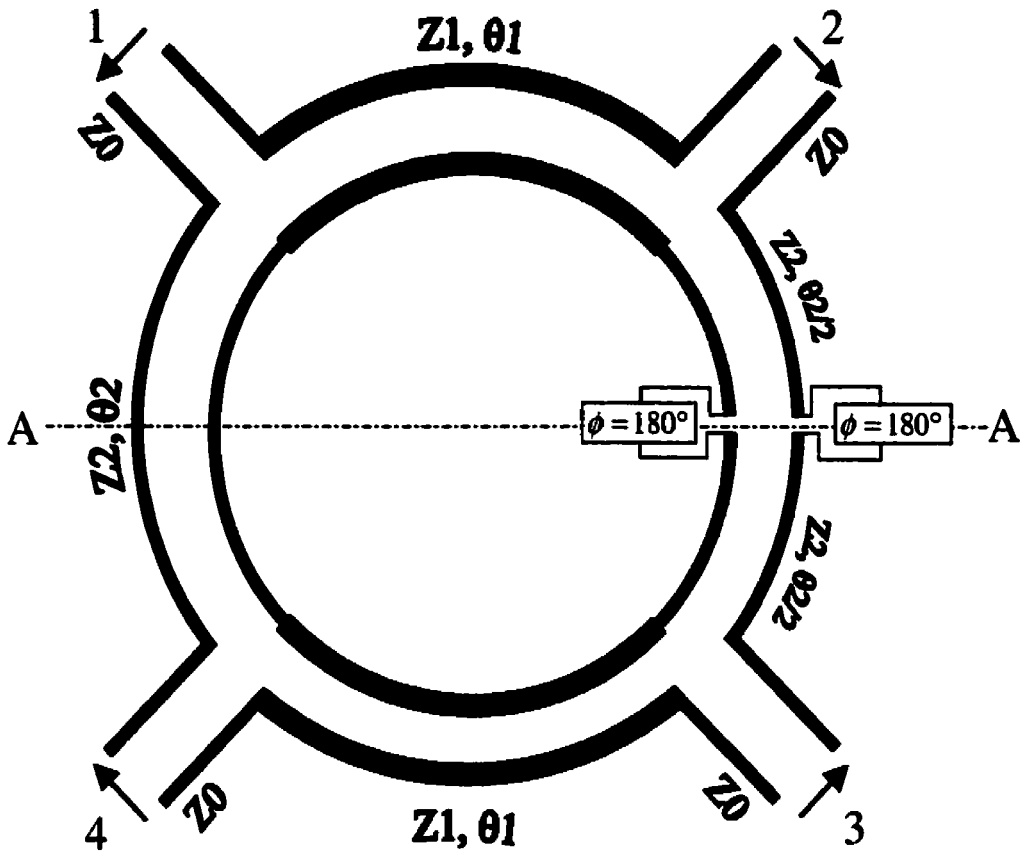

Figure 3.1 A schematic diagram of series-type ring coupler with ideal phase inverter

Generally speaking, the electrical characteristics of a coupler can simply be described by a four-port S-parameter matrix given by

$$S = \begin{bmatrix} S_{11} & S_{12} & S_{13} & S_{14} \\ S_{21} & S_{22} & S_{23} & S_{24} \\ S_{31} & S_{32} & S_{33} & S_{34} \\ S_{41} & S_{42} & S_{43} & S_{44} \end{bmatrix} \tag{3.2}$$

Since the coupler circuit is symmetrical with respect to the cross-line A-A, we have

$$\begin{aligned} S_{11} &= S_{44} \\ S_{22} &= S_{33} \\ S_{12} &= S_{43} \\ S_{13} &= S_{42} \end{aligned} \tag{3.3}$$

With (3.3) and the reciprocity of passive circuit, we can rewrite the S-parameter matrix (3.2) as the following simplified form.

$$S = \begin{bmatrix} S_{11} & S_{12} & S_{13} & S_{14} \\ S_{12} & S_{22} & S_{23} & S_{13} \\ S_{13} & S_{23} & S_{22} & S_{12} \\ S_{14} & S_{13} & S_{12} & S_{11} \end{bmatrix} \tag{3.4}$$

It is known that a symmetrical four-port network can simply be analyzed by using a conventional even- and odd-mode analysis technique. Under the even- and odd-mode excitation, the ring coupler can be decomposed into a pair of two-port networks as shown in Figure 3.2. Obviously, the S-parameters of the ring coupler can be obtained from the relationship given below.

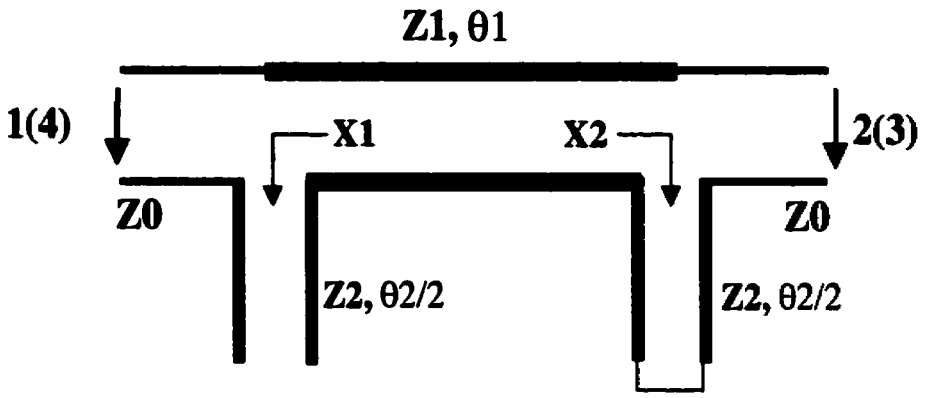

(a)

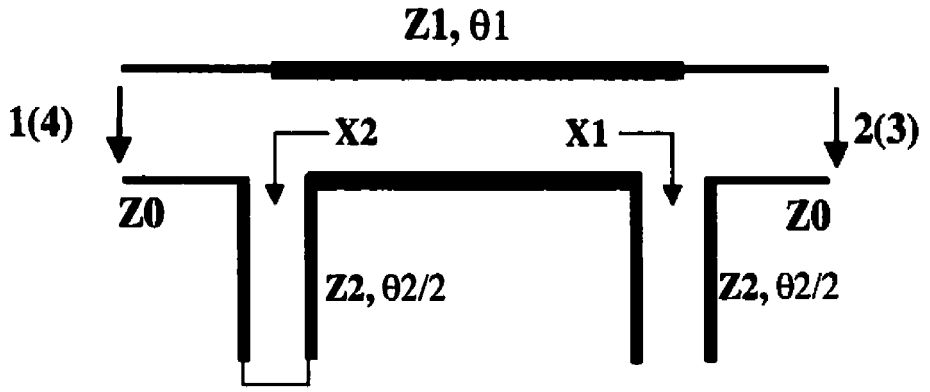

(b)

Figure 3.2 Equivalent circuits for even/odd mode excitation. (a) Even-mode and (b) odd-mode.

$$
\begin{aligned}
S_{11} &= (S_{11e} + S_{11o})/2 \\
S_{22} &= (S_{22e} + S_{22o})/2 \\
S_{12} &= (S_{12e} + S_{12o})/2 \\
S_{13} &= (S_{12e} - S_{12o})/2 \\
S_{14} &= (S_{11e} - S_{11o})/2 \\
S_{23} &= (S_{22e} - S_{22o})/2
\end{aligned}
\tag{3.5}
$$

where S-parameters with subscripts e and o stand for the S-parameters of two-port networks as shown in Figure 3.2 (a) and (b), respectively.

In Figure 3.2, both circuits can be treated as the cascades of three two-port sub-networks. Characteristics for the overall circuit can be obtained by using analysis of the cascaded ABCD matrix. The input impedance for the series stubs can be written as

$$
\begin{cases}
X_1 = -j \cdot \dfrac{Z_2}{\tan\left(\dfrac{\theta_2}{2}\right)} \\
X_2 = j \cdot Z_2 \cdot \tan\left(\dfrac{\theta_2}{2}\right)
\end{cases}
\tag{3.6}
$$

With a straightforward analytical manipulation, we can derive the following set of equations for the S-parameters.

$$
\begin{aligned}
S_{11} &= S_{22} = \frac{\cos\theta_1 \cdot Y_0 \cdot (X_1 + X_2) + K_s}{N_s} \\
S_{12} &= \frac{2}{N_s} \\
S_{13} &= 0 \\
S_{14} &= -S_{23} = \frac{j \cdot Y_1 \cdot \sin\theta_1 \cdot (X_1 - X_2)}{N_s}
\end{aligned}
\tag{3.7}
$$

in which

$$
\begin{aligned}
K_s &= j \cdot Y_0 \cdot Z_1 \cdot \sin\theta_1 \cdot (1 + X_1 \cdot X_2 \cdot Y_1^2 - Z_0^2 \cdot Y_1^2) \\
N_s &= 2 \cdot \cos\theta_1 + (j \cdot Y_1 \cdot \sin\theta_1 + \cos\theta_1 \cdot Y_0) \cdot (X_1 + X_2) + H_s \\
H_s &= j \cdot Y_0 \cdot Z_1 \cdot \sin\theta_1 \cdot (1 + X_1 \cdot X_2 \cdot Y_1^2 + Z_0^2 \cdot Y_1^2) \\
Y_0 &= 1/Z_0 \\
Y_1 &= 1/Z_1
\end{aligned}
\tag{3.8}
$$

The perfect match condition of the input/output ports requires that S_{11} and S_{22} be zero. This leads to a simple relation as follows

$$
2 \cdot Z_2 \cdot \cot\theta_1 \cdot \cot\theta_2 = Z_1 \cdot (1 + Z_2^2 \cdot Y_1^2 - Z_0^2 \cdot Y_1^2) \tag{3.9}
$$

From (3.7), the amplitude imbalance between the two output ports is written as

$$
\left|\frac{S_{12}}{S_{14}}\right| = \left|\frac{S_{12}}{S_{23}}\right| = \left|\frac{Z_1 \cdot \sin\theta_2}{Z_2 \cdot \sin\theta_1}\right| \tag{3.10}
$$

It is well known that, for a lossless, passive and linear four-port network, S-parameters must obey the unity condition or power conservation condition

$$
S \cdot S_t^* = I \tag{3.11}
$$

In which S_t^* refers to the transpose and complex conjugate counterpart of S, I is the unit matrix.

With (3.10) and (3.11), we can obtain a pair of equations

$$|S_{12}|^2 = \frac{(1-|S_{11}|^2)\cdot|Z_1\cdot\sin\theta_2|^2}{|Z_2\cdot\sin\theta_1|^2+|Z_1\cdot\sin\theta_2|^2}$$

$$|S_{14}|^2 = \frac{(1-|S_{11}|^2)\cdot|Z_2\cdot\sin\theta_1|^2}{|Z_2\cdot\sin\theta_1|^2+|Z_1\cdot\sin\theta_2|^2} \tag{3.12}$$

Obviously, the above theory is general, and may apply to the analysis and design of a ring coupler with ideal phase inverter and any arbitrary power ratio.

From the above equations, we can summarize principal features and electrical characteristics of a ring coupler with phase inverter as follows.

(a) The signal isolation between the two output ports is perfect and it is independent of frequency since $s_{13} = s_{24} = 0$ as long as the general network condition is upheld.

(b) The phase difference between the two output ports is 0°/180° and it is also independent of frequency since $ang(s_{12}/s_{14}) = 0°$ and $ang(s_{12}/s_{23}) = 180°$.

(c) The power-split ratio between the two output ports is proportional to the square of the term $\left|\frac{Z_1\cdot\sin\theta_2}{Z_2\cdot\sin\theta_1}\right|$. If $\theta_1 = \theta_2$, such a power split ratio is obviously proportional to the square of the ratio of the two impedance variables of the ring and it is independent of frequency.

3.3 Design of 3-dB ring coupler with phase inverter

Generally speaking, coupler design is concerned with the determination of circuit parameters such that certain pre-designated performance specifications can be met over a frequency band of interest. These specifications refer usually to factors such as coupling,

matching, and isolation. As discussed above, the isolation for a ring coupler with phase inverter can be perfect and is frequency-independent. Therefore, we need to only look into design aspects of coupling and matching conditions. In the design of a 3-dB coupler, the two output ports are required to be equal. With (3.10), we can obtain

$$Z_1 = Z_2 \cdot \frac{\sin\theta_1}{\sin\theta_2} \tag{3.13}$$

Note that the absolute sign in (3.13) is eliminated to consider that $\theta_1, \theta_2 < 180^\circ$. This is a typical case in coupler design.

With (3.13) and the perfect matching condition formulated in (3.9), a pair of design equations for a series-type 3 dB ring coupler with phase inverter can be obtained as

$$\begin{aligned} Y_1 &= Y_0 \cdot \frac{\sqrt{2-(\cos\theta_1+\cos\theta_2)^2}}{\sin\theta_1} \\ Y_2 &= Y_0 \cdot \frac{\sqrt{2-(\cos\theta_1+\cos\theta_2)^2}}{\sin\theta_2} \end{aligned} \tag{3.14}$$

Where $Y_2 = 1/Z_2$. From (3.14), it is seen that there are two degrees of freedom in the coupler design related to the choice of θ_1 and θ_2. Of course, they depend on the expected center frequency and other relevant requirements, for example, operating bandwidth or circuit size. Since the characteristic impedance Z_1, Z_2 of ring transmission lines have to be larger than zero, the following constraint for θ_1 and θ_2 is established.

$$\theta_1 + \theta_2 > 65.53^\circ \tag{3.15}$$

Considering the bandwidth specification, the coupler design may be classified into two categories: broadband and narrow-band.

A) *Broadband design*

From (3.10), it is seen that the two output ports are perfectly balanced and also they are frequency-independent if $\theta_1 = \theta_2 = \theta$ and $Y_1 = Y_2 = Y$. For a broadband design, the circuit parameters of each ring section should be, therefore, set to be the same while the phase inverter is ignored. Since frequency response of coupling and input matching (or return loss) of the coupler is expected to be symmetrical with respect to the axis $\theta = 90°$, it can be shown that the maximum possible bandwidth for certain specifications is achieved with $\theta = 90°$ at the designated center frequency. In the conventional design, the input/output lines are perfectly matched at the center frequency. In general, the coupling and matching conditions for a broadband application are required only to meet certain tolerance limits over a specific bandwidth of interest even though the circuit may not be matched perfectly at the center frequency. With this argument in mind, we develop a procedure for a broadband coupler design as follows.

With the conditions $\theta_1 = \theta_2 = \theta$ and $Y_1 = Y_2 = Y$, the following relationship can be obtained from (3.7), (3.9), and (3.12)

$$|S_{12}|^2 = |S_{14}|^2 = \frac{1}{2} \cdot \left(1 - |S_{11}|^2\right)$$

$$S_{11} = \frac{(4Z^2 - Z_0^2)\cos 2\theta + Z_0^2}{(4Z^2 + Z_0^2)\cos 2\theta - Z_0^2 + j4ZZ_0 \sin 2\theta} \tag{3.16}$$

$$Y = Y_0 \cdot \sqrt{2(1 - \cot^2 \theta)}$$

with $Z = 1/Y$

From this relationship, it is seen that the series-type ring coupler design can be simplified into a design of input matching condition. In terms of (3.16), it is obvious that if the circuit is matched at θ_m, it is also simultaneously matched at $180^\circ - \theta_m$. These two matching points are actually overlapped at the center frequency in the conventional design. Since the frequency response is symmetrical with respect to the axis point $\theta = 90^\circ$. The maximum effective bandwidth can be obtained only if the maximum in-band return loss is located at the center frequency ($\theta = 90^\circ$). Thus, the new proposed broadband design can be interpreted as a technique allowing the displacement of the two matching points away from the classical design point which is at the center frequency. The circuit parameters can be calculated once the return loss is defined at the center frequency for the in-band specification.

With the above discussion, the design equations for the series-type 3-dB ring coupler are given below

$$Y = Y_0 \cdot \sqrt{2\left(1 - \frac{2}{1+10^{-\frac{L}{20}}}\right)} \qquad (3.17)$$

$\theta = 90^0$ (at the center frequency)

Where L is the in-band maximum return loss specification. Clearly, the characteristic admittance Y must meet the following condition.

$$Y \le Y_0 \cdot \sqrt{2} \qquad (3.18)$$

B) *Narrow-band design*

In some cases, the bandwidth may not be the primary concern in the coupler design. On the contrary, a narrow-band operation is desirable. Therefore, the input impedance should be matched at the center frequency as in case of the conventional design. The relevant

circuit parameters can be usually calculated from (3.14). Since there are two degrees of freedom related to the choice of θ_1 and θ_2, these circuit parameters could be arbitrary. In practice, we prefer to have a compact coupler size. This requirement leads to the narrow-band design equations as below

$$Y_1 = Y_0 \cdot \frac{\sqrt{2-(\cos\theta_1+\cos\theta_2)^2}}{\sin\theta_1}$$

$$Y_2 = Y_0 \cdot \frac{\sqrt{2-(\cos\theta_1+\cos\theta_2)^2}}{\sin\theta_2} \qquad (3.19)$$

$$\textit{Minimize}\ (\theta_1+\theta_2) \qquad \text{under certain fabrication requirements}$$

It can be seen from (3.15) that the circumference of a size-reduced coupler for the narrow-band application must be larger than $3\lambda_g/8$.

3.4 Numerical and experimental results for a coplanar stripline ring coupler

The analysis and design criteria for the series-type ring coupler have been presented in the above sections. To validate the developed design theory, this section presents numerical and experimental results for a 3-dB coplanar stripline ring coupler with phase inverter. In the following, we first give a brief description of the ring coupler circuit. Then, numerical results for the coupler are calculated using the full-wave analysis based on a finite element technique. Experimental results are also presented and discussed in detail.

3.4.1 Description of a coplanar stripline ring coupler circuit

Figure 3.3 illustrates the physical configuration of a 3-dB coplanar stripline ring coupler with phase inverter. The ring coupler consists of four coplanar stripline T-junctions and four quarter-wavelength coplanar stripline sections. One of the four coplanar stripline

sections has a phase inverter, which is realized by a two-strip crossover. As discussed in the previous chapter, the stripline crossover produces additional 180° phase shift over a broadband. The uniplanar ring coupler was built on a RT/Duriod 6010 ($\varepsilon_r = 10.2$) substrate with thickness $h = 1.27$ mm. Characteristic impedance for feed lines was chosen to be 100 Ω with the following dimensions: the strip width $W = 0.30$ mm and the gap size between two strips $S = 0.28$ mm. Using (3.17) for the design requirement of –20 dB return loss, we can obtain the characteristic impedance for the quarter-wavelength section as 78.2 Ω, which corresponds to $W = 0.52$ mm and $S = 0.20$ mm. The coplanar stripline ring has the mean radius $r = 10$ mm. The gap dimension for the two-strip crossover is $G = 0.20$ mm.

3.4.2 Numerical Results

The performance of the ring coupler described above was calculated using the commercial software HFSS developed by Ansoft. Figure 3.4 shows the geometry of the coupler used in the performance calculation. A virtual box was introduced to define the field solution area. Radiation boundaries were assigned to the surfaces of the virtual box in analysis to consider the unbounded effect of the circuit. To minimize computational efforts, the virtual box was chosen to have dimensions of $30\times30\times30$ mm^3. The dimensions for all of the feeding ports are 8×8 mm^2. The crossover for 180° phase shift was modeled by an airbridge with a square cross-section (0.2×0.2 mm^2). Calculated frequency responses for return loss, coupling, isolation and phase difference are shown in Figure 3.5.

Figure 3.5(a) shows that the return loss for $|S_{11}|$ and $|S_{44}|$ is better than -20 dB from 1.9 GHz to 3.3 GHz. The two matching points are clearly observed in the frequency range as predicted by the developed theory. For the same requirement, the effective bandwidth for $|S_{22}|$ and $|S_{33}|$ is about 0.9 GHz from 2.1-3.0 GHz. The bandwidth

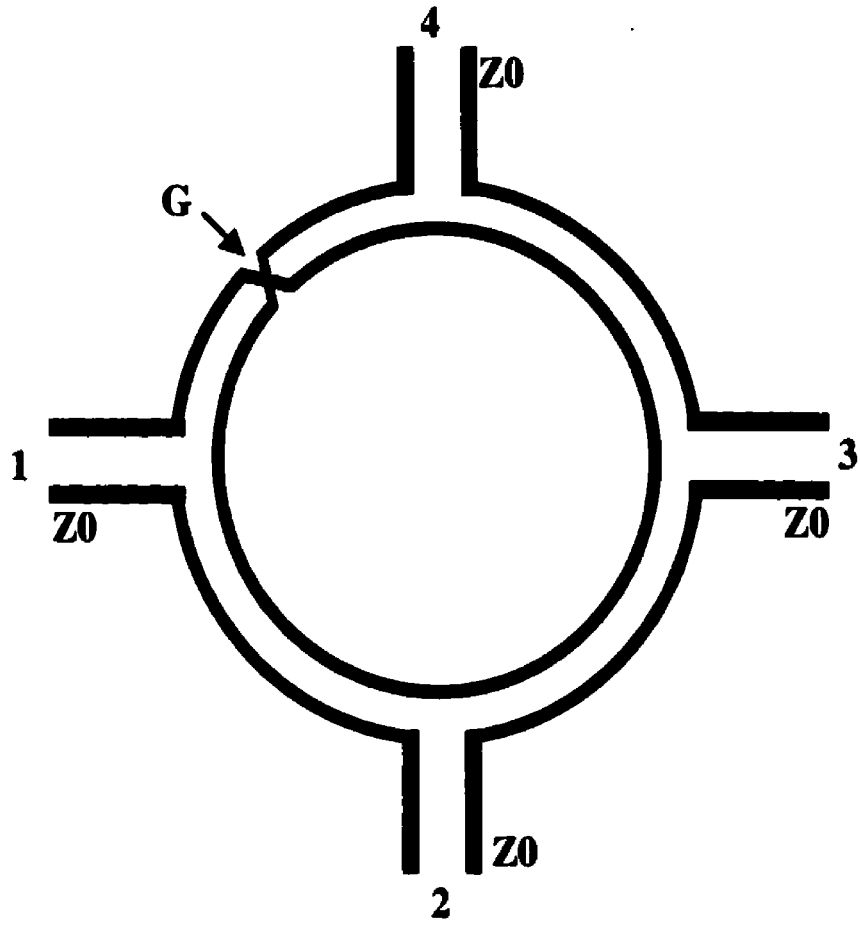

Figure 3.3 Physical configuration of a coplanar stripline ring coupler with phase inverter.

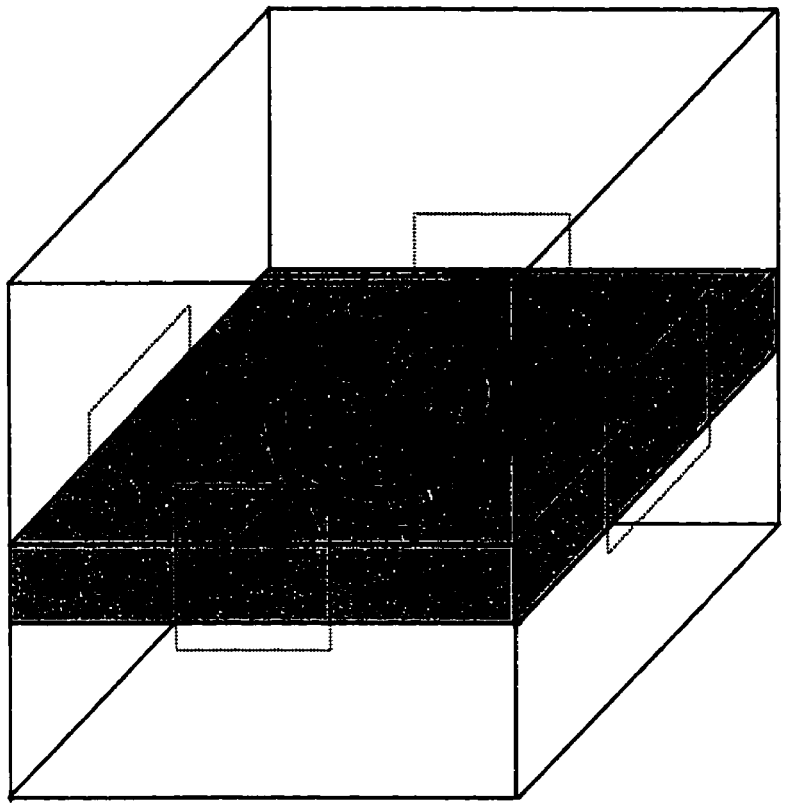

Figure 3.4 Geometry of the coplanar stripline ring coupler for the finite element analysis

reduction for $|S_{22}|$ and $|S_{33}|$ is essentially caused by the imperfection of the phase inverter as discussed in the previous chapter. It may also be attributed to the two-strip crossover, which adds additional physical length to the section. In Figure 3.5(b), it is seen that the coupling for all ports is within -3.7 ± 0.5 dB from 1.6 - 3.0 GHz. The extra insertion loss for the outputs may be caused by radiation of the coplanar stripline. The mutual isolation of ports 1(2) and 3(4) is shown in Figure 3.5(c). It is seen that the isolation is better than -20 dB from 1.0 - 3.4 GHz. Figure 3.5(d) shows the phase difference for the in-phase and 180° out of phase mode coupling. The phase error is less than $\pm 5°$ in the frequency range of 1.3 - 3.3 GHz. In summary, the calculated results show that the proposed ring coupler has a fairly good performance. It validates the design theory, which was developed in the previous section.

3.4.3 Experiment results

Measured performance of the proposed ring coupler is shown in Figure 3.6. The measurement was made using GGB probes (40A-GS-750) and a vector network analyzer (HP 8720ES). A TRL calibration was used to remove the system errors of the test station. For each measurement, a two-port S-parameter was obtained under the condition of terminating the other two ports of the ring coupler. The termination for each port was implemented by soldering a 100 Ω chip resistor to the coplanar stripline. Figure 3.6(a) shows the measured frequency response of return loss for all ports of the ring coupler. It is seen that the return loss is better than -15 dB in the frequency range of 1.4 - 2.4 GHz, which generally agrees with the calculated results. Measured frequency response of coupling for output ports is shown in Figure 3.6(b). The coupling for all the ports is within -3.6 ± 0.8 dB from 1.0 - 2.3 GHz. Figure 3.6(c) shows measured mutual isolation between ports 1(2) and 3(4)). It is seen that the mutual isolation is better than -20 dB in the frequency range of 1.0 - 2.2 GHz, which agrees with the calculated one as shown in Figure 3.5(c). Measured phase difference for the in-phase and 180° out of phase mode coupling is shown in Figure 3.6(d). The phase error is less than $\pm 4°$ in the frequency

range of 1.0 - 2.3 GHz. It should be noted that the above measured results include the effect of the imperfection of termination resistors.

3.5 Conclusion

In this chapter, analysis of the series-type uniplanar ring coupler with phase inverter has been presented. Principal features and design considerations for the ring coupler are summarized. A general design equation is also derived. The design criteria of the 3-dB ring coupler for broadband and narrow-band applications are discussed. A coplanar stripline ring coupler was designed and tested to validate the developed design theory. Numerical and experimental results were presented and discussed in detail.

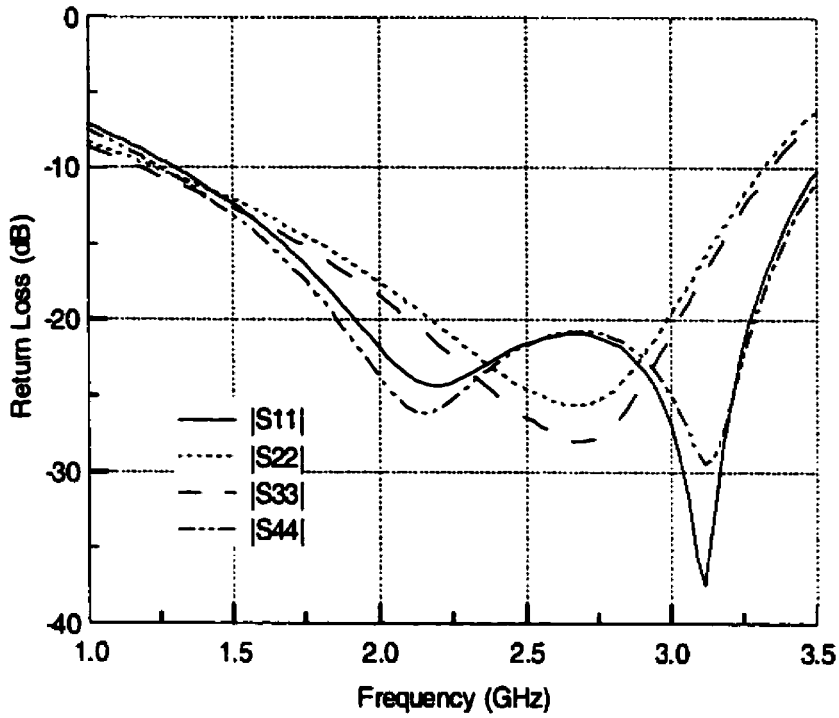

Figure 3.5(a) Calculated frequency responses of return loss for the four input ports of the ring coupler shown in Figure 3.4

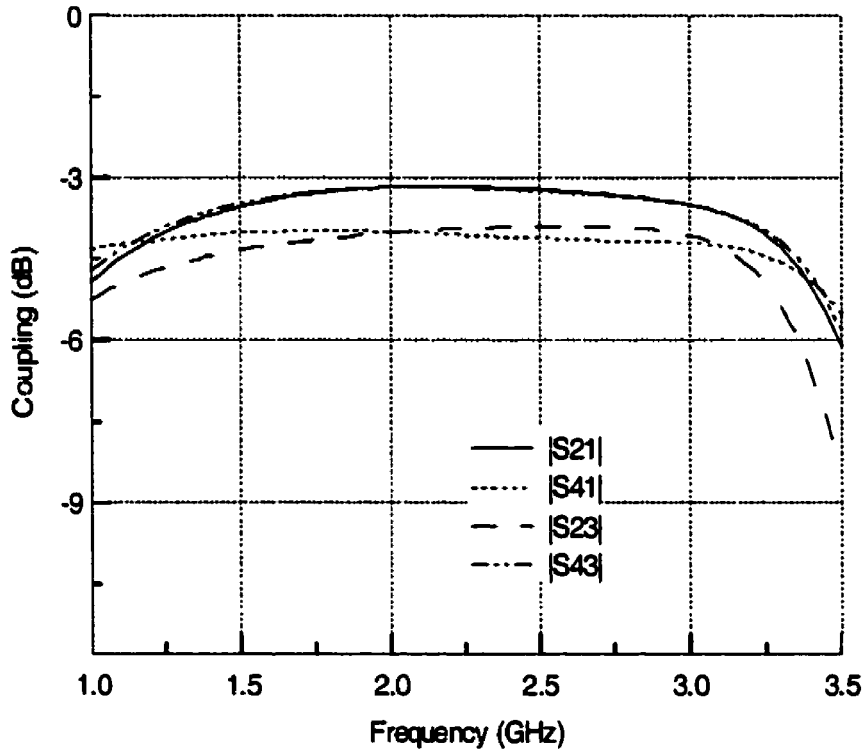

Figure 3.5(b) Calculated frequency responses of coupling for the ring coupler shown in Figure 3.4

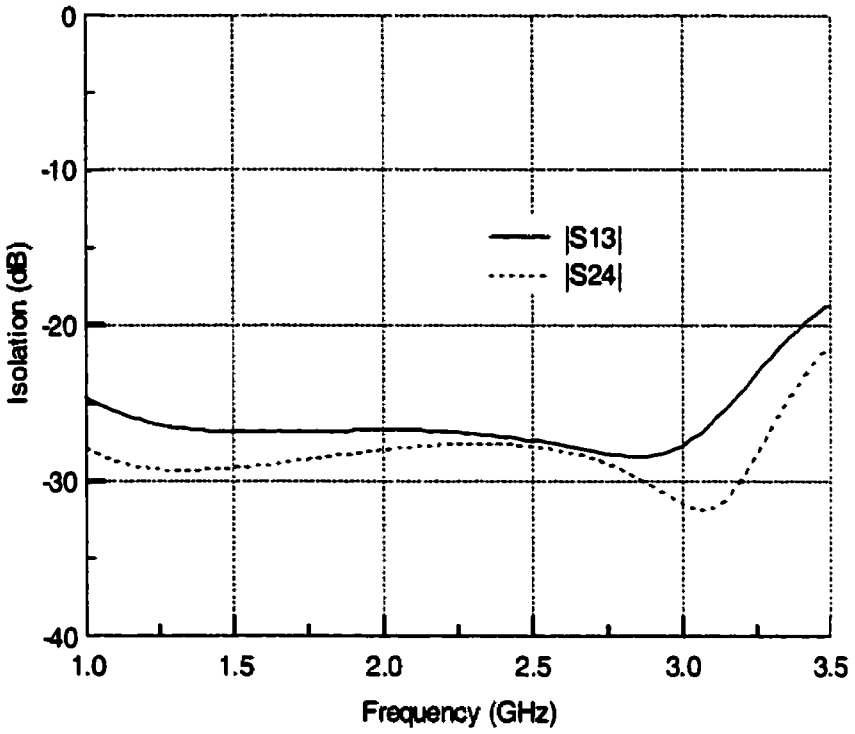

Figure 3.5(c) Calculated frequency responses of the mutual isolation for the ring coupler shown in Figure 3.4

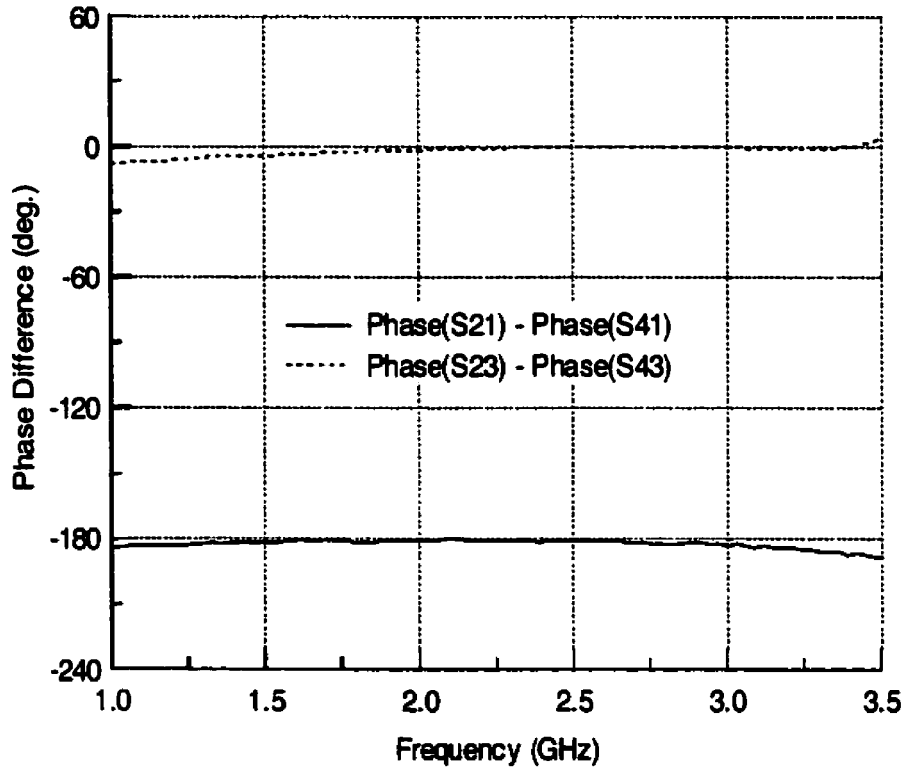

Figure 3.5(d) Calculated phase difference between output ports 2 and 4 for the ring coupler shown in Figure 3.4

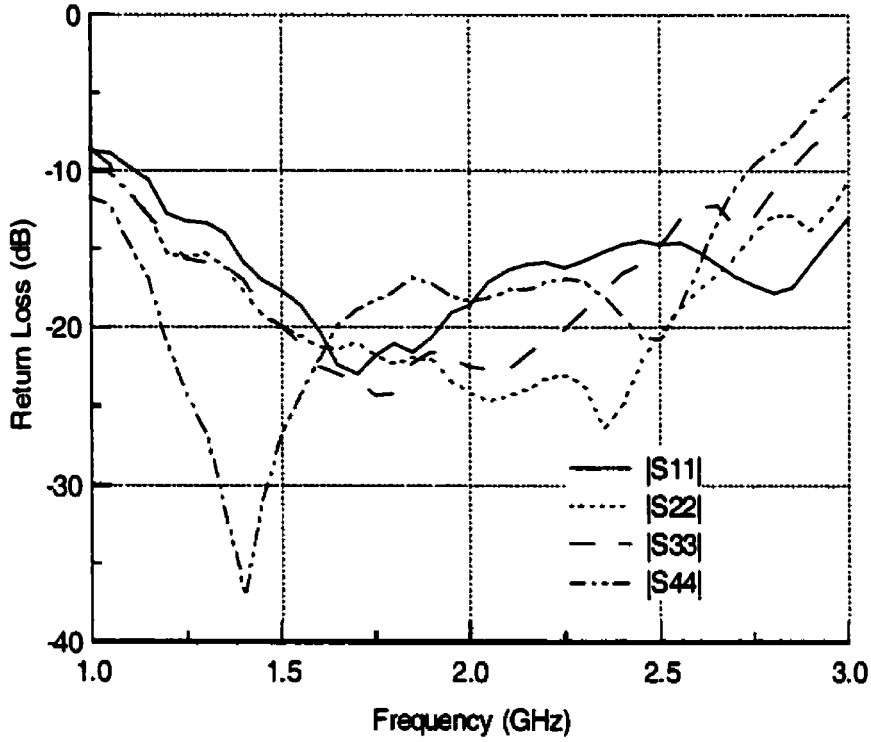

Figure 3.6(a) Measured frequency responses of return loss for the four input ports of the ring coupler shown in Figure 3.3

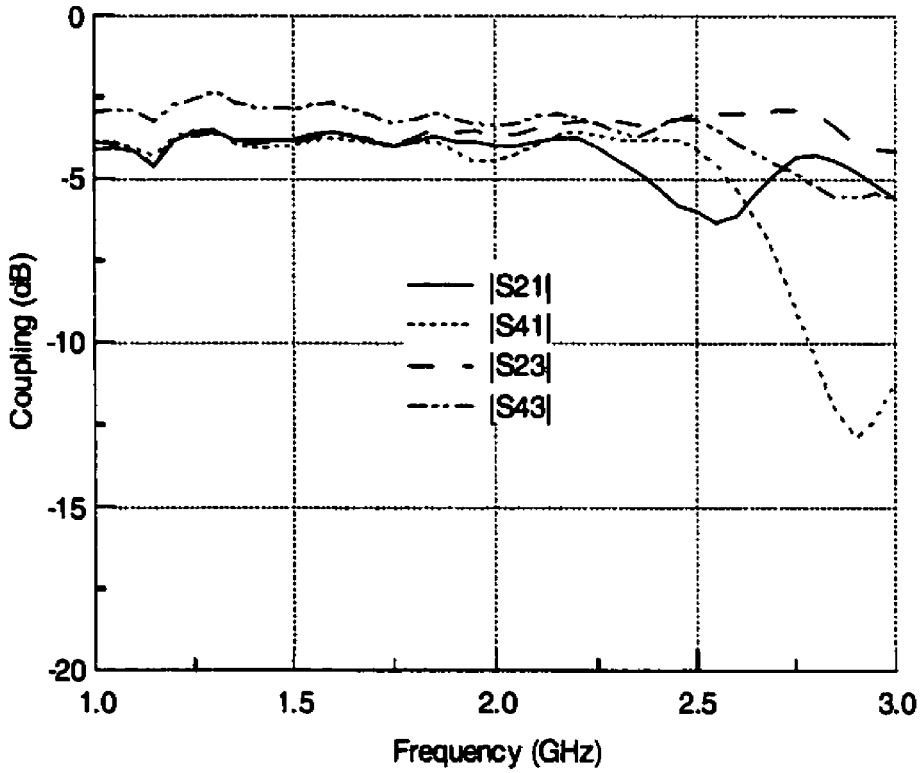

Figure 3.6(b) Measured frequency responses of coupling for the ring coupler shown in Figure 3.3

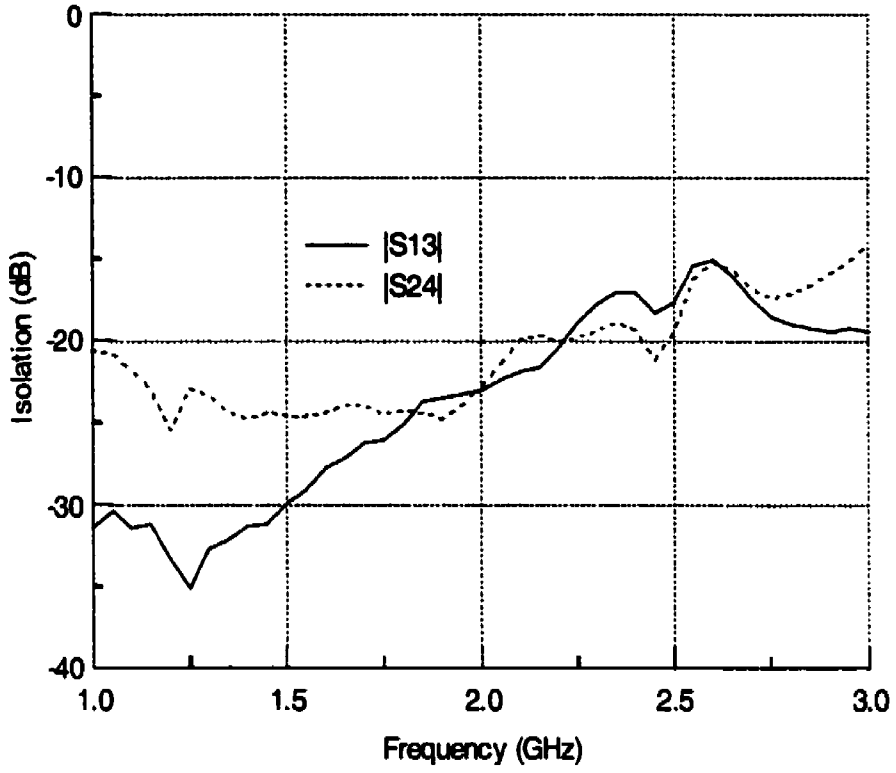

Figure 3.6(c) Measured frequency responses of the mutual isolation for the ring coupler shown in Figure 3.3

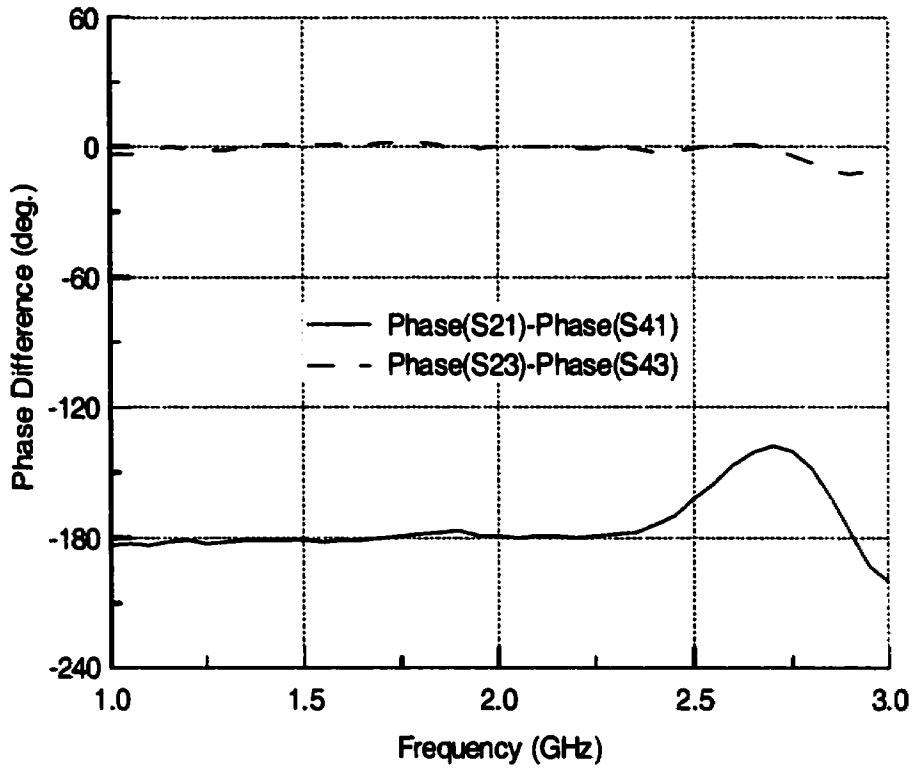

Figure 3.6(d) Measured phase difference between output ports 2 and 4 for the ring coupler shown in Figure 3.3

Chapter IV

Analysis and Design of Parallel-Type Ring Coupler with Phase Inverter

4.1 Introduction

In the previous chapter, we presented the analysis and design of the series-type ring coupler with phase inverter. In this chapter, we address the analysis and design of the parallel-type ring coupler with phase inverter. Since the design of the parallel-type ring coupler with phase inverter has been discussed in [14], only a brief description on the analysis will be given in this chapter. After the brief discussion on the analysis, a micro-coplanar stripline ring coupler will be presented. Electrical performance of the coupler is obtained by using a finite element technique. Calculated and measured results are presented and discussed in detail.

4.2 Analysis of parallel-type ring coupler with phase inverter

Figure 4.1 shows the schematic diagram of a parallel-type ring coupler with an ideal phase inverter. The coupler consists of four transmission line sections on the ring. One of the four sections has a phase inverter, which is illustrated by a sub-network with a 180^0 phase shift. Electrical lengths and characteristic admittances of the transmission lines on the ring are described in the figure. Symbol Y_0 in Figure 4.1 denotes the characteristic admittance of feed lines. The voltage reference for each port is denoted by the arrow lines. As discussed before, we place the phase inverter in the middle of the transmission line section. Clearly, the coupler circuit is symmetrical to the axis A-A.

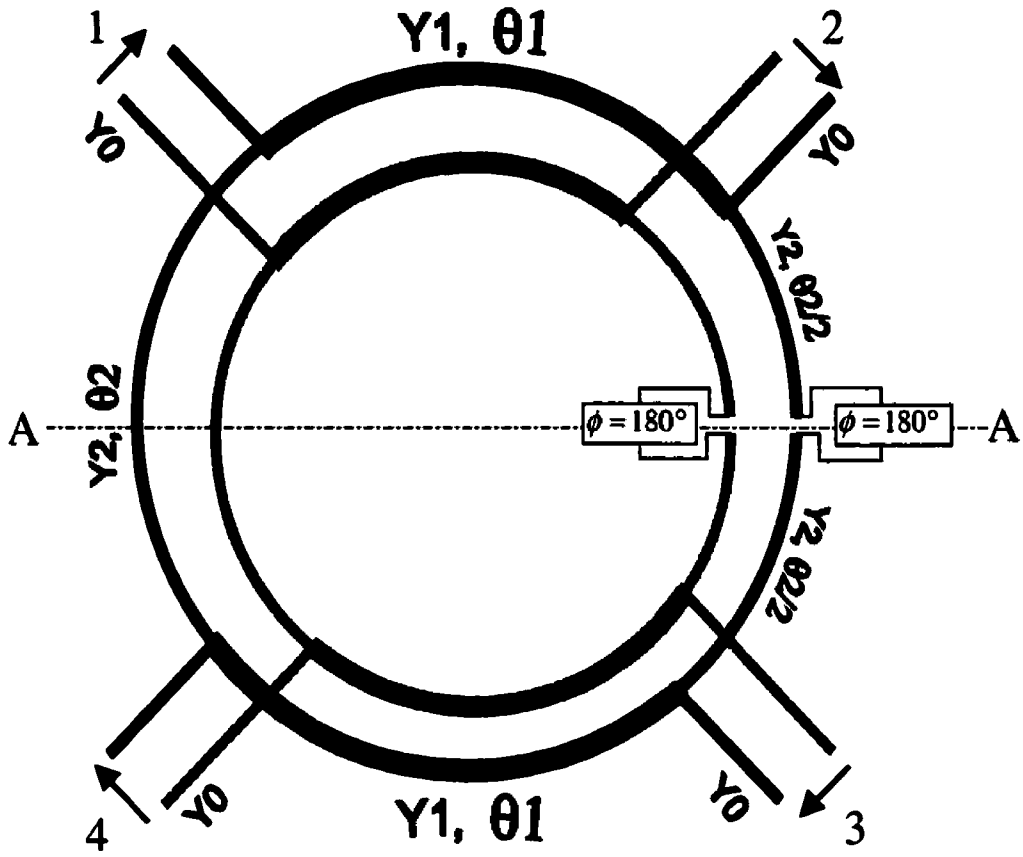

Figure 4.1 A schematic diagram of parallel-type ring coupler with ideal phase inverter

In view of the symmetry and reciprocity of the ring coupler circuit, its electrical performance can be characterized by the following four-port S-parameter matrix

$$S=\begin{bmatrix} S_{11} & S_{12} & S_{13} & S_{14} \\ S_{12} & S_{22} & S_{23} & S_{13} \\ S_{13} & S_{23} & S_{22} & S_{12} \\ S_{14} & S_{13} & S_{12} & S_{11} \end{bmatrix} \tag{4.1}$$

It is known that a symmetrical four-port network can be simply analyzed by using a conventional even- and odd-mode analysis technique. With the even- and odd-mode excitation, the ring coupler can be decomposed into a pair of two-port networks as shown in Figure 4.2. The S-parameters of the ring coupler can be obtained using (3.5). The input admittance for the parallel stubs can be written as

$$\begin{cases} B_1 = j \cdot Y_2 \cdot \tan\left(\dfrac{\theta_2}{2}\right) \\ B_2 = -j \cdot \dfrac{Y_2}{\tan\left(\dfrac{\theta_2}{2}\right)} \end{cases} \tag{4.2}$$

The circuit shown in Figure 4.2(a) can be treated as cascaded three two-port sub-networks. Using the analysis of ABCD matrix, characteristics of the overall circuit can be described by the following matrix

$$\begin{aligned} \begin{bmatrix} a_e & b_e \\ c_e & d_e \end{bmatrix}_{even-mode} &= \begin{bmatrix} 1 & 0 \\ B_1 & 1 \end{bmatrix} \cdot \begin{bmatrix} \cos\theta_1 & j\sin\theta_1/Y_1 \\ jY_1\sin\theta_1 & \cos\theta_1 \end{bmatrix} \cdot \begin{bmatrix} 1 & 0 \\ B_2 & 1 \end{bmatrix} \\ &= \begin{bmatrix} \cos\theta_1 + jB_2\sin\theta_1/Y_1 & j\sin\theta_1/Y_1 \\ (B_1+B_2)\cos\theta_1 + j(B_1B_2+Y_1^2)\sin\theta_1/Y_1 & \cos\theta_1 + jB_1\sin\theta_1/Y_1 \end{bmatrix} \end{aligned} \tag{4.3}$$

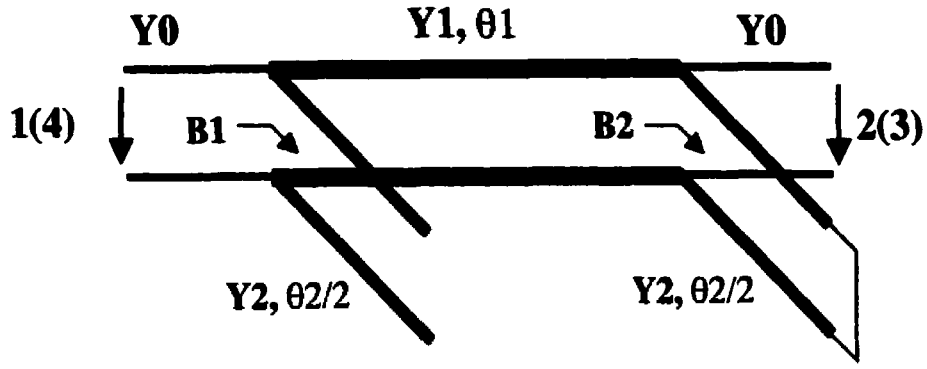

(a)

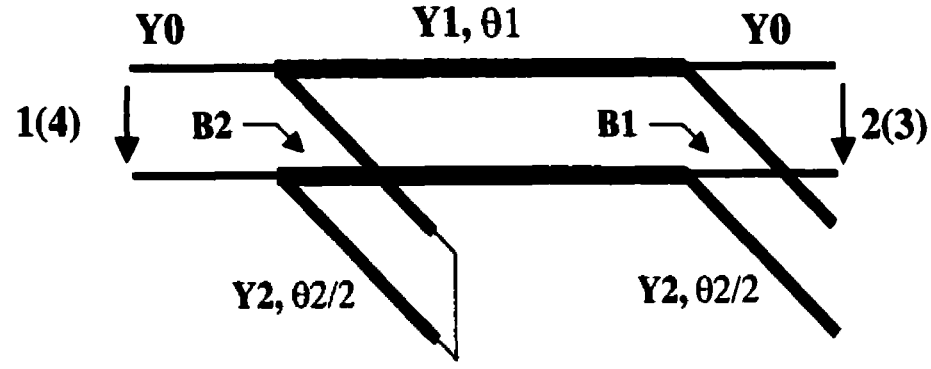

(b)

Figure 4.2 Equivalent circuits for even/odd mode excitation. (a) Even-mode and (b) odd-mode.

In Figure 4.2, it is obvious that the equivalent circuit under the odd-mode excitation is the same as the one under the even-mode excitation with exchanging the input and output ports. Therefore, we have

$$\begin{aligned} a_o &= d_e \\ b_o &= b_e \\ c_o &= c_e \\ d_o &= a_e \end{aligned} \tag{4.4}$$

in which the subscript o stands for the odd-mode excitation.

It is known that for a reciprocal two-port network the relationship between the S-parameter and normalized ABCD matrix can be expressed as

$$\begin{bmatrix} S_{11} & S_{12} \\ S_{21} & S_{22} \end{bmatrix} = \frac{1}{A+B+C+D} \begin{bmatrix} A-D+B-C & 2 \\ 2 & D-A+B-C \end{bmatrix} \tag{4.5}$$

where

$$\begin{bmatrix} A & B \\ C & D \end{bmatrix} = \begin{bmatrix} a & bY_0 \\ c/Y_0 & d \end{bmatrix} \tag{4.6}$$

With the above analysis, we can obtain the S-parameters of the ring coupler as below.

$$
\begin{aligned}
S_{11} &= S_{22} = -\frac{\cos\theta_1 \cdot Z_0 \cdot (B_1 + B_2) + K_p}{N_p} \\
S_{12} &= \frac{2}{N_p} \\
S_{13} &= 0 \\
S_{14} &= -S_{23} = \frac{j \cdot Z_1 \cdot \sin\theta_1 \cdot (B_2 - B_1)}{N_p}
\end{aligned}
\tag{4.7}
$$

where

$$
\begin{aligned}
K_p &= j \cdot Z_0 \cdot Y_1 \cdot \sin\theta_1 \cdot (1 + B_1 \cdot B_2 \cdot Z_1^2 - Y_0^2 \cdot Z_1^2) \\
N_p &= 2 \cdot \cos\theta_1 + (j \cdot Z_1 \cdot \sin\theta_1 + \cos\theta_1 \cdot Z_0) \cdot (B_1 + B_2) + H_p \\
H_p &= j \cdot Z_0 \cdot Y_1 \cdot \sin\theta_1 \cdot (1 + B_1 \cdot B_2 \cdot Z_1^2 + Y_0^2 \cdot Z_1^2) \\
Z_0 &= 1/Y_0 \\
Z_1 &= 1/Y_1
\end{aligned}
\tag{4.8}
$$

The perfect match condition of the input/output ports requires that S_{11} and S_{22} be zero. This leads to the following equation

$$
2 \cdot Y_2 \cdot \cot\theta_1 \cdot \cot\theta_2 = Y_1 \cdot (1 + Y_2^2 \cdot Z_1^2 - Y_0^2 \cdot Z_1^2) \tag{4.9}
$$

From (4.7), the amplitude imbalance between two output ports can be written as

$$
\left|\frac{S_{12}}{S_{14}}\right| = \left|\frac{S_{12}}{S_{23}}\right| = \left|\frac{Y_1 \cdot \sin\theta_2}{Y_2 \cdot \sin\theta_1}\right| \tag{4.10}
$$

As discussed in the previous chapter, (3.11) must be upheld for a lossless, passive and linear four-port network.

With (3.11) and (4.10), we can obtain a pair of equations

$$|S_{12}|^2 = \frac{(1-|S_{11}|^2)\cdot|Y_1\cdot\sin\theta_2|^2}{|Y_2\cdot\sin\theta_1|^2+|Y_1\cdot\sin\theta_2|^2}$$
$$|S_{14}|^2 = \frac{(1-|S_{11}|^2)\cdot|Y_2\cdot\sin\theta_1|^2}{|Y_2\cdot\sin\theta_1|^2+|Y_1\cdot\sin\theta_2|^2} \tag{4.11}$$

Clearly, the above theory is general, and may apply to the analysis and design of a parallel-type ring coupler with ideal phase inverter and any arbitrary power ratio.

From the above equations, it is seen that principal features and electrical characteristics of a series-type ring coupler, which was discussed in the previous chapter, are also applied to the parallel-type ring coupler. The power-split ratio between the two output ports is proportional to the square of the term $\left|\frac{Y_1\cdot\sin\theta_2}{Y_2\cdot\sin\theta_1}\right|$. If $\theta_1=\theta_2$, such a power split ratio is obviously proportional to the square of the ratio of the two admittance variables of the ring and it is independent of frequency.

4.3 Design criteria for 3-dB ring coupler with phase inverter

In the design of a 3-dB coupler, the two output ports are required to be equal. With (4.10), we have

$$Y_1 = Y_2\cdot\frac{\sin\theta_1}{\sin\theta_2} \tag{4.12}$$

Note that the absolute sign in (4.12) is eliminated to consider that $\theta_1,\theta_2<180°$. This is a typical case in coupler design.

With (4.12) and (4.9), the design equations for a parallel-type 3 dB ring coupler with phase inverter can be obtained as

$$Z_1 = Z_0 \cdot \frac{\sqrt{2-(\cos\theta_1+\cos\theta_2)^2}}{\sin\theta_1}$$
$$Z_2 = Z_0 \cdot \frac{\sqrt{2-(\cos\theta_1+\cos\theta_2)^2}}{\sin\theta_2} \tag{4.13}$$

in which $Z_2 = 1/Y_2$. Since the characteristic impedances Z_1, Z_2 of transmission lines on ring have to be larger than zero, the constraint for θ_1 and θ_2 in (3.15) also holds for the parallel-type ring coupler. With the similar argument given in the design of the series-type ring coupler, we may classify the design for the parallel-type ring coupler into two categories: broadband and narrow-band. In the following, we just give a brief summary for the two designs since the detailed discussion was presented in the Chapter III.

In the broadband design, the two output ports can perfectly be balanced with the following condition.

$$\theta_1 = \theta_2 = \theta$$
$$Y_1 = Y_2 = Y \tag{4.14}$$

In light of (4.9), and (4.14), the following relationship can be obtained

$$|S_{12}|^2 = |S_{14}|^2 = \frac{1}{2}\cdot\left(1-|S_{11}|^2\right)$$
$$Z = Z_0 \cdot \sqrt{2(1-\cot^2\theta)} \tag{4.15}$$

where $Z = 1/Y$

For a given return loss requirement, the design equations for the parallel-type 3-dB ring coupler can be written as

$$Z = Z_0 \cdot \sqrt{2\left(1 - \frac{2}{1+10^{-\frac{L}{20}}}\right)} \qquad (4.16)$$

$\theta = 90^0$ (at the center frequency)

in which L is the in-band maximum return loss specification. Clearly, the characteristic impedance Z must meet the following condition.

$$Z \le Z_0 \cdot \sqrt{2} \qquad (4.17)$$

For narrow-band application, the design equations of the parallel-type ring coupler can be written as

$$Z_1 = Z_0 \cdot \frac{\sqrt{2-(\cos\theta_1 + \cos\theta_2)^2}}{\sin\theta_1}$$

$$Z_2 = Z_0 \cdot \frac{\sqrt{2-(\cos\theta_1 + \cos\theta_2)^2}}{\sin\theta_2} \qquad (4.18)$$

Minimize $(\theta_1 + \theta_2)$ under certain fabrication requirements

4.4 Numerical and experimental results for a micro-coplanar stripline ring coupler

The analysis and design criteria for the parallel-type ring coupler with phase inverter have been presented in the above sections. Now, we introduce a 3-dB micro-coplanar stripline ring coupler, which is developed based on the above proposed design theory. In

the following, we first give a brief description of the ring coupler circuit. Then, numerical results for the coupler are calculated using the full-wave analysis based on a finite element technique. The coupler was fabricated and tested. Experimental results are also presented and discussed in detail.

4.4.1 Description of a micro-coplanar stripline ring coupler circuit

Figure 4.3 illustrates the physical configuration of a 3-dB micro-coplanar stripline ring coupler with phase inverter. The ring coupler consists of four CPW to micro-coplanar stripline T-junctions and four quarter-wavelength micro-coplanar stripline sections. One of the four micro-coplanar stripline sections contains a phase inverter, which is realized by the combination of two-strip crossover and slotline radial stub. As discussed in the chapter II, the combination of slotline radial stub and two-strip crossover produces additional 180° phase shift for a broadband. The uniplanar ring coupler was built on a RT/Duriod 6010 ($\varepsilon_r = 10.2$) substrate with thickness $h = 1.27$ mm. The characteristic impedance for feed lines was chosen as 50 Ω with the following dimensions: the center conductor width $W = 0.60$ mm and the gap size between the center conductor and ground $S = 0.26$ mm. Using (4.16) for the design requirement of –20 dB return loss, we can obtain the characteristic impedance for the quarter-wavelength section as 64.2 Ω, which corresponds to the strip width $W = 1.15$ mm and the gap size between the strip and ground $S = 0.25$ mm. The micro-coplanar stripline ring has the mean radius $r = 10$ mm. The gap dimension for the two-strip crossover is $G = 0.40$ mm. Dimensions of the slotline radial stub are the radius $r = 7$ mm and angle $\alpha = 90°$.

4.4.2 Numerical Results

The performance of the ring coupler described above was calculated using the commercial software HFSS developed by Ansoft. Figure 4.4 shows the geometry of the coupler used in the performance calculation. A virtual box was introduced to define the

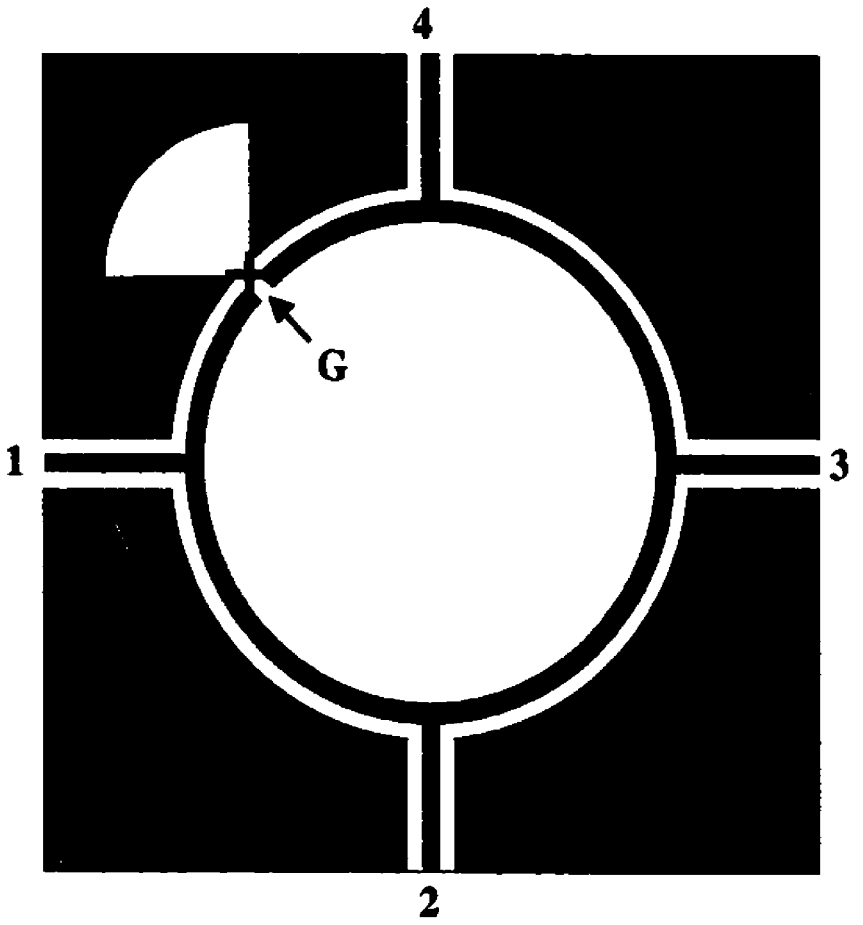

Figure 4.3 Physical configuration of a micro-coplanar stripline ring coupler with phase inverter.

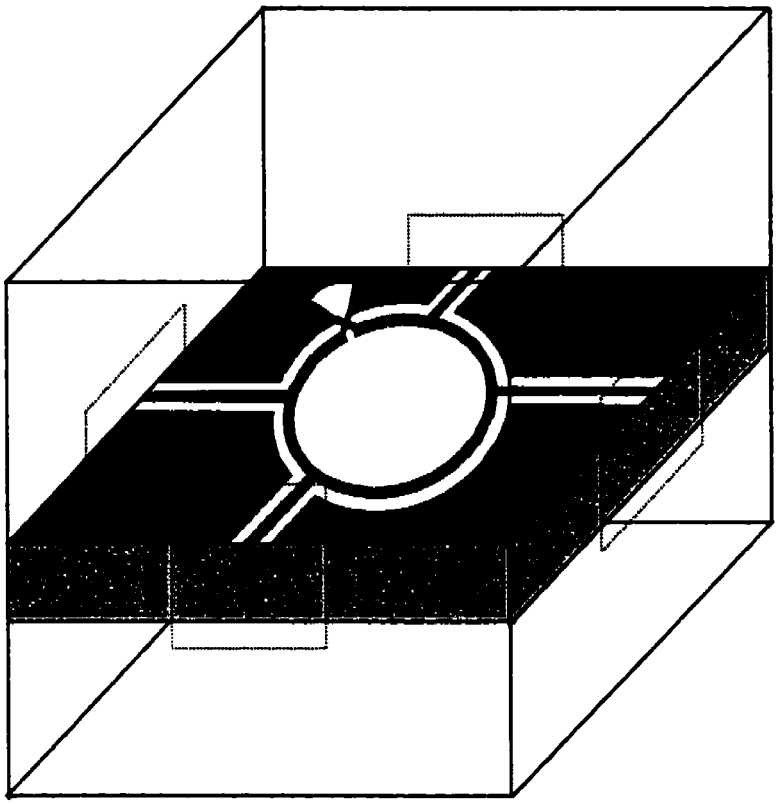

Figure 4.4 Geometry of the micro-coplanar stripline ring coupler for finite element analysis

field solution area. Radiation boundaries were assigned to the surfaces of the virtual box in analysis in order to consider the bounded effect of the circuit. To minimize computational resources, the virtual box was chosen to have the dimension of $30\times30\times30$ mm^3. The dimensions for all of the feeding ports are 8×8 mm^2. The crossover for 180° phase shift was modeled by an airbridge with a square cross-section (0.2×0.2 mm^2). Calculated frequency responses for return loss, coupling, isolation and phase difference are shown in Figure 4.5.

Figure 4.5(a) shows that the return loss for $|S_{11}|$ and $|S_{44}|$ is better than -15 dB from 1.3 GHz to 2.5 GHz. For the same requirement, the effective bandwidth for $|S_{22}|$ and $|S_{33}|$ is about 1.6 GHz from 1.0 - 2.6 GHz. The two matching points are clearly observed in the figure, which validates the developed design theory. The bandwidth reduction for $|S_{11}|$ and $|S_{44}|$ is essentially caused by the imperfection of the phase inverter as discussed in the chapter II. In Figure 4.5(b), it is seen that the power dividing $|S_{21}|$, $|S_{23}|$, and $|S_{43}|$ is within -3.5 ± 0.5 dB from 0.9 - 2.5 GHz. With the same coupling requirement, the bandwidth of $|S_{41}|$ is 0.8 GHz from 1.5 - 2.3 GHz. The bandwidth reduction for $|S_{41}|$ may be caused by the imperfection of the slotline radial stub, which provides open-circuit only at the center frequency. The mutual isolation for ports 1(2) and 3(4) is shown in Figure 4.5(c). It is seen that the isolation is better than -20 dB from 1.2 - 3.0 GHz. Figure 4.5(d) shows the phase difference for the in-phase and 180° out of phase mode coupling. The phase error is less than $\pm5°$ in the frequency range of 1.5 - 2.4 GHz. Clearly, the calculated results show that the proposed ring coupler has a fairly good performance.

4.4.3 Experiment results

Measured performance of the proposed ring coupler is shown in Figure 4.6. The measurement was made using GGB probes (40A-GSG-1250) and a vector network

analyzer (HP 8720ES). A TRL calibration was used to remove the systematic errors of the test station. For each measurement, a two-port S-parameter was obtained under the condition of terminating the other two ports of the ring coupler. The termination for each port was implemented by soldering two $100\,\Omega$ chip resistors to the CPW feed line in parallel. Figure 4.6(a) shows the measured frequency response of return loss for all ports of the ring coupler. It is seen that the return loss is better than $-18\,\text{dB}$ in the frequency range of $1.6-2.6\,\text{GHz}$, which generally agrees with the calculated results. Measured frequency response of coupling for output ports is shown in Figure 4.6(b). The coupling for all the ports is within -3.5 ± 0.6 dB from $1.6-3.0\,\text{GHz}$. It is obvious that the coupling performance is limited by $|S_{41}|$, which agrees with the calculated results shown in Figure 4.5(b). Figure 4.6(c) shows measured mutual isolation between the ports 1(2) and 3(4)). It is seen that the mutual isolation is better than -20 dB in the frequency range of $1.0-3.5\,\text{GHz}$. Measured phase difference for the in-phase and 180° out of phase mode coupling is shown in Figure 4.6(d). The phase error is less than $\pm5°$ in the frequency range of $1.6-2.5\,\text{GHz}$, which agrees well with the calculated one. It should be noted that the above measured results include the effect of the imperfection of termination resistors.

4.5 Conclusion

In this chapter, the analysis of parallel-type uniplanar ring coupler with phase inverter has been presented. Principal features and design consideration for the ring coupler are reviewed. A micro-coplanar stripline ring coupler was developed. The electrical performance of the ring coupler was calculated using a full-wave analysis. The experimental results agree well with the numerical ones.

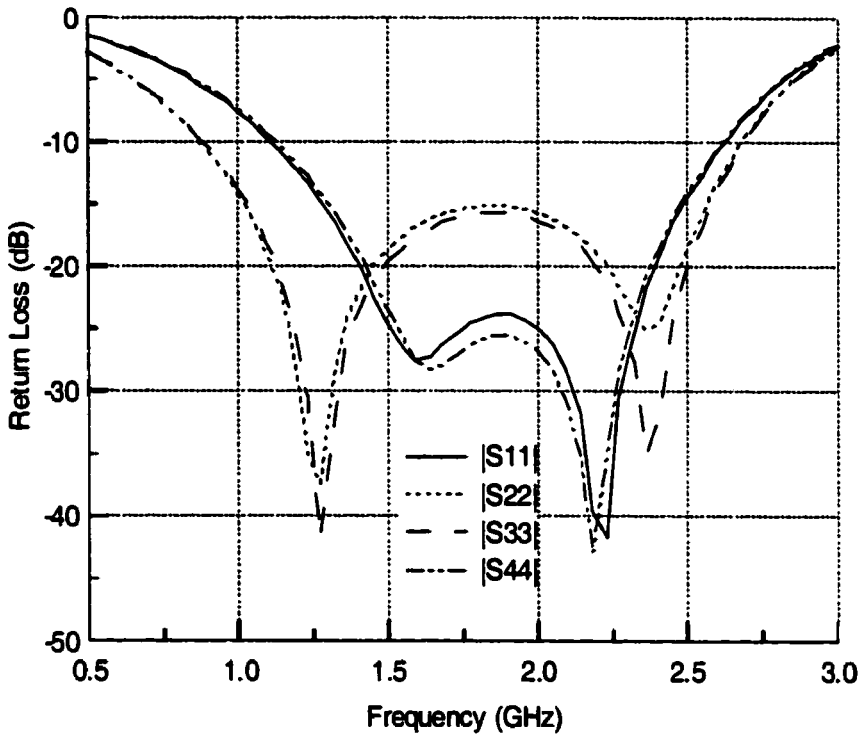

Figure 4.5(a) Calculated frequency responses of return loss for the four input ports of the ring coupler shown in Figure 4.4

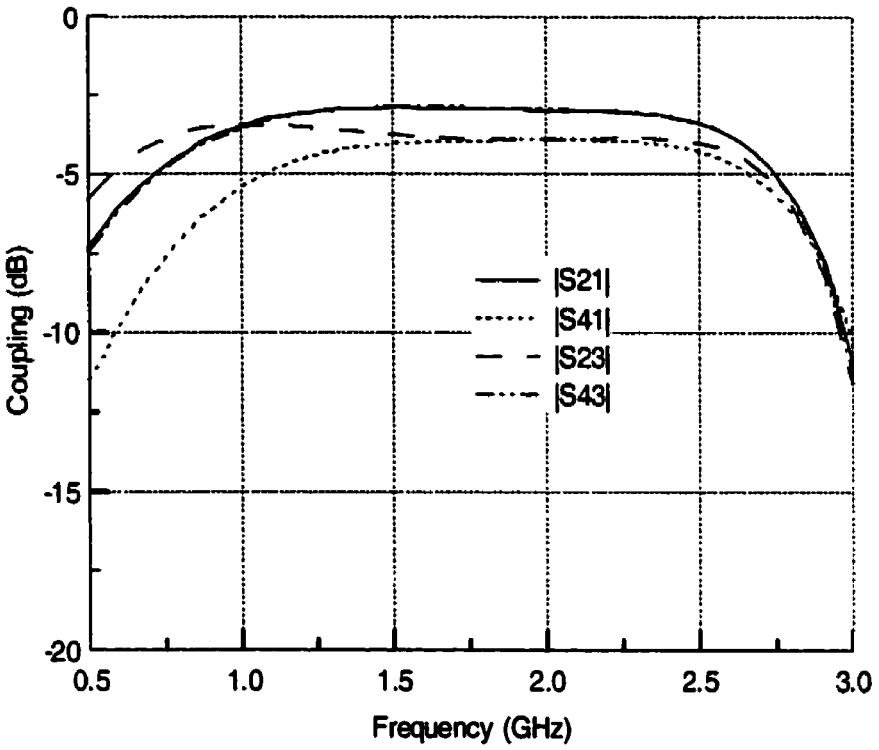

Figure 4.5(b) Calculated frequency responses of coupling for the ring coupler shown in Figure 4.4

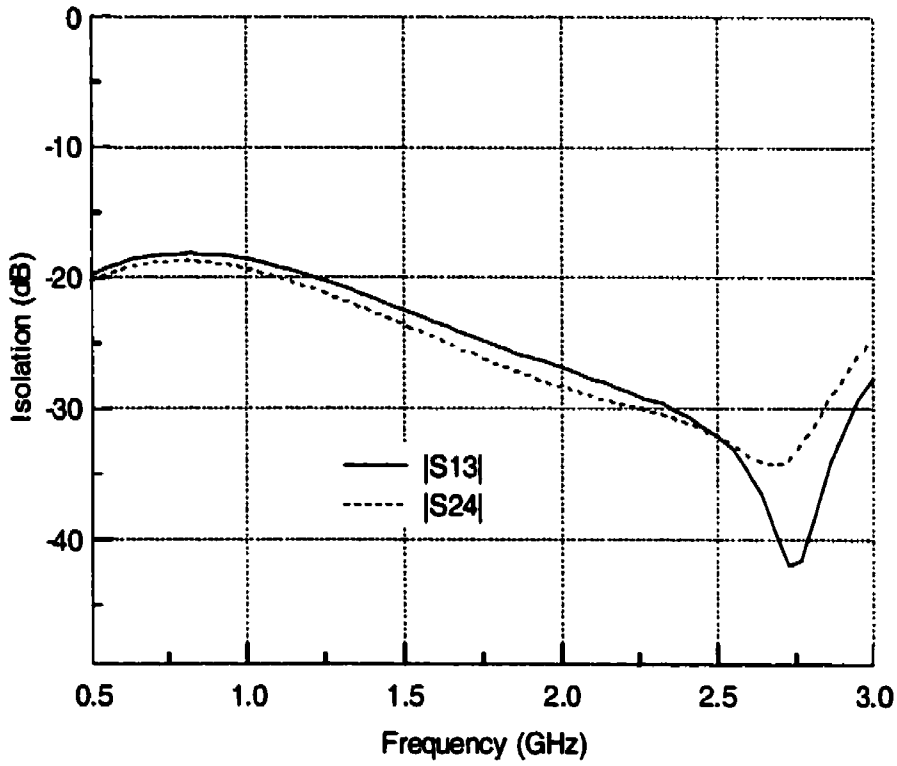

Figure 4.5(c) Calculated frequency responses of the mutual isolation for the ring coupler shown in Figure 4.4

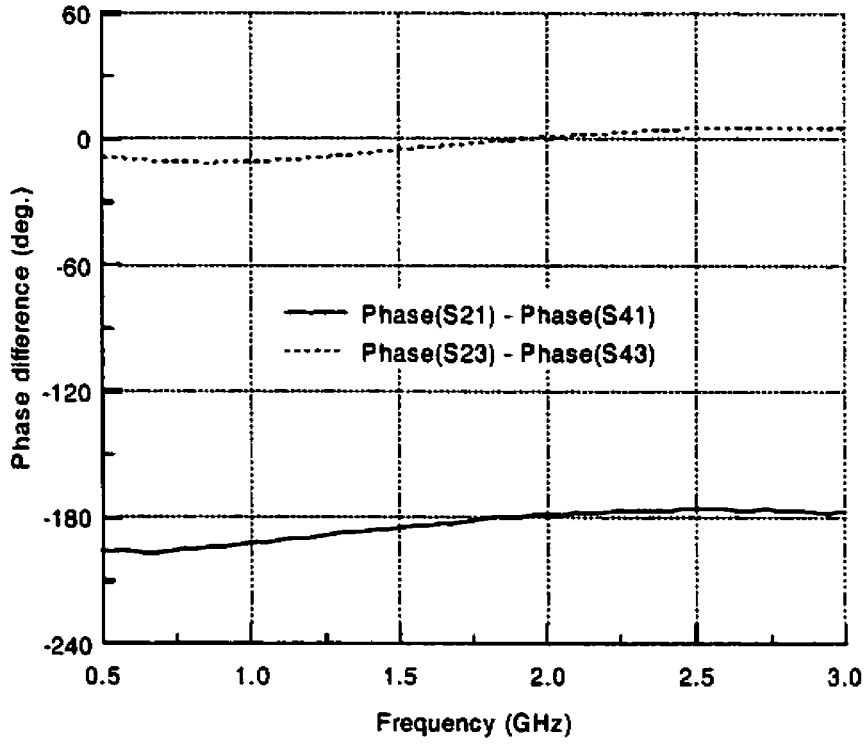

Figure 4.5(d) Calculated phase difference between output ports 2 and 4 for the ring coupler shown in Figure 4.4

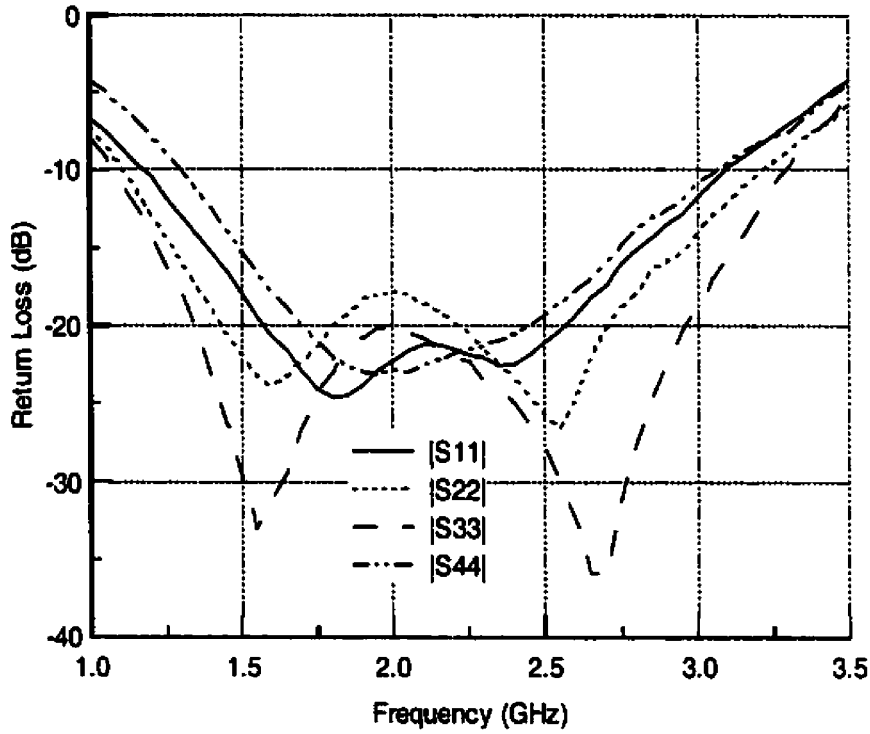

Figure 4.6(a) Measured frequency responses of return loss for the four input ports of the ring coupler shown in Figure 4.3

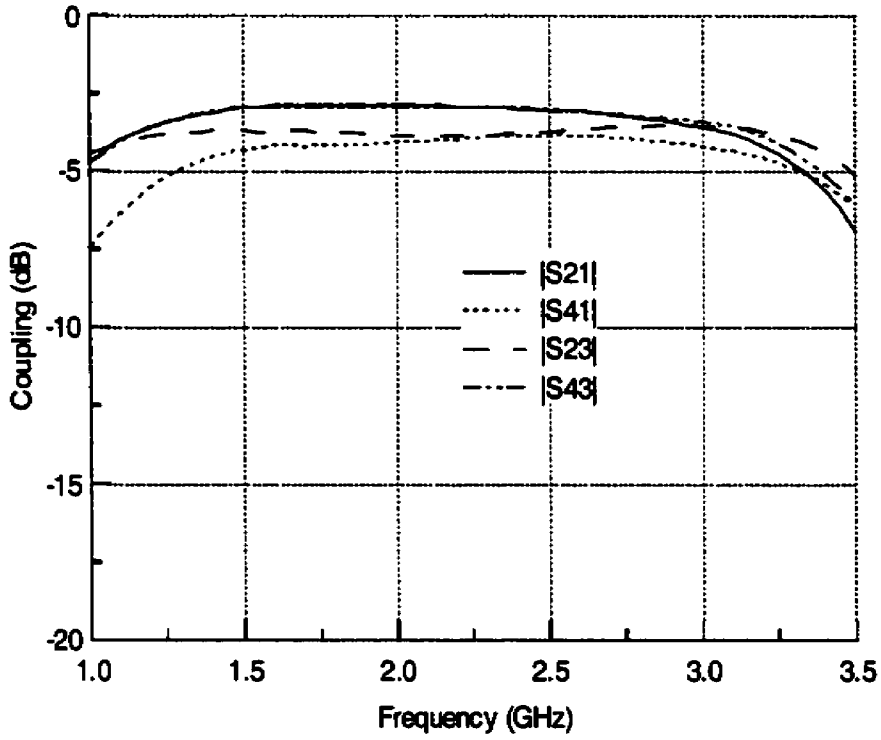

Figure 4.6(b) Measured frequency responses of coupling for the ring coupler shown in Figure 4.3

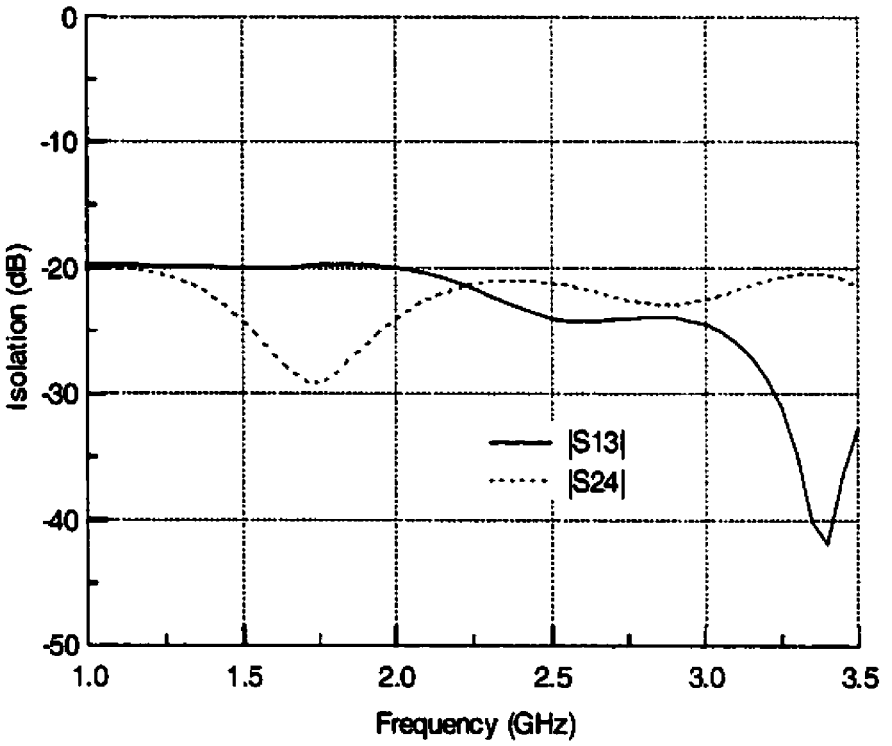

Figure 4.6(c) Measured frequency responses of the mutual isolation for the ring coupler shown in Figure 4.3

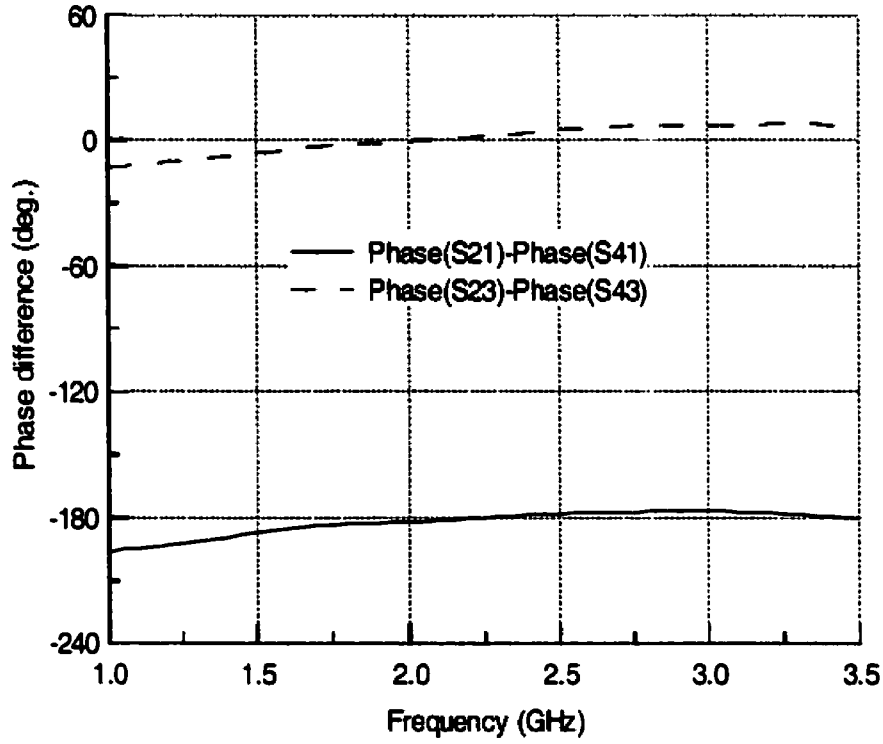

Figure 4.6(d) Measured phase difference between output ports 2 and 4 for the ring coupler shown in Figure 4.3

Chapter V

Analysis and Design of Uniplanar Magic-T Circuits

5.1 Introduction

This chapter presents the analysis and design of novel uniplanar magic-T circuits. Magic-T's are fundamental components in many microwave circuits such as power combiners and dividers, balanced mixer, and frequency discriminators. The matched waveguide double-T is a well-known and widely used waveguide magic-T. Figure 5.1 shows the physical configuration of the waveguide magic-T. The magic-T is composed of E- and H-junctions. The reference planes for ports 1 and 2 are chosen to be symmetrical with respect to the plane P-P as shown in Figure 5.1. It is obvious that, when a TE_{10} mode is incident at port H, the resulting E_y field has even distribution with respect to the plane P-P at the junction as shown in Figure 5.2(a). This means there is no coupling between ports E and H. The incident wave will divide into two components at the junctions. The components arrive in-phase at ports 1 and 2. Similarly, when a TE_{10} mode is incident at port E, the resulting E_y field has odd distribution with respect to the plane P-P at the junction as shown in Figure 5.2(b). Again there is no coupling between ports E and H. The incident wave will divide into two components at the junctions, both of which arrive at port 1 and 2 with 180° phase difference. The properties of the waveguide magic-T discussed here are also applied to the uniplanar magic-T presented below.

In this chapter, we first describe two basic configurations of uniplanar magic-T circuits. Then the characteristics of uniplanar magic-T circuits are discussed. Using the power conservation, we derive the matching condition of the uniplanar magic-T. A conceptual

lumped circuit model of the matched magic-T is also given in the second section. The third section presents the theoretical analysis of uniplanar magic-T circuits. A set of design equations are obtained. The design criteria of uniplanar magic-T circuits are discussed. To verify the developed design theory, a compact uniplanar magic-T circuit is introduced in the forth section. The circuit performance is calculated using finite element analysis. The theoretical and experimental results are presented and discussed in detail.

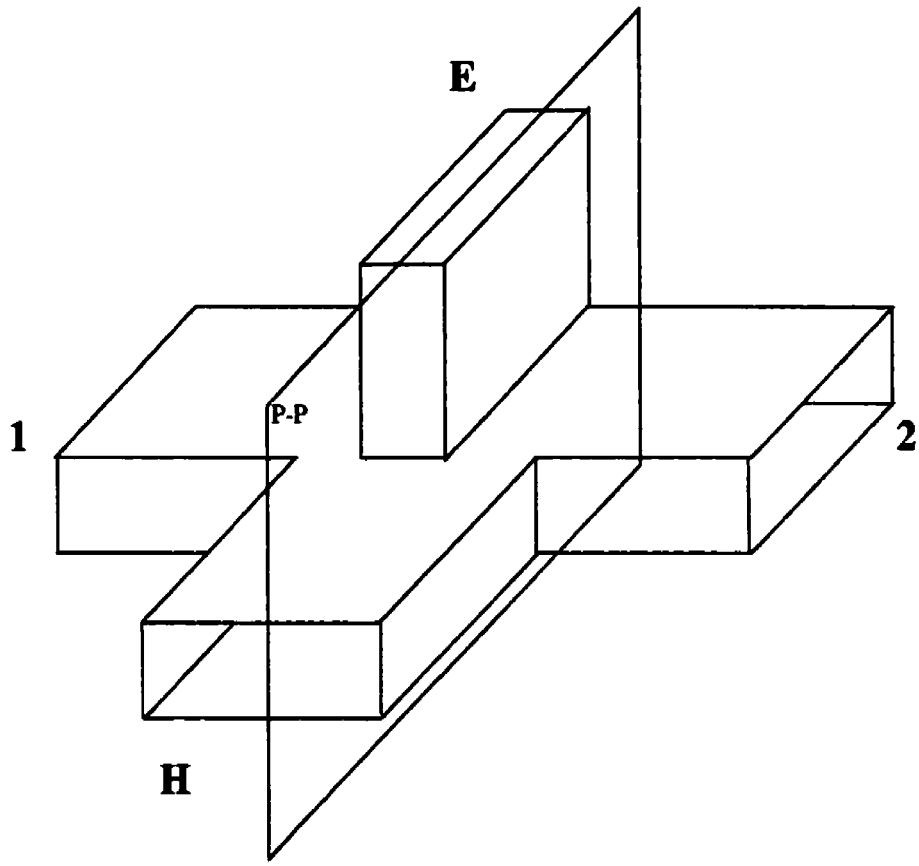

Figure 5.1 Physical configuration of the waveguide magic-T

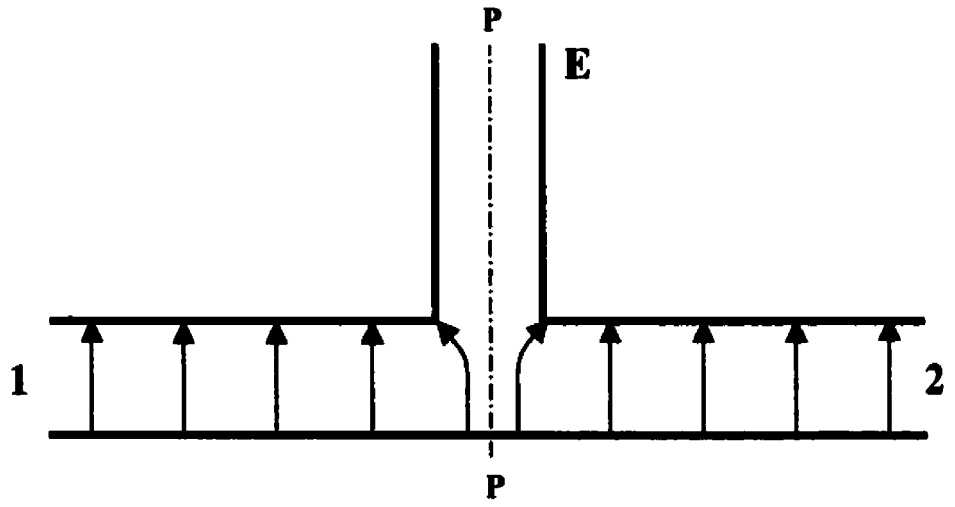

(a)

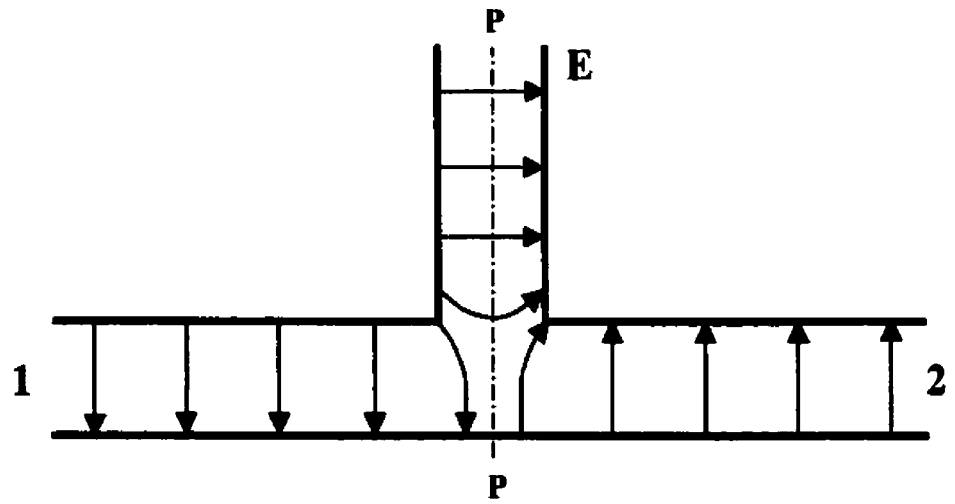

(b)

Figure 5.2 Schematic diagram of the E-field distribution of (a) the excitation at H-port and (b) the excitation at E-port

5.2 Basic properties of uniplanar magic-T circuits

As mentioned before, one of advantages of uniplanar circuits is easy to realize series and parallel connections. Figure 5.3 shows uniplanar series and parallel T-junctions. The waveguide magic-T consists of two T-junctions. It is well known that the E-junction in the waveguide magic-T is equivalent to series T-connection while the H-junction equivalent to parallel T-connection. Similarly, uniplanar magic-T's presented here are also composed of series and parallel T-junctions. In terms of T-junction, uniplanar magic-T circuits can be divided into two basic types: series and parallel. Figure 5.4 shows the schematic diagrams of two basic types of uniplanar magic-T's. The reference planes for ports 1 and 2 are chosen to be symmetrical with respect to the plane P-P. The reference direction of voltage at the ports 1 and 2 is shown in the figure by the lines with an arrow at one end. In Figure 5.4(a), the series-type uniplanar magic-T consists of three series and one parallel T-junctions. The parallel-type magic-T is composed of three parallel and one series T-junctions as shown in Figure 5.4(b).

Generally speaking, a magic-T is a four-port network. Its electrical characteristics can be described by a 4X4 S-parameter matrix as given below.

$$S = \begin{bmatrix} S_{11} & S_{1H} & S_{12} & S_{1E} \\ S_{H1} & S_{HH} & S_{H2} & S_{HE} \\ S_{21} & S_{2H} & S_{22} & S_{2E} \\ S_{E1} & S_{EH} & S_{E2} & S_{EE} \end{bmatrix} \tag{5.1}$$

In terms of the discussion in the previous section, it is known that there is no coupling between ports H and E due to the even and odd field distributions at the junction. Obviously, the property also holds for uniplanar magic-T circuits. Since the ports 1 and 2 of the uniplanar magic-T are symmetrical with respect to the plane P-P, we have

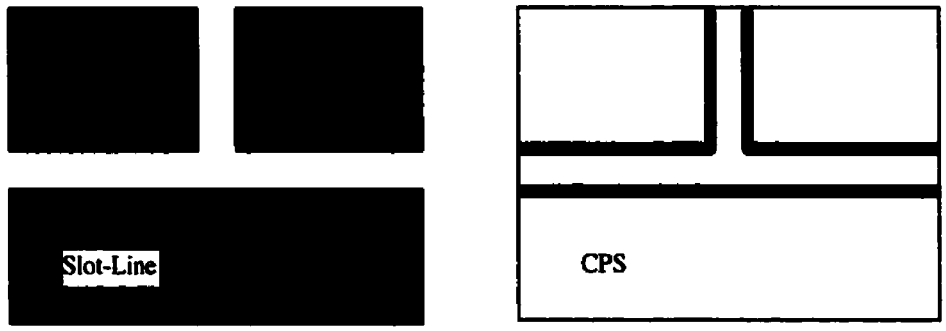

(a)

(b)

Figure 5.3 Physical layouts of uniplanar T-junctions (a) series-type and (b) parallel-type

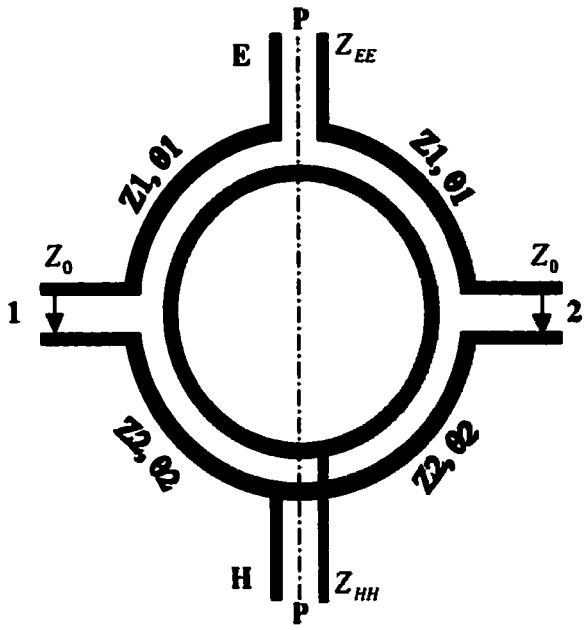

(a)

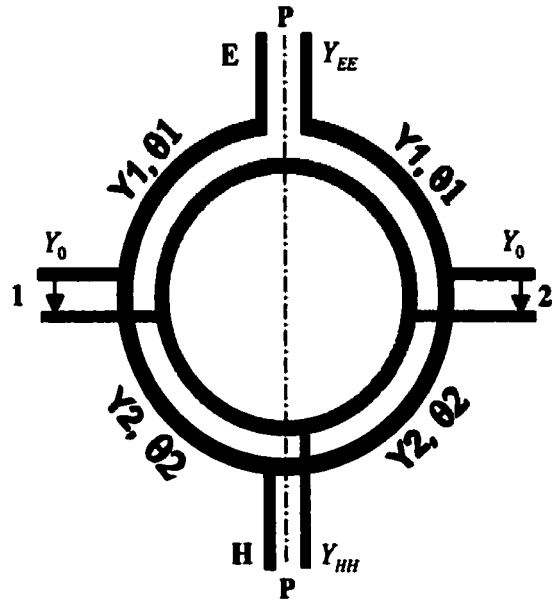

(b)

Figure 5.4 Schematic diagrams of uniplanar magic-T's (a) series-type and (b) parallel-type

$$
\begin{aligned}
S_{EH} &= S_{HE} = 0 \\
S_{11} &= S_{22} \\
S_{1H} &= S_{2H} \\
S_{1E} &= -S_{2E}
\end{aligned}
\tag{5.2}
$$

With (5.2), we can rewrite (5.1) as

$$
S = \begin{bmatrix}
S_{11} & S_{1H} & S_{12} & S_{1E} \\
S_{1H} & S_{HH} & S_{1H} & 0 \\
S_{12} & S_{1H} & S_{11} & -S_{1E} \\
S_{1E} & 0 & -S_{1E} & S_{EE}
\end{bmatrix}
\tag{5.3}
$$

For a reciprocal and lossless passive network, we have

$$
S \cdot S_t^* = I \tag{5.4}
$$

Where S_t^* stands for the transpose and complex conjugate matrix of S and I is a unit matrix.

Substituting (5.3) into (5.4), we obtain

$$
\begin{aligned}
|S_{1H}|^2 &= \frac{1-|S_{HH}|^2}{2} \\
|S_{1E}|^2 &= \frac{1-|S_{EE}|^2}{2} \\
S_{11} &= -\frac{1}{2}\cdot\left[\frac{S_{1H}}{S_{1H}^*}\cdot S_{HH}^* + \frac{S_{1E}}{S_{1E}^*}\cdot S_{EE}^*\right] \\
S_{12} &= -\frac{1}{2}\cdot\left[\frac{S_{1H}}{S_{1H}^*}\cdot S_{HH}^* - \frac{S_{1E}}{S_{1E}^*}\cdot S_{EE}^*\right]
\end{aligned}
\tag{5.5}
$$

From (5.5), it is seen that S_{11} and S_{12} are the linear combination of S_{HH}^{*} and S_{EE}^{*}, respectively. Clearly, the moduli of $\frac{S_{1H}}{S_{1H}^{*}}$ and $\frac{S_{1E}}{S_{1E}^{*}}$ are equal to one. Using the triangle inequality in complex algebra, we have

$$\begin{aligned} |S_{11}| &\le \frac{|S_{EE}|+|S_{HH}|}{2} \le Max(|S_{EE}|,|S_{HH}|) \\ |S_{12}| &\le \frac{|S_{EE}|+|S_{HH}|}{2} \le Max(|S_{EE}|,|S_{HH}|) \end{aligned} \tag{5.6}$$

The inequalities of (5.6) indicates that with the same design criteria for the return loss and isolation the bandwidth of magic-T is not limited by $|S_{11}|$ and $|S_{12}|$.

Further, if

$$|S_{HH}| = |S_{EE}| = 0 \tag{5.7}$$

We obtain

$$\begin{aligned} |S_{1H}| &= \frac{1}{\sqrt{2}} \\ |S_{1E}| &= \frac{1}{\sqrt{2}} \\ S_{11} &= 0 \\ S_{12} &= 0 \end{aligned} \tag{5.8}$$

From (5.8), we can conclude that if the ports E and H are matched the uniplanar magic-T becomes an ideal 3-dB coupler, that is, all ports are matched and the ports between E (1) and H (2) are isolated.

In the terms of above analysis, it is seen that the uniplanar magic-T design is attributed to input impedance matching design at the ports E and H, respectively. Generally, impedance matching can be achieved by an impedance transformer. Figure 5.5 shows a conceptual lumped circuit model of magic-T, in which the impedance matching is realized by two transformers. In the following section, we will derive a general design formula for matched uniplanar magic-T. It will be found that there are two sets of solutions for the matched uniplanar magic-T. One of the solutions is corresponding to the impedance transformer design.

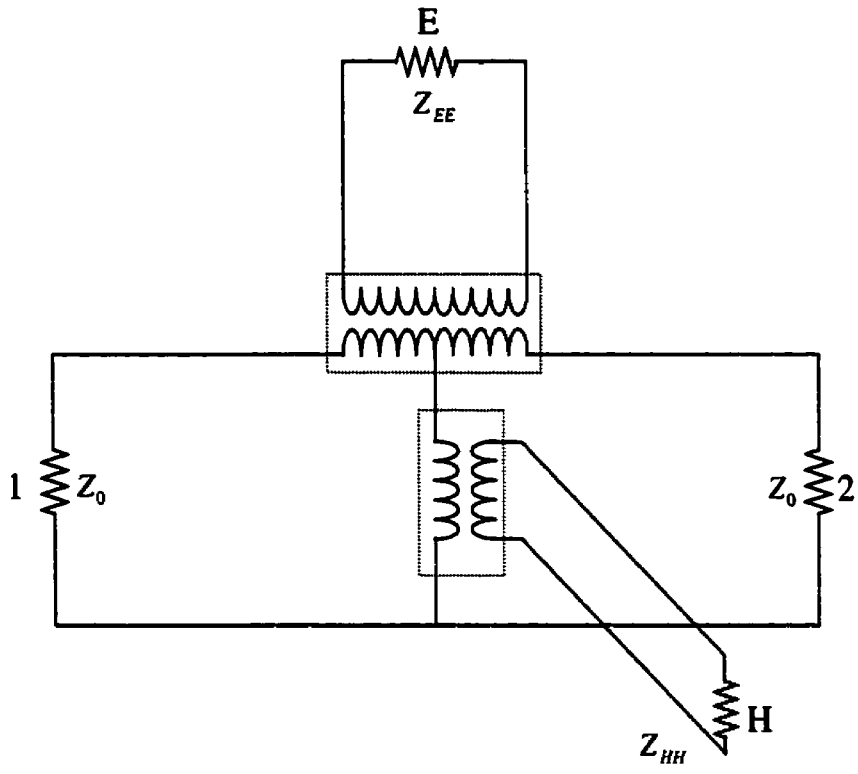

Figure 5.5 A conceptual lumped circuit model of magic-T

5.3 Theoretical analysis of uniplanar magic-T's

It is known that the uniplanar magic-T design can be simplified to the input impedance matching design at ports E and H. The reflection coefficients at ports E and H can be obtained from the circuit analysis. As discussed before, uniplanar magic-T 's can be classified as two types. In the following, we present the analysis of two types of uniplanar magic-T's, respectively.

5.3.1 Series-type uniplanar magic-T

The series-type uniplanar magic-T is shown in Figure 5.4(a). The characteristic impedance for ports E and H is described by Z_{EE} and Z_{HH}, respectively. The symbol Z_0 stands for the characteristic impedance of ports 1 and 2. The electrical length and characteristic impedance for transmission lines connected to the E-junction are denoted by θ_1 and Z_1, respectively. The θ_2 and Z_2 stands for the electrical length and characteristic impedance of the transmission lines connected to H-junction. Since there is no coupling between ports E and H, the uniplanar magic-T can be decomposed to a simple one-port network under E- and H-port excitation as shown in Figure 5.6. It should be noted that with the excitation at H-port the series-junction connecting to port E is equivalent to open-circuit due to the even distribution of the voltage with respect to the plane P-P. Similarly, with the excitation at E-port the parallel-junction connecting to port H is equivalent to short-circuit due to the odd distribution of the voltage with respect to the plane P-P.

In Figure 5.6, the input reflection coefficients S_{EE} and S_{HH} can be written as

$$S_{EE} = \frac{Z_{inE} - Z_{EE}}{Z_{inE} + Z_{EE}}$$
$$S_{HH} = \frac{Z_{inH} - Z_{HH}}{Z_{inH} + Z_{HH}} \tag{5.9}$$

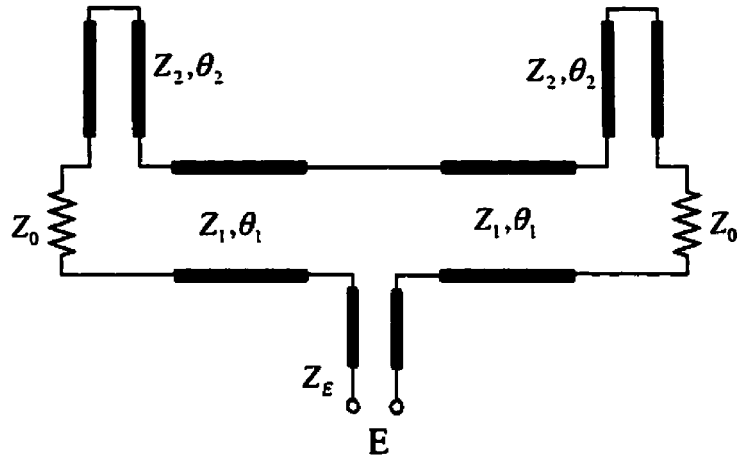

(a)

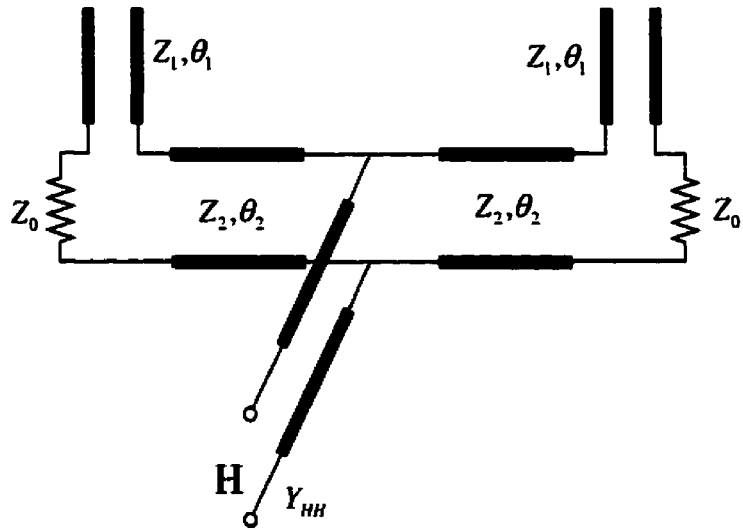

(b)

Figure 5.6 Equivalent circuits of series-type uniplanar magic-T with the excitation (a) at port E and (b) at port H.

In which Z_{inE} and Z_{inH} are the input impedance considering the excitation at ports E and H, respectively. With a straightforward circuit analysis, we can express S_{EE} and S_{HH} in terms of the circuit parameters as below.

$$S_{EE} = \frac{Z_1 Z_0 - Z_E(Z_1 - Z_2 \tan\theta_1 \tan\theta_2) + j[(Z_1^2 - Z_E Z_0)\tan\theta_1 + Z_1 Z_2 \tan\theta_2]}{Z_1 Z_0 + Z_E(Z_1 - Z_2 \tan\theta_1 \tan\theta_2) + j[(Z_1^2 + Z_E Z_0)\tan\theta_1 + Z_1 Z_2 \tan\theta_2]}$$

$$S_{HH} = \frac{Z_2 Z_0 - Z_H(Z_2 + Z_1 \cot\theta_1 \tan\theta_2) - j[Z_1 Z_2 \cot\theta_1 - (Z_2^2 - Z_0 Z_H)\tan\theta_2]}{Z_2 Z_0 + Z_H(Z_2 + Z_1 \cot\theta_1 \tan\theta_2) - j[Z_1 \cot\theta_1 - (Z_2^2 + Z_0 Z_H)\tan\theta_2]} \quad (5.10)$$

Where $Z_E = Z_{EE}/2$ and $Z_H = 2Z_{HH}$

As discussed above, the condition for a matched magic-T can be simply written as

$$\begin{aligned} S_{EE} &= 0 \\ S_{HH} &= 0 \end{aligned} \quad (5.11)$$

Substituting (5.10) into (5.11), the following relationship can be obtained.

$$\begin{aligned} &Z_1 Z_2 \cot\theta_1 - (Z_2^2 - Z_0 Z_H)\tan\theta_2 = 0 \\ &Z_1(Z_0 - Z_E)\cot\theta_1 + Z_E Z_2 \tan\theta_2 = 0 \\ &Z_2(Z_0 - Z_H) - Z_H Z_1 \cot\theta_1 \tan\theta_2 = 0 \\ &(Z_1^2 - Z_E Z_0) + Z_1 Z_2 \cot\theta_1 \tan\theta_2 = 0 \end{aligned} \quad (5.12)$$

In (5.12), the first two equations are a set of linear homogeneous algebraic equations with respect to $\cot\theta_1$ and $\tan\theta_2$. It is known that the solutions for a set of linear homogeneous algebraic equations can be divided into two cases: trivial and nontrivial ones. In the following, we discuss the solutions of (5.12) for the two cases, respectively.

Case 1: *Trivial solution for* $\cot\theta_1$ *and* $\tan\theta_2$

Obviously, the determinant of the coefficients for the first two equations in (5.12) can be written as

$$D_s = \begin{vmatrix} Z_1 Z_2 & -(Z_2^2 - Z_0 Z_H) \\ Z_1(Z_0 - Z_E) & Z_E Z_2 \end{vmatrix} \tag{5.13}$$

For the trivial solution, we have

$$\begin{aligned} &D_s \neq 0 \\ &\cot\theta_1 = \tan\theta_2 = 0 \end{aligned} \tag{5.14}$$

With (5.12) and (5.14), we can obtain the design equations for the matched series-type uniplanar magic-T as below.

$$\begin{aligned} &Z_2^2 \neq Z_H(Z_0 - Z_E) \\ &Z_1 = \sqrt{Z_E Z_0} \\ &Z_0 = Z_H \\ &\theta_1 = \frac{\pi}{2} + n\pi \quad \Rightarrow \frac{\lambda_g}{4} + n\cdot\frac{\lambda_g}{2} \\ &\theta_2 = n\pi \quad \Rightarrow n\cdot\frac{\lambda_g}{2} \end{aligned} \tag{5.15}$$

In which λ_g is a guided wavelength and $n = 0,1,2,\ldots$.

(5.15) shows that the transmission line section with respect to θ_1 and Z_1 functions as a quarter-wavelength impedance transformer which is in line with the lumped circuit model of magic-T discussed before. Since the length of transmission line section with respect to

θ_2 is related to a half of wavelength, there is no impedance transforming and the characteristic impedance of port H can not be arbitrarily chosen. The minimum electrical length of $\theta_1 + \theta_2$ is equal to $\frac{\pi}{2}$ (or $\frac{\lambda_g}{4}$). In the previous chapters, it is found that for the broadband design of ring coupler with a phase inverter the electrical length for the all transmission line sections on the ring is equal to a quarter wavelength. Clearly, this property does not hold for the design of series-type uniplanar magic-T.

Case 2: *Nontrivial solution for* $\cot\theta_1$ *and* $\tan\theta_2$

For the nontrivial solution, we have

$$D_s = 0 \tag{5.16}$$

With a straightforward mathematical manipulation, we can derive the other set of design equations for the matched series-type uniplanar magic-T as below.

$$\begin{aligned} Z_2^2 &= Z_H(Z_0 - Z_E) \\ Z_1^2 &= Z_0 Z_E + (Z_0 - Z_E)(Z_H - Z_0) \\ \tan^2\theta_1 &= \frac{Z_0}{Z_H - Z_0} + \frac{Z_0 - Z_E}{Z_E} \\ \tan^2\theta_2 &= \frac{(Z_H - Z_0)(Z_0 - Z_E)}{Z_H Z_E} \end{aligned} \tag{5.17}$$

From (5.17), it is seen that the following conditions for the port characteristic impedance must hold.

$$Z_E \le Z_0 \le Z_H \tag{5.18}$$

In a typical application, we choose the characteristic impedance of all input ports to be the same as Z_0, that is,

$$\begin{aligned} Z_E &= Z_0/2 \\ Z_H &= 2Z_0 \end{aligned} \tag{5.19}$$

With (5.17) and (5.19), The design equations for the series-type uniplanar magic-T with the same characteristic impedance at all ports can be rewritten as

$$\begin{aligned} Z_1 &= Z_0 \\ Z_2 &= Z_0 \\ \tan\theta_1 &= \sqrt{2} \\ \tan\theta_2 &= \frac{1}{\sqrt{2}} \end{aligned} \tag{5.20}$$

Obviously, the characteristic impedance for all transmission line sections in the series-type uniplanar magic-T is the same, which makes the design be much simple. Again the minimum electrical length of $\theta_1 + \theta_2$ is equal to $\frac{\pi}{2}$ (or $\frac{\lambda_g}{4}$).

5.3.2 Parallel-type uniplanar magic-T

Figure 5.4(b) shows the parallel-type uniplanar magic-T. The circuit parameters are also described in the figure. The Y_{EE} and Y_{HH} denote the characteristic admittance for ports E and H, respectively. The symbol Y_0 stands for the characteristic admittance of ports 1 and 2. The electrical length and characteristic admittance for transmission lines connected to the E-junction are described by θ_1 and Y_1, respectively. The θ_2 and Y_2 stands for the electrical length and characteristic admittance of the transmission lines connected to H-junction. Since there is no coupling between ports E and H, the uniplanar magic-T can be

decomposed to a simple one-port network under E- and H-port excitation as shown in Figure 5.7. Again with the excitation at H-port the series-junction connecting to port E is equivalent to open-circuit while with the excitation at E-port the parallel-junction connecting to port H is equivalent to short-circuit.

Similarly, the input reflection coefficients S_{EE} and S_{HH} in Figure 5.7 can be written as

$$S_{EE} = \frac{Y_{EE} - Y_{inE}}{Y_{EE} + Y_{inE}}$$
$$S_{HH} = \frac{Y_{HH} - Y_{inH}}{Y_{HH} + Y_{inH}} \tag{5.21}$$

Where Y_{inE} and Y_{inH} are the input admittance with the excitation at ports E and H, respectively. Using a straightforward circuit analysis, we can express S_{EE} and S_{HH} in terms of the circuit parameters as below.

$$S_{EE} = \frac{Y_1(Y_E - Y_0) + Y_E Y_2 \tan\theta_1 \cot\theta_2 + j\left[(Y_E Y_0 - Y_1^2)\tan\theta_1 + Y_1 Y_2 \cot\theta_2\right]}{Y_1(Y_E + Y_0) + Y_E Y_2 \tan\theta_1 \cot\theta_2 + j\left[(Y_E Y_0 + Y_1^2)\tan\theta_1 - Y_1 Y_2 \cot\theta_2\right]}$$
$$S_{HH} = \frac{Y_2(Y_H - Y_0) - Y_H Y_1 \tan\theta_1 \tan\theta_2 - j\left[Y_2 Y_1 \tan\theta_1 + (Y_2^2 - Y_H Y_0)\tan\theta_2\right]}{Y_2(Y_H + Y_0) - Y_H Y_1 \tan\theta_1 \tan\theta_2 + j\left[Y_2 Y_1 \tan\theta_1 + (Y_2^2 + Y_H Y_0)\tan\theta_2\right]} \tag{5.22}$$

Where $Y_E = 2Y_{EE}$ and $Y_H = Y_{HH}/2$

The condition for a matched uniplanar magic-T can be written as

$$S_{EE} = 0$$
$$S_{HH} = 0 \tag{5.23}$$

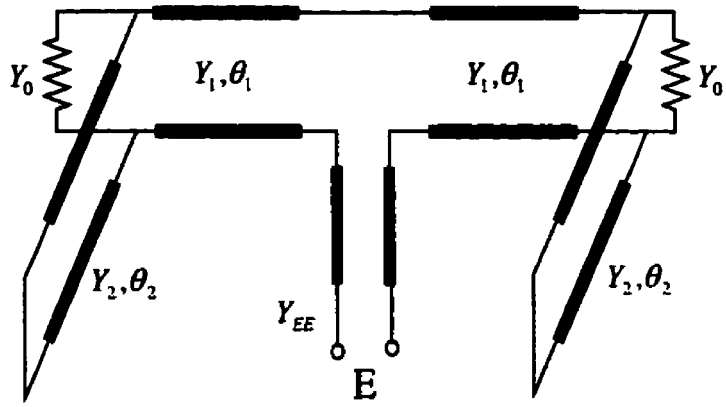

(a)

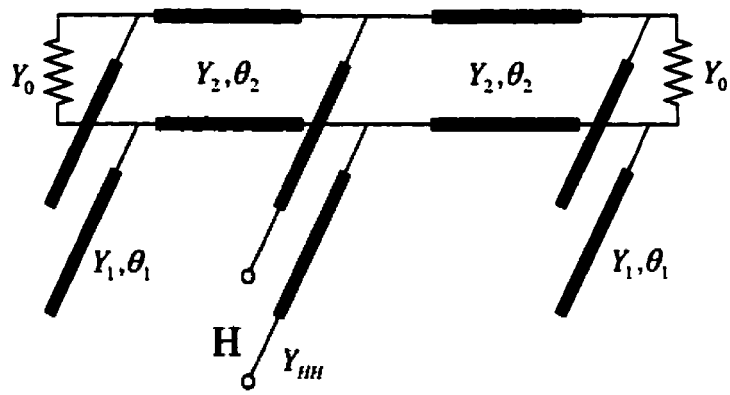

(b)

Figure 5.7 Equivalent circuits of parallel-type uniplanar magic-T with the excitation (a) at port E and (b) at port H.

Substituting (5.22) into (5.23), the following relationship can be derived.

$$\begin{aligned}
&(Y_E Y_0 - Y_1^2)\tan\theta_1 + Y_1 Y_2 \cot\theta_2 = 0 \\
&Y_H Y_1 \tan\theta_1 - Y_2(Y_H - Y_0)\cot\theta_2 = 0 \\
&Y_1(Y_E - Y_0) + Y_E Y_2 \tan\theta_1 \cot\theta_2 = 0 \\
&(Y_2^2 - Y_H Y_0) + Y_1 Y_2 \tan\theta_1 \cot\theta_2 = 0
\end{aligned} \tag{5.24}$$

Again the first two equations in (5.24) are a set of linear homogeneous algebraic equations with respect to $\tan\theta_1$ and $\cot\theta_2$. Its solutions can be divided into two cases: trivial and nontrivial ones. In the following, we discuss the solutions of (5.24) for the two cases, respectively.

Case 1: *Trivial solution for* $\tan\theta_1$ *and* $\cot\theta_2$

The determinant of the coefficients for the first two equations in (5.24) can be written as

$$D_p = \begin{vmatrix} (Y_E Y_0 - Y_1^2) & Y_1 Y_2 \\ Y_H Y_1 & -Y_2(Y_H - Y_0) \end{vmatrix} \tag{5.25}$$

For the trivial solution, we have

$$\begin{aligned}
&D_p \neq 0 \\
&\tan\theta_1 = \cot\theta_2 = 0
\end{aligned} \tag{5.26}$$

In terms of (5.24) and (5.26), we can obtain the design equations for the matched parallel-type uniplanar magic-T as below.

$$
\begin{aligned}
&Y_1^2 \neq Y_E(Y_0 - Y_H) \\
&Y_2 = \sqrt{Y_H Y_0} \\
&Y_E = Y_0 \\
&\theta_1 = n\pi \qquad\qquad \Rightarrow n \cdot \frac{\lambda_g}{2} \\
&\theta_2 = \frac{\pi}{2} + n\pi \qquad \Rightarrow \frac{\lambda_g}{4} + n \cdot \frac{\lambda_g}{2}
\end{aligned}
\tag{5.27}
$$

From (5.27), it is seen that the transmission line section with respect to θ_2 and Z_2 functions as a quarter-wavelength impedance transformer which is again in line with the lumped circuit model of magic-T discussed before. Since the length of transmission line section with respect to θ_1 is equal to multiple half of wavelength, there is no impedance transforming and the characteristic admittance of port E can not be arbitrarily chosen. The minimum electrical length of $\theta_1 + \theta_2$ is equal to $\frac{\pi}{2}$ (or $\frac{\lambda_g}{4}$).

Case 2: *Nontrivial solution for* $\tan\theta_1$ *and* $\cot\theta_2$

For the nontrivial solution, we have

$$D_p = 0 \tag{5.28}$$

In terms of (5.24) and (5.28), we can obtain the other set of design equations for the matched parallel-type uniplanar magic-T as below.

$$
\begin{aligned}
&Y_1^2 = Y_E(Y_0 - Y_H) \\
&Y_2^2 = Y_0 Y_H + (Y_0 - Y_H)(Y_E - Y_0) \\
&\tan^2\theta_1 = \frac{(Y_0 - Y_H)(Y_E - Y_0)}{Y_H Y_E} \\
&\tan^2\theta_2 = \frac{Y_0 - Y_H}{Y_H} + \frac{Y_0}{Y_E - Y_0}
\end{aligned}
\tag{5.29}
$$

From (5.29), it is seen that the conditions of (5.18) also hold for the parallel-type uniplanar magic-T.

In a typical application, we choose the characteristic admittance of all input ports to be the same as Y_0, that is,

$$\begin{aligned} Y_E &= 2Y_0 \\ Y_H &= Y_0/2 \end{aligned} \tag{5.30}$$

With (5.29) and (5.30), The design equations for the parallel-type uniplanar magic-T with the same characteristic admittance at all input ports can be simplified as

$$\begin{aligned} Y_1 &= Y_0 \\ Y_2 &= Y_0 \\ \tan\theta_1 &= \frac{1}{\sqrt{2}} \\ \tan\theta_2 &= \sqrt{2} \end{aligned} \tag{5.31}$$

It is obvious that the minimum electrical length of $\theta_1 + \theta_2$ is equal to $\frac{\pi}{2}$ (or $\frac{\lambda_g}{4}$).

It should be noted that the uniplanar magic-T circuits are similar to the ring couplers with a phase inverter, which are discussed in the previous chapters. The reversal phase in the magic-T circuit is provided by E-junctions. Since the magic-T circuits are symmetrical with the plane P-P, it can be expected that the magic-T's have better performance in terms of amplitude imbalance. From the above analysis, it is obvious that the magic-T design equations are different from ones of the ring couplers with a phase inverter. In the following section, we will present the numerical and experimental results for a compact uniplanar magic-T circuit in order to verify the design procedure developed here.

5.4 Numerical and experimental results for a compact uniplanar magic-T

In the previous section, the analysis and design criteria for the uniplanar magic-T's have been developed. To validate the proposed design theory, this section presents numerical and experimental results for a compact uniplanar magic-T. In the following, we first give a brief description of the compact uniplanar magic-T circuit. Then the numerical results for the magic-T are calculated using the full-wave analysis based on finite element technique. The experimental results are also presented and discussed in detail.

5.4.1 Description of a compact uniplanar magic-T circuit

Figure 5.8 shows the physical configuration of a compact uniplanar magic-T. The port E of the magic-T is fed through a CPW connected to the CPW-slotline transition. The ports H, 1 and 2 are all fed by CPW lines. Ports 1 and 2 are symmetrical with respect to the slotline and CPW double-T junctions. The four short dark lines across CPW represent airbridge, which is used to suppress the slotline mode in the CPW feed lines. Since ports 1 and 2 are fed by CPW lines, the magic-T can be classified as parallel-type. From (5.27), it is seen that for a parallel-type uniplanar magic-T, the minimum of θ_1 and θ_2 can be written as

$$\begin{aligned} \theta_1 &= 0 \\ \theta_2 &= \pi/2 \end{aligned} \tag{5.32}$$

For the characteristic admittance of feed lines, the following condition must hold

$$\begin{aligned} Y_2 &= \sqrt{Y_H Y_0} \\ Y_E &= Y_0 \end{aligned} \tag{5.33}$$

It is noted that in Figure 5.7 the two impedance transforming sections connected to port H have been combined to form a compact circuit. The uniplanar magic-T was built on a

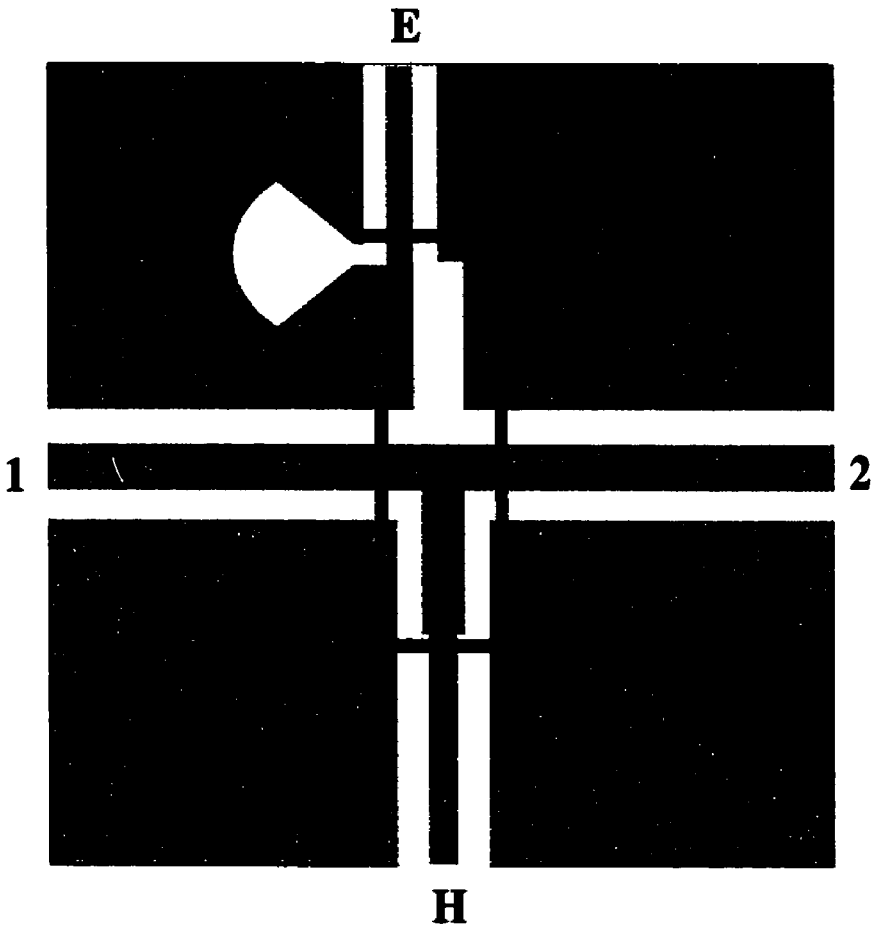

Figure 5.8 Physical configuration of a compact uniplanar magic-T

RT/Duriod 6010 ($\varepsilon_r = 10.2$) substrate with the thickness $h = 1.27$ mm. The characteristic impedance for CPW feed lines was chosen as 70.7 Ω with the dimensions: the center conductor width $W = 0.30$ mm and the gap size between the ground and center conductor $S = 0.41$ mm. Using (5.32) and (5.33), we can obtain the characteristic impedance for the quarter-wavelength slotline and CPW impedance transformers as 100 Ω and 50 Ω, respectively. The circuit was designed with the center frequency $f = 3.5$ GHz. The dimensions for the slotline impedance transformer are the slot width $S = 0.82$ mm and the quarter-wavelength $\lambda_g/4 = 12$ mm. The dimensions for the CPW-line impedance transformer are the center conductor width $W = 0.60$ mm, the gap size $S = 0.26$ mm and the quarter-wavelength $\lambda_g/4 = 9.2$ mm. In the CPW to slotline transition, a wideband slotline radial stub was used. The dimensions for the radial stub are the radius $r = 8$ mm and angle $\alpha = 60°$.

5.4.2 Numerical results

The performance of the magic-T described above was calculated using the commercial software HFSS that was developed and marketed by Ansoft. HFSS is a 3D full-wave simulator, which uses finite element technique to solve Maxwell equations. The circuit parameters are extracted based on the field solutions. The geometry of the magic-T used in the performance calculation is shown in Fig. 5.9. A virtual box was introduced to define the filed solution area. Radiation boundaries were assigned to the surfaces of the virtual box in analysis in order to consider the effect of unshielding of the circuit. To conserve computing resources, the virtual box was chosen to have the dimensions: $30\times30\times30$ mm^3. The dimensions for all of feeding ports are 7.5×7.5 mm^2. In the analysis model, four air brides with a square cross-section (0.2×0.2 mm^2) are also included. The calculated frequency responses for return loss, coupling, isolation and phase difference are shown in Figure 5.10.

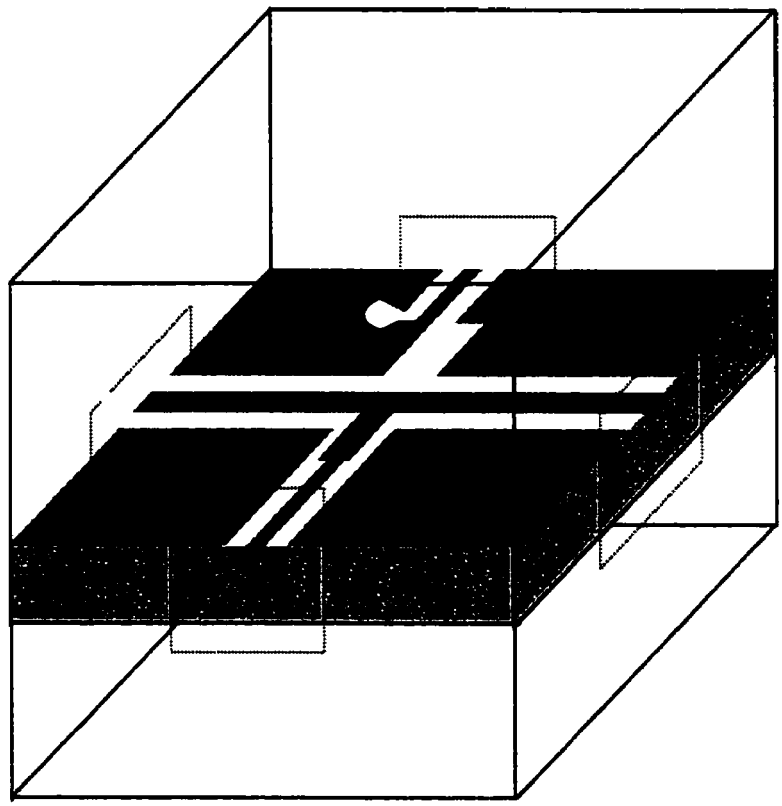

Figure 5.9 Geometry of the uniplanar magic-T for finite element analysis

In Figure 5.10(a), it is seen that the return loss of the magic-T is better than -17 dB at the center frequency $f = 3.5$ GHz. The minimum return loss of port H is –24 dB at around 3.0 GHz. The center frequency shift of return loss at port H is due to the double-T junction effects, which was not included in the circuit design. Similarly, the center frequency of return loss for ports 1 and 2 are slightly shifted to higher frequency due to the same cause. It is obvious that the inequality (5.6) hold for the magic-T except for the small error at around 3.3 GHz. Figure 5.10(b) shows the frequency response of power dividing for the ports E and H. Clearly, the two outputs at ports 1 and 2 have very good behavior for the amplitude balance. The extra insertion loss of port E is larger than that of the port H, which may be caused by the radiation loss of the slotline transformer and slotline radial stub. The mutual isolation for ports E(1) and H(2) is shown in Figure 5.10(c). As expected, there is a very good isolation (better than 40 dB) between ports E and H. Figure 5.10(d) shows the phase difference for the in-phase and 180° out of phase mode coupling. The phase error is less than 1° in the frequency range of 2 - 4.5 GHz. In a summary, the calculated results show that the proposed magic-T has a fairly good performance. To some extent, it validates the design theory, which was developed in the previous section.

5.4.3 Experimental results

The measured performance of the proposed magic-T is shown in Figure 5.11. The measurement was made using GGB probes (40A-GSG-1250) and a vector network analyzer (HP 8720ES). TRL calibration was employed to remove the systematic errors of the test station. In the each measurement, a two-port S-parameter was obtained under the condition of terminating the other two ports of the magic-T. The termination for each port was implemented by soldering two chip resistors in parallel to CPW-line. It is noted that the chip resistors should be symmetrically placed on the CPW line to eliminate slotline-mode excitation. Figure 5.11(a) shows the measured frequency response of return loss for the four input ports of the proposed magic-T. It is seen that the return loss is better than

-18 dB in the frequency range of 3 - 3.5 GHz, which agrees with the calculated results. The measured frequency response of power dividing for ports E and H is shown in Figure 11(b). It is obvious that the extra insertion of port H is less than that of port E which agrees with the prediction in the field analysis. The maximum amplitude imbalance for the port H is less than 0.2 dB in the frequency range of 2 - 4.5 GHz. Figure 11(c) shows the measured mutual isolation between the ports E (1) and H (2). It is seen that the mutual isolation at $f = 3.5$ GHz is better than -20 dB. The isolation between ports E and H is better than -40 dB in the frequency range of 2 - 4.5 GHz, which agrees very well with the calculated one shown in Figure 10(c). The measured phase difference for the in-phase and 180° out of phase mode coupling is shown in Figure 11(d). The phase error may be caused by the uncertainty of the probe landing location in different measurement. It should be noted that the resistor termination and its location placed on the CPW lines also contribute some test error.

5.5 Conclusion

In this chapter, the analysis of uniplanar magic-T has been described in detail. General speaking, the uniplanar magic-T can be classified as two types. The design equations for each type were derived. The properties of uniplanar magic-T were summarized and discussed. A compact uniplanar magic-T was designed to validate the developed design theory. The numerical and experimental results were presented. It is seen that the uniplanar magic-T has fairly good performance in terms of amplitude imbalance between two output ports.

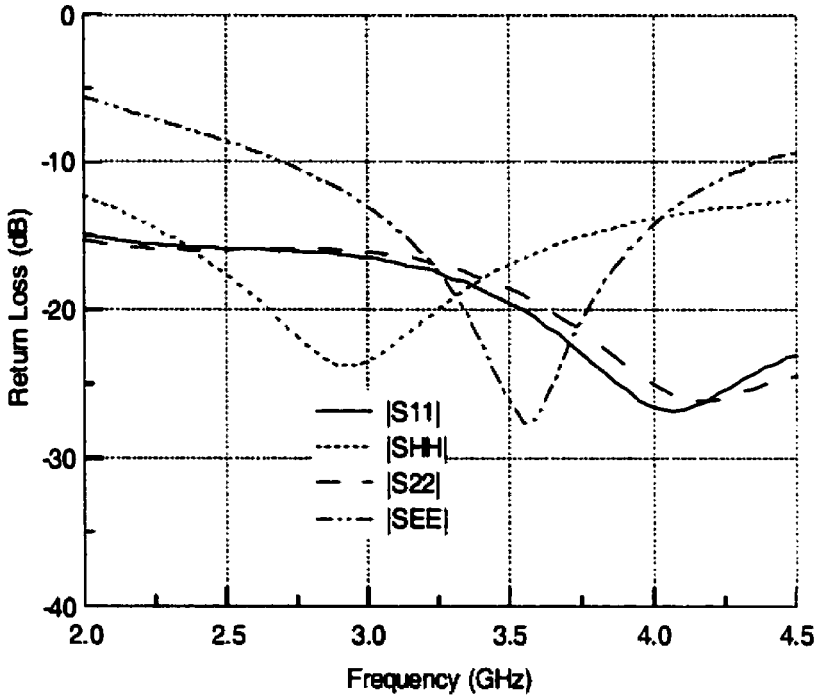

Figure 5.10(a) Calculated frequency responses of return loss for the four input ports of the magic-T shown in Figure 5.9

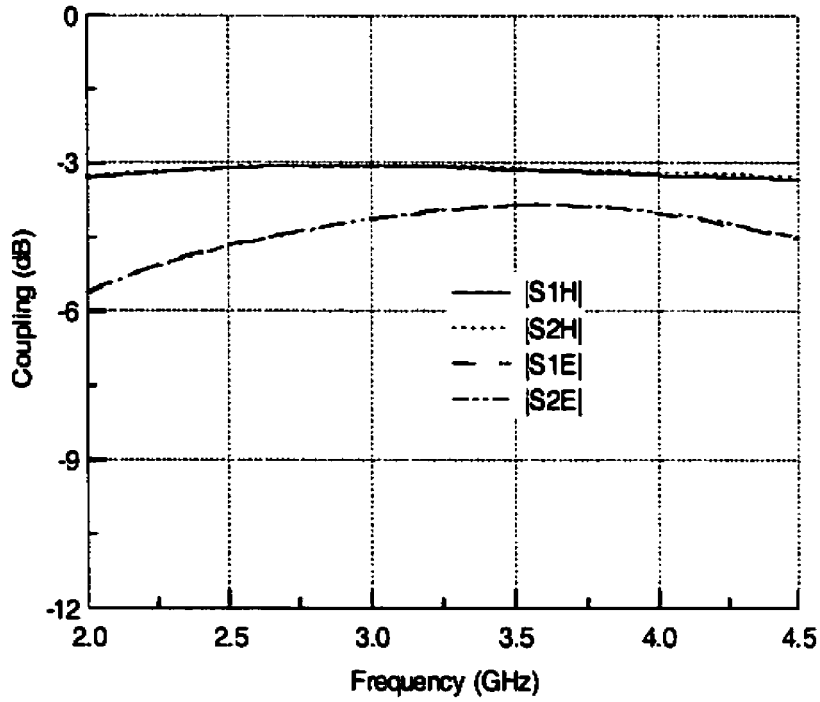

Figure 5.10(b) Calculated frequency responses of the power dividing of ports E and H for the magic-T shown in Figure 5.9

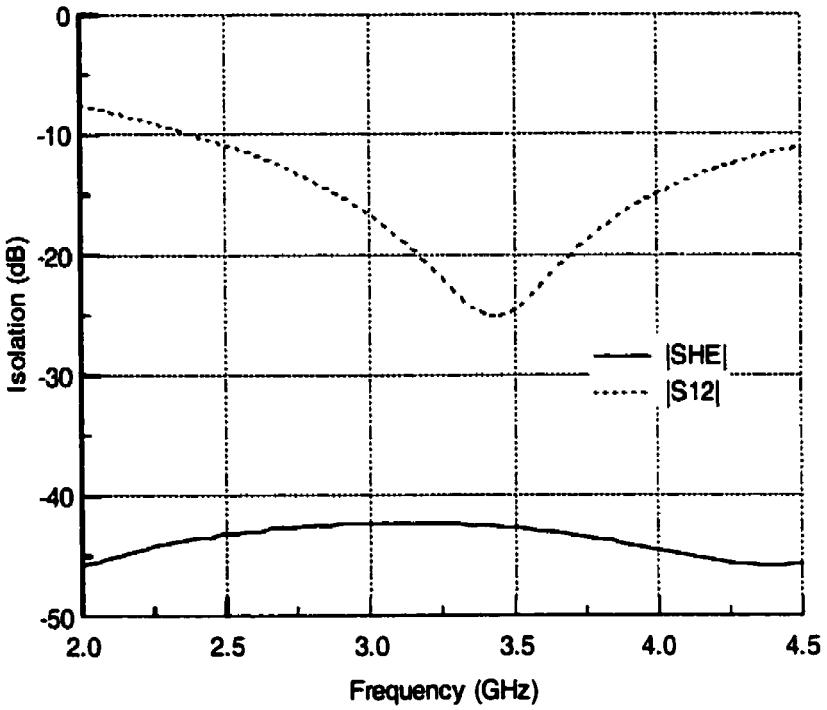

Figure 5.10(c) Calculated frequency responses of the mutual isolation for the magic-T shown in Figure 5.9

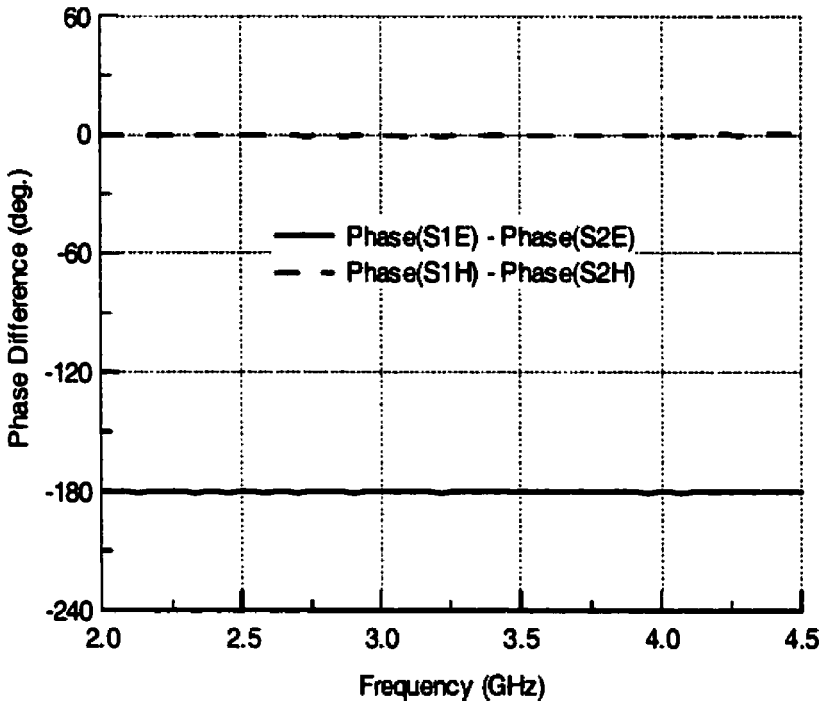

Figure 5.10(d) Calculated phase difference between output ports 1 and 2 for the magic-T shown in Figure 5.9

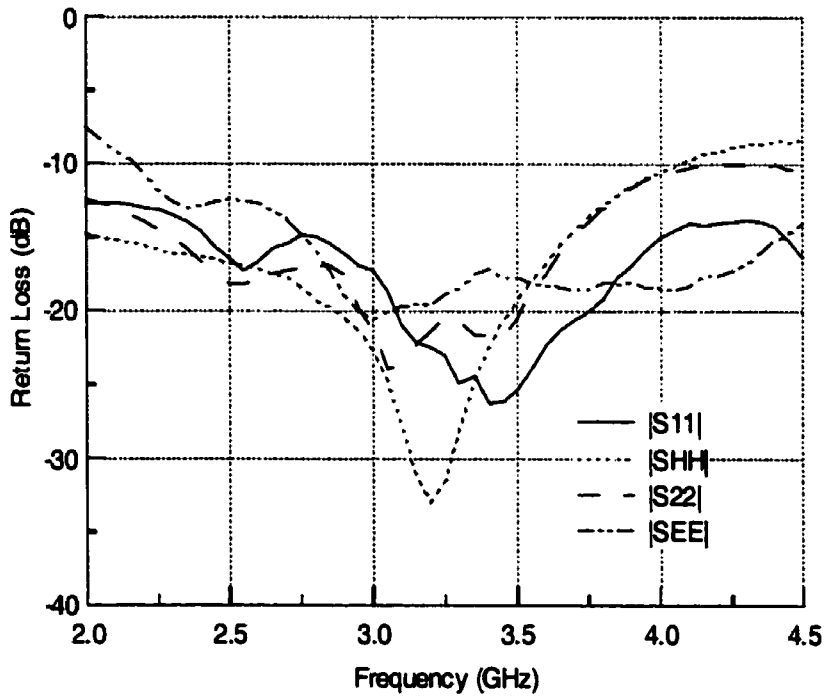

Figure 5.11(a) Measured frequency responses of return loss for the four input ports of the magic-T shown in Figure 5.8

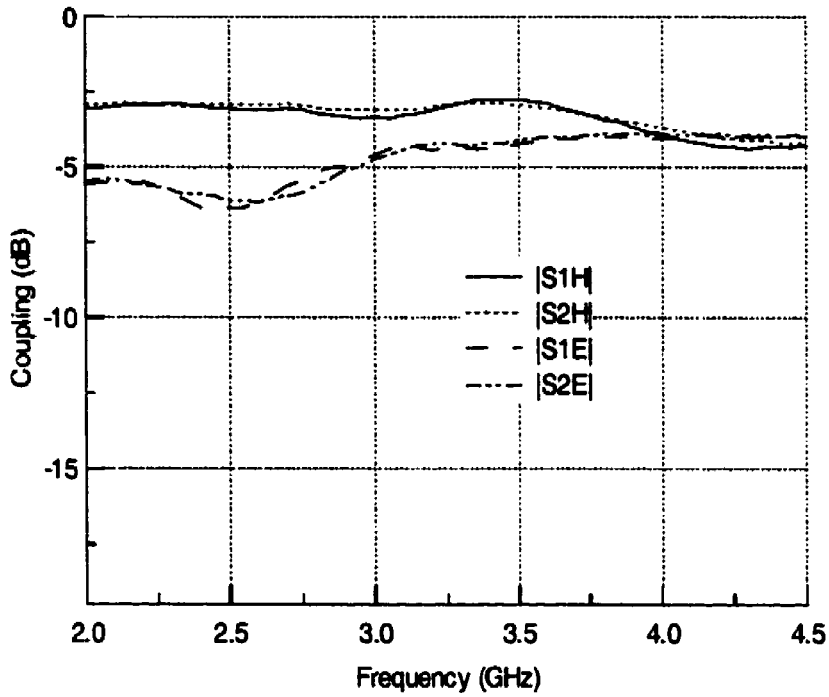

Figure 5.11(b) Measured frequency responses of the power dividing of ports E and H for the magic-T shown in Figure 5.8

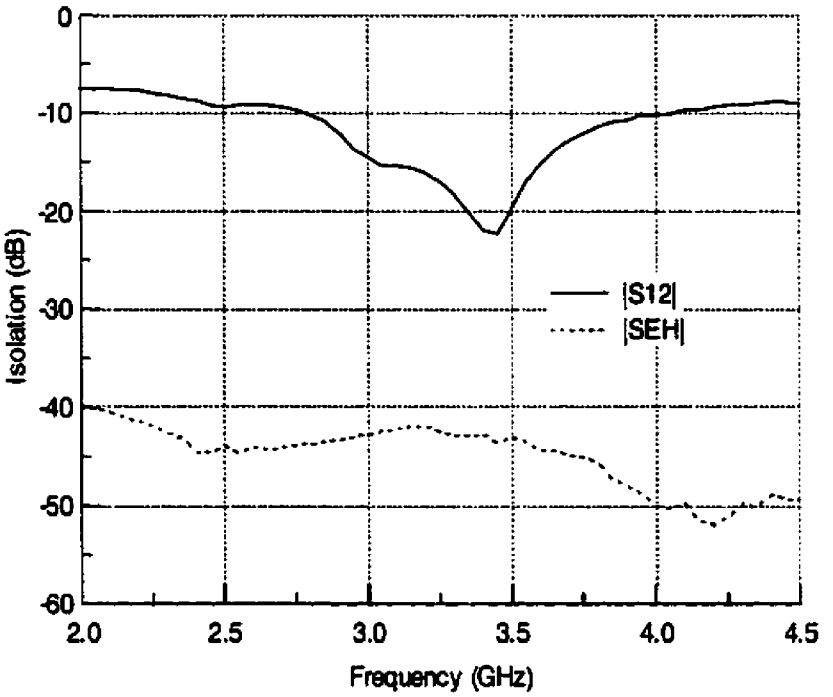

Figure 5.11(c) Measured frequency responses of the mutual isolation for the magic-T shown in Figure 5.8

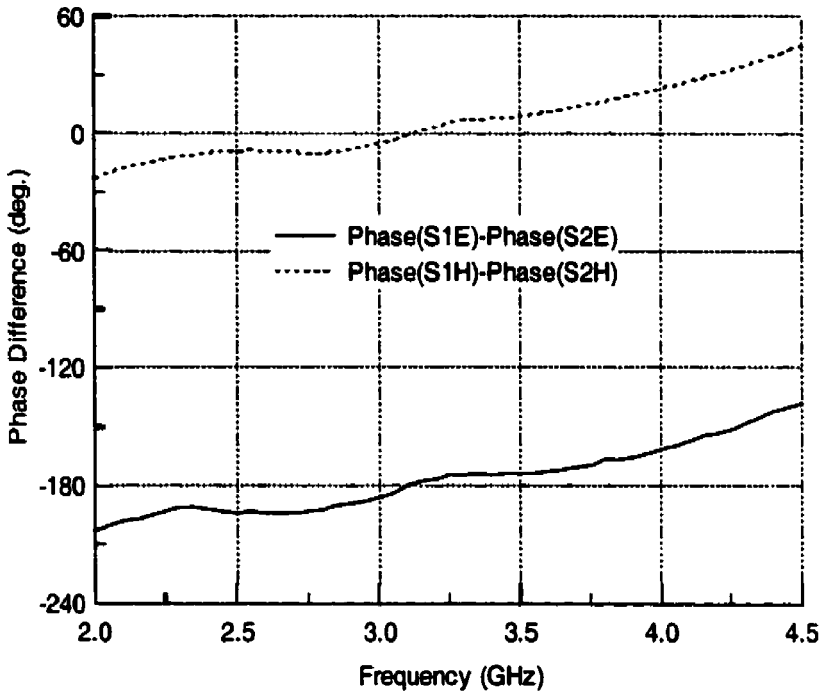

Figure 5.11(d) Measured phase difference between output ports 1 and 2 for the magic-T shown in Figure 5.8

Chapter VI

Conclusions And Recommendations For Future Work

6.1 Conclusions

To conclude, this thesis has presented the study of uniplanar phase inverters, ring couplers and Magic-T's. Several novel uniplanar circuits have been developed. The circuits can be used as fundamental building blocks in many microwave and millimeter-wave integrated circuit applications. Following is a summary of work described in this thesis.

Coplanar stripline and micro-coplanar stripline phase inverter circuits have been developed. The electrical performance for the phase inverters were calculated using the full-wave analysis based on finite element method. The calculated and experimental results show that both phase inverter circuits are suited for broadband application. For the coplanar phase inverter, the insertion loss within -0.4 dB has been achieved up to 10.0 GHz while the phase shift within $-182° \pm 3°$ has been obtained up to 8.8 GHz. As expected, the usable bandwidth of micro-coplanar stripline phase inverter is smaller than the counterpart of coplanar stripline due to the effect of slotline radial stub. The measured results show that the insertion loss of micro-coplanar stripline phase inverter is within -1.0 dB in the frequency range of 1.9 - 4.7 GHz, which corresponds to more than one octave bandwidth.

Hybrid ring coupler is one of fundamental components in microwave and millimeter-wave integrated circuits. In general, ring couplers are divided into two categories: series-

type and parallel-type. A comprehensive study for both types of uniplanar ring couplers with phase inverter has been achieved. A set of design equations were derived. Principle features and design consideration for the ring coupler are summarized. The design criteria for broadband and narrow-band applications are discussed. Two ring coupler circuits have been developed. The electrical performance was obtained using a finite element analysis. Numerical and experimental results are presented to verify the proposed design concept. The measurements show that both ring couplers have a fairly good electrical performance. Their mutual isolation is better than $-20.0\,\text{dB}$ over a bandwidth of more than one octave. For the series-type coplanar stripline ring coupler, the phase error of less than $\pm 4°$ has been demonstrated in the frequency range of $1.0 - 2.3\,\text{GHz}$.

Magic-T circuit is widely used in microwave and millimeter-wave system. The analysis and design of novel uniplanar magic-T circuits have been presented. Two basic configurations of uniplanar magic-T circuits were described. The electrical performance of uniplanar magic-T circuits was discussed. The matching condition of uniplanar magic-T circuits has been obtained from a simple circuit analysis. A general design formulation was derived. A compact uniplanar magic-T circuit has been developed. The magic-T consists of slotline and coplanar waveguide double-T junctions. The electrical characteristics is calculated using finite element analysis. The circuit has fairly good amplitude balance and mutual isolation. The measured results showed that the maximum amplitude imbalance for the port H is less than $0.2\,\text{dB}$ in the frequency rang of $2 - 4.5\,\text{GHz}$. Over the same frequency range, the isolation between ports E and H is better than $-40\ \text{dB}$.

6.2 Recommendations

This thesis presented the framework of the uniplanar phase inverter, ring coupler and magic-T circuit analysis and design. The future work associated with this thesis should include the following aspects.

One subject which deserves more consideration is to develop wideband phase inverters using various uniplanar guided-wave structures. Generally, uniplanar guided-wave structures consist of coplanar waveguide, coplanar stripline, micro-coplanar stripline and slotline. More complicated phase inverter circuits can be designed using the combination of different type of transmission lines.

The design of 3-dB ring coupler with phase inverter has been discussed in this thesis. As extension to this work, the further study should be concentrated on improving circuit performance and developing new circuit configurations. The design theory developed here is general and can be extended to the design of arbitrary power-dividing ratio ring coupler.

In the magic-T design, one work which remains to be done is to develop a design procedure in terms of bandwidth requirement. Uniplanar magic-T is divided into two basic types. For each type, there are two solutions. For practical applications, it is necessary to determine the effective bandwidth for each solution. The further work should also include new circuit development.

This thesis presented several basic uniplanar circuits (phase inverter, ring coupler and magic-T). One obvious extension is to use these basic configurations to develop more complicated circuit function blocks such as balanced amplifier, balanced mixer, and uniplanar microwave and millimeter-wave transceiver for radar and communication systems. Another important work required to be addressed is how to package uniplanar circuits for commercial applications.

References

[1] MURAGUCHI, M., et al. (1988). Uniplanar MMIC's and their applications. IEEE Trans. Microwave Theory Tech., 36, 1896-1901.

[2] HIROTA, T., et al. (1987). Uniplanar MMIC hybrids -- a proposed new MMIC structure. IEEE Trans. Microwave Theory Tech., 35, 576-581.

[3] CHANG, K. (1996). Microwave Ring Circuits and Antennas. John Wiley & Sons, New York.

[4] FAN, L., et al. (1996). Uniplanar power dividers using coupled CPW and asymmetrical CPS for MIC's and MMIC's. IEEE Trans. Microwave Theory Tech., 44, 2411-2420.

[5] LANGE, J. (1969). Interdigitated strip-line quadrature hybrid. 1969 G-MTT Int. Microwave Symp. Dig., 10-13.

[6] SCHIEK, B. (1974). Hybrid branchline coupler -- a useful new class of directional couplers. IEEE Trans. Microwave Theory Tech., 22, 864-869.

[7] HOFFMAN, R. K. and SIEGL, J. (1982). Microstrip-slot coupler design, Part I and II. IEEE Trans. Microwave Theory Tech., 30, 1205-1216.

[8] PON, C. P. (1961). Hybrid-ring directional coupler for arbitrary power division. IRE Trans. Microwave Theory Tech., 9, 529-535.

[9] MARCH, S. (1968). A wide band stripline hybrid ring. IEEE Trans. Microwave Theory Tech., 16, 361.

[10] KIM, D. I. and NAITO, Y. (1982). Broad-band design of improved hybrid-ring 3-dB directional couplers. IEEE Trans. Microwave Theory Tech., 30, 2040-2046.

[11] KIM, D. I. and G. S YANG, G. S. (1991). Design of new hybrid-ring directional coupler using $\lambda/8$ or $\lambda/6$ sections. IEEE Trans. Microwave Theory Tech., 39, 1779-1783.

[12] HO, C. H., FAN, L. and CHANG, K. (1994). New uniplanar coplanar waveguide hybrid-ring couplers and Magic-T's. IEEE Trans. Microwave Theory Tech., 42, 2240-2248.

[13] MURGULESCU, M. H., et al., (1994). New wideband, $0.67\lambda_g$ circumference 180^0 hybrid ring coupler. Elect. Lett., 30, 299-300.

[14] WANG, T. and WU, K., (1999). Size-reduction and band-broadening design technique of uniplanar hybrid ring coupler using phase inverter for M(H)MIC's. IEEE Trans. Microwave Theory Tech., 47, 198-206.

[15] WANG, T., OU, Z. and WU, K., (1997). Experimental study of wideband uniplanar phase inverters for MIC's. IEEE MTT-s Int. Microwave Symp. Dig., 777-780.